Thermal Model of Microrobot

Yu-Ming Chen

A thesis submitted in partial fulfillment
of the requirements for the degree of

Master of Science in Electrical Engineering

University of Washington

2005

Program Authorized to Offer Degree: Electrical Engineering

University of Washington
Graduate School

This is to certify that I have examined this copy of a master' s thesis by

Yu-Ming Chen

and have found that it is complete and satisfactory in all respects, and that any and all revisions required by the final examining committee have been made.

Committee Members:

_____
Karl F. Böhringer

_____
Lih Y. Lin

_____
Babak Amir Parviz

Date _____

In presenting this thesis in partial fulfillment of the requirements for a master' s degree at the University of Washington, I agree that the Library shall make its copies freely available for inspection. I further agree that extensive copying of this thesis is allowable only for scholarly purposes, consistent with " fair use" as prescribed in the U.S. Copyright Law. Any other reproduction for any purpose or by any means shall not be allowed without my written permission.

Signature_____

Date_____

TABLE OF CONTENTS

List of Figures **iii**

Glossary **xi**

Chapter 1: Introduction **1**

1.1 Related Work.....1

1.2 Previous Research of The Micro Cilia Array Chip 7

1.3 Overview of Thesis.....10

Chapter 2: Microrobot Overview **11**

2.1 Microrobot Size……11

2.2 Micro Cilia Array Chip…… 14

2.3 Micro Cilium Actuator ……17

Chapter 3: Experiments and Methods **20**

3.1 Four-Phase Motion.....20

3.2 Motion Tracking Software 23

3.3 Controller Board.....28

3.4 Temperature Measurement 30

Chapter 4: Results and Discussion **33**

4.1 The Microrobot Speed 33

4.2 The Heat Dissipation of Different Step Frequencies.....44

4.3 The Correlation Between Temperature and Speed.....49

4.4 The Influence of Surface Roughness....51
4.5 Simulations....57
4.5.1 Simulation Considerations....57
4.5.2 Macroscopic Simulation....59
4.5.3 Micro Cilium Simulation....68
4.5.4 Lifting Capacity....73
4.5.5 FSI Simulation....77
Chapter 5: Conclusion and Future Works 84
5.1 Conclusion....84
5.2 Future Works....85
List of References 87
Appendix A: Macroscopic Simulation 89
A.1 Dimension and Material Properties....89
A.2 Heat Generation....92
A.3 Boundary Conditions....93
A.3.1 Hot Flat Plate Facing Up....94
A.3.2 Vertical Flat Plate....98
Appendix B: Micro Cilium Simulation 100

LIST OF FIGURES

1.1 Solar powered 10mg silicon robot [8]. (a) electrostatic inchworm motors and two legs (b) solar cells (c) CMOS digital sequencer……2

1.2 Untethered micro actuators for autonomous micro-robot locomotion [9]. Its dimension is usually 100μm×80μm×(1~2μm) (a) a schematic shows how the robot moves. (b) the V_1 and V_2 electrodes build a voltage potential, V_{plate}. on the robot (c) An optical micrograph of the untethered robot. ……3

1.3 Prototype microrobots for micro positioning in a manufacturing process and micro unmanned vehicles [7]. (a) a SEM picture indicates the structure of the two degrees of freedom leg. (b) dimension of the leg (c) demonstration of bearing an insect (d) a simplified wiring diagram…….4

1.4 A walking silicon microrobot [10]. (a) the design of one leg (b) the operation principle for driving the microrobot (c) the load test of its maximum 2500mg load capacity……6

1.5 A schematic shows the idea of the docking system [2]……7

1.6 The experimental setup of the docking system [2]. The air table lift up the puck using air force and the slope adjust knob changes the normal force on the micro cilia array chips. ……..8

1.7 The experimental setup pictures of the docking system related to Figure 1.6 [2]. ……9

2.1 The soldering equipment for bonding the control wires on top of the PCB. ……12

2.2 Top view of the microrobot. The printed circuit board (PCB) bonds two micro cilia array chips, thus forming the backbone of the microrobot. The contacts on the PCB electrically connect to control wires. …….12

2.3 Bottom view of the microrobot. The printed circuit board (PCB) bonds two micro cilia array chips. The contacts on the PCB electrically connect to two chips via gold wires. ……..13

2.4 The schematic of the microrobot. The microrobot's size is about 30mm×10mm×1mm. ……14

2.5 Schematic of micro cilia array chip and one motion cell. This figure is scanned from John Suh's dissertation [1]. The T1 through T4 labels mark the thermal control wires and the E1 through E4 labels mark the electrostatic control wires. ……..16

2.6 SEM picture of the motion cells in the unheated state taken by Xiaorong Xiong at Washington Technology Center. ……16

2.7 The resistance of thermal control wires and the corresponding contacts on top of PCB. N1~W1 is for chip 1 and N2~W2 is for chip 2. ……..17

2.8 The illustration of the micro cilium and the detailed layout of its structure. The thickness of each layer is shown in the parenthesis. This plot is scanned from John Suh's dissertation [1]. ……18

2.9 A SEM picture scanned from John Suh's dissertation [1] shows the lift-up height of the micro cilium in the unheated state. The heights at position A and B are about 91μm and 117μm respectively. ……...19

3.1 A schematic of the four-phase motion. (a) A schematic of one motion pixel. The red color means the leg lifts up. (b) A side view of the four-phase motion corresponding to part (a). ……21

3.2 LabVIEW interface for microrobot control. It allows an operator to control the motion of the two micro cilia array chips separately. ……..22

3.3 Eight tracking markers. ARToolKit can recognize these markers and record their positions and rotational angle. ……..24

3.4 The dimension of the tracking markers. ……24

3.5 The eight tracking markers are printed on a strip of paper and put on the microrobot. ……24

3.6 ARToolKit interface. The upper part is the output screen of ARToolKit. ARToolKit puts a virtual 3D shape on the recognized tracking marker. The bottom window shows the position and rotational angle recorded by ARToolKit. ……25

3.7 The whole experimental setup. ……27

3.8 Microrobot operational platform. The microrobot walks on a 3-inch silicon wafer. Two piles of pyrex glass lift up the platform. The microscope focuses on the tracking patterns. ……..28

3.9 The power amplifier PCB connecting to the power supply and the NI-DAQ card in the host computer. ……29

3.10 The intermediate PCB connecting the control wires and the power amplifier PCB. ……30

3.11 The thermometer and thermocouple used for measuring the temperature of the microrobot chip and the walking surface. …….31

3.12 The circled position is where the microrobot chip' s temperature is measured. ……31

3.13 The thermocouple was attached on the bottom of the walking surface to measure its temperature. ……32

4.1 (a) Experimental data and curve fitting results of position versus time (b) speed versus time. $V(0)$ and $V(\infty)$ are 178.32 μm/sec and 86.59 μm/sec respectively. ……35

4.2 (a) Experimental data and curve fitting results of position versus time (b) speed versus time. $V(0)$ and $V(\infty)$ are 192.61 μm/sec and 115.77 μm/sec respectively. ……36

4.3 (a) Experimental data and curve fitting results of position versus time (b) speed versus time. $V(0)$ and $V(\infty)$ are 209.40 μm/sec and 120.40 μm/sec respectively. ……37

4.4 (a) Experimental data and curve fitting results of position versus time (b) speed versus time. $V(0)$ and $V(\infty)$ are 224.35 μm/sec and 124.50 μm/sec respectively. ……38

4.5 (a) Experimental data and curve fitting results of position versus time (b) speed versus time. $V(0)$ and $V(\infty)$ are 203.33 μm/sec and 113.53 μm/sec respectively. ……39

4.6 (a) Experimental data and curve fitting results of position versus time (b) speed versus time. $V(0)$ and $V(\infty)$ are 201.90 μm/sec and 111.58 μm/sec respectively. ……40

4.7 (a) Experimental data and curve fitting results of position versus time (b) speed versus time. $V(0)$ and $V(\infty)$ are 190.05 μm/sec and 107.95 μm/sec respectively. ……41

4.8 (a) Experimental data and curve fitting results of position versus time (b) speed versus time. $V(0)$ and $V(\infty)$ are 174.04 μm/sec and 99.71 μm/sec respectively. ……42

4.9 Speed plots of different step frequencies. There is a very similar decaying tendency between these plots. ……43

4.10 The time constants t of different step frequencies. Most of them spread between 6.1 ~ 7.7. ……..44

4.11 The heat power dissipated from one cilia array chip in each phase of the four-phase motion. ……45

4.12 The energy dissipation of 100Hz and 200Hz step frequency. The same amount of energy is dissipated in 0.04 second. ……..46

4.13 Temperature measurements of 100Hz and 200Hz step frequency on (a) microrobot chip (b) walking surface……47

4.14 Calculation results of heat dissipation for different step frequencies in one second. Above 50Hz, the value is almost a constant. ……49

4.15 The comparison of microrobot speed and walking surface temperature. The microrobot ran for 20 seconds, stopped running for 10 seconds and then resumed running for 10 seconds. ……51

4.16 Experimental result, best-fit curve and variation range. It shows that the speed is within variation range. This means that the influence of surface roughness is not severe. ……..53

4.17 Experimental result, best-fit curve and variation range. It shows that the speed is well outside the variation range. This means that the influence of surface roughness is very severe. ……...53

4.18 The comparison of glass A and B. Glass A has a polished surface. Glass B was dipped into HF solution to get a rougher surface. ……..55

4.19 Surface roughness measurement of glass A in Figure 4.18 taken by Cheng-Chun Lee at the Washington Technology Center. The heigth between highest and lowest position is about 0.3μm……..56

4.20 Surface roughness measurement of glass B in Figure 4.18 taken by Cheng-Chun Lee at the Washington Technology Center. The length between highest and lowest position is about 6.5μm……..56

4.21 A schematic of the microrobot. The top and bottom air layers are the main media, which transfer heat dissipated from every micro cilium to the robot chip and the walking surface. ……58

4.22 Microrobot operational platform. The microrobot walks on a 3-inch silicon wafer. Two piles of pyrex glass lift up the platform. The microscope focuses on the tracking patterns. ……60

4.23 Temperature drop due to thermal contact resistance. This plot is scanned from Introduction to Heat Transfer [4]. ……61

4.24 The model for macroscopic simulation. (a) full view of the model (b) highlight of the structure between microrobot chip and walking surface. ……..63

4.25 Temperature comparison of measurement and simulation results in the microrobot chip and the walking surface for heat-up curve. ……66

4.26 Temperature comparison of measurement and simulation results in the microrobot chip and the walking surface for cool-down curve. ……67

4.27 The illustration of the micro cilium and the detailed layout of its structure. The thickness of each layer is shown in the parenthesis. This plot is scanned from John Suh' s dissertation [1]. ……...70

4.28 The illustration of the simulation model representing the micro cilium. The thickness of each layer is shown in the parenthesis. ……71

4.29 The simulation result of the micro cilium. The height of position A and B are 116.73μm and 84.02μm respectively. The X direction bending is 3.83μm. ……..73

4.30 The microrobot can bear at maximum 3.524g consisting of two 16 pin ICs, two 8 pin ICs and 30 staples. ……74

4.31 A 16 pin IC. It is about 2cm and 0.983g. ……75

4.32 An 8 pin IC. It is about 1cm and 0.464g. ……75

4.33 A staple. It is about 1cm and 0.021g. ……..76

4.34 The simulation result of applying force on the micro cilium. (a) front view before applying force (b) front view after applying force (c) side view before applying force (d) side view after applying force ……77

4.35 Schematic of micro cilia array chip and one motion cell. This figure is scanned from John Suh' s dissertation [1]. The T1 through T4 labels mark the thermal control wires and the E1 through E4 labels mark the electrostatic control wires. ……..78

4.36 The solid part of the FSI simulation model. (A) The Ti-W resistor outside the micro cilia (B) the micro cilia ……79

4.37 The composition of the FSI simulation model. (a) solid part (b) fluid part (c) combination. The solid model is enclosed by the fluid model. ……..80

4.38 The length, width and thickness of the fluid part in the simulation model. ……..81

4.39 Fluid-Solid Interaction Solution Algorithm copied from ANSYS manual [6]. ……..82

A.1 Dimension of the microrobot. ..……90

A.2 Position of the microrobot. Dimension of the 3-inch wafer and the pyrex glass ……90

A.3 Side view of the simulation model. The scale is exaggerated for expressing more clearly. Figure A.4 is the list of the material properties corresponding to the indicated material numbers..……91

A.4 Material properties corresponding to Figure A.3. ……91

A.5 Heat power in every phase of the four-phase motion. ……92

A.6 Plot of Equation A.1……...93

A.7 A schematic indicates where the boundary conditions are applied. ….94

A.8 Plot of the heat convection coefficient for the PCB surface……96

A.9 Plot of the heat convection coefficient for the robot chip surface……..96

A.10 Plot of the heat convection coefficient for the wafer surface. ……..97

A.11 Plot of the heat convection coefficient for the Pyrex Glass Surface…97

A.12 Plot of the heat convection coefficient for the Side Surface 1 of Pyrex Glass……..99

A.13 Plot of the heat convection coefficient for the Side Surface 2 of Pyrex Glass……..99

B.1 The material properties used in this simulation cited from John Suh's dissertation……...……100

B.2 The dimension of the micro cilium……101

B.3 The layer structure of the micro cilium. There are three different layer structures in the micro cilium. (1) Top to A (2) A to B (3) B to Bottom. The detailed information of each layer is in Figure B.4, B.5 and B.6……102

B.4 The detailed information of the section 1 (Top to A), corresponding to Figure B.3……103

B.5 The detailed information of the section 2 (A to B), corresponding to Figure B.3……104

B.6 The detailed information of the section 3 (B to Bottom), corresponding to Figure B.3……105

GLOSSARY

t : time constant

Ra_L : Rayleigh number

g : gravitational acceleration

b : volumetric thermal expansion coefficient; for an ideal gas $b \equiv 1/(absolute\_temperature)$

a : thermal diffusivity of fluid

u : kinematics viscosity of fluid

r : density of fluid

L_c : characteristic length

k : thermal conductivity

h : convection heat transfer coefficient

c_p : specific heat

Nu : Nusselt number

$R''_{t,c}$: thermal contact resistance

?: angle (unit: degree)

ACKNOWLEDGEMENTS

I would like to thank my advisor, Professor Karl F. Böhringer for his support, encouragement, and careful editing of this thesis. I also thank Professor Lih Y. Lin and Professor Babak Amir Parviz for serving as the faculties of my defense committee. I also want to thank Dr. Kerwin Wang who provided many useful ideas for me, Dr. Xiaorong Xiong who helped me take the SEM picture of the micro cilia, Cheng-Chun Lee, Eric J. Black who set up the LabVIEW control system and Anshuman Shukla who helped me finish the experiments.

Special thanks go out to my family. To my dad Yung-Lo Chen, to my mom Su-Chung Lai, and to my sister Tsai-Huang Chen. Without their support, I will not be able to overcome many difficulties during this period of time.

Chapter 1

INTRODUCTION

Many applications of microrobots have been envisioned, including industrial inspection, micro assembly, health monitoring, etc. Some microrobots built with MEMS technology have been introduced. There are two important functions in these applications, which are conveying object and positioning to a certain location. All possible applications for these microrobots depend on the degree of understanding of the microrobot for accurate control. In this project, we introduce an omnidirectional microrobot, which has three degrees of freedom (X, Y, ?) motion. It is composed of two micro cilia array chips. Each chip has 256 bimorph thermal actuators as the legs of the microrobot. The initial speed is over 220μm/sec and the steady state speed is over 120μm/sec. Its maximum loading capacity is 3.524g.

1.1 Related Work

Using electrostatic force or thermal expansion force are two common methods for driving a MEMS microrobot. Seth Hollar and others built a solar powered 10mg silicon robot actuated by electrostatic inchworm motors [1]. Figure 1.1 shows the solar powered robot. It has two, one degree of freedom legs and is a combination of three chips. The first chip contains the inchworm motors and the legs, the second chip is the solar cell and the third chip contains CMOS circuitry for controlling the legs. This robot

consumes very low power (22nW). The speed is less then 97µm/sec without slippage.

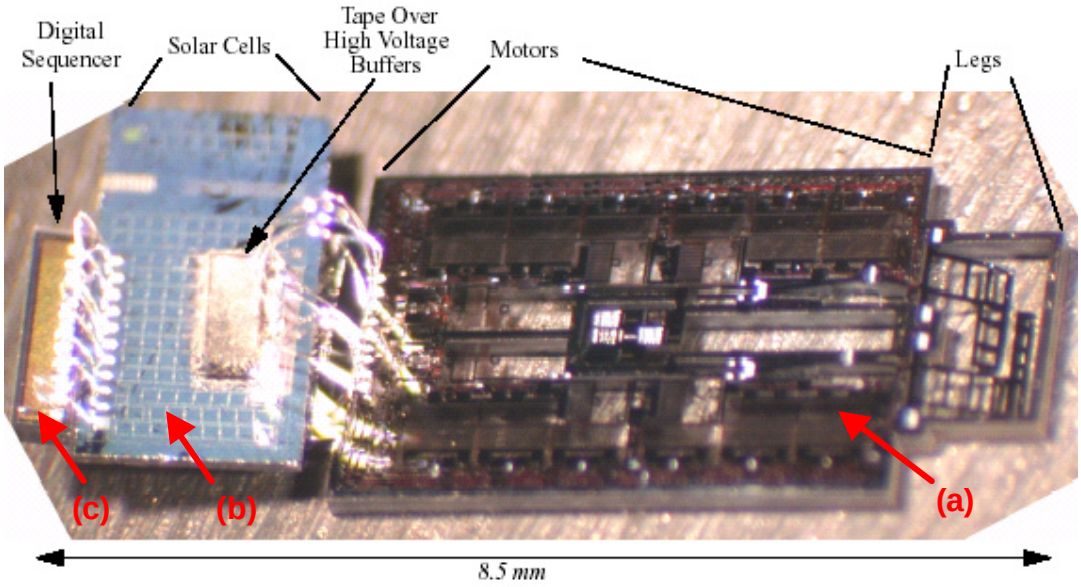

Figure 1.1: Solar powered 10mg silicon robot [1]. (a) electrostatic inchworm motors and two legs (b) solar cells (c) CMOS digital sequencer

The other example of electrostatic microrobot is the untethered microrobot built by Bruce Donald and coworkers [2]. Its body consists of a scratch drive actuator (SDA), which is composed of a thin polysilicon plate with a bushing at the front end. Figure 1.2 shows its design and how it moves. The walking surface is covered with a sequence of insulated electrodes. The electrodes build a voltage, V_{plate} on the robot, governed by Equation 1.1 [2]. V_1 and V_2 are the applied voltages and the C_1 and C_2 are the capacitances across the surface electrodes and the robot.

$$V_{plate} = \frac{V_1 \cdot C_1 + V_2 \cdot C_2}{C_1 + C_2} \quad \text{.....(1.1)}$$

The experimental result shows that its speed can be up to 1.5mm/sec and it has ability to push small objects.

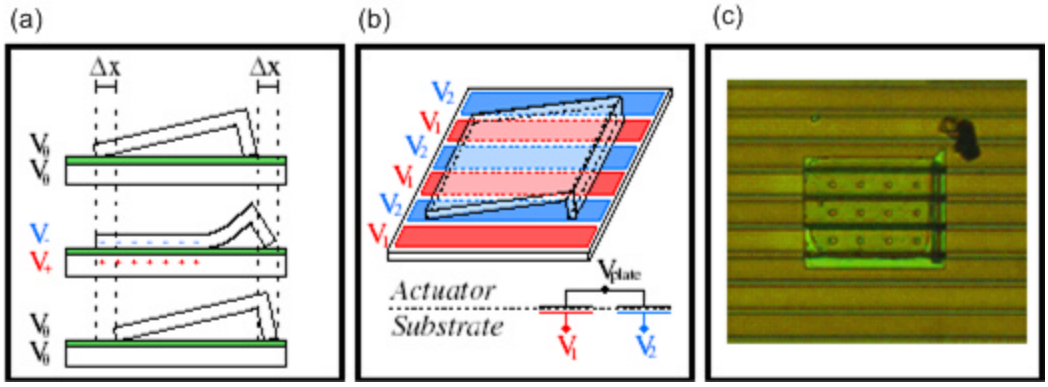

Figure 1.2: Untethered micro actuators for autonomous micro-robot locomotion [2]. Its dimension is usually 100μm×80μm×(1~2μm) (a) a schematic shows how the robot moves. (b) the V_1 and V_2 electrodes build a voltage potential, V_{plate}. on the robot (c) An optical micrograph of the untethered robot.

Using thermal expansion force to actuate microrobot is the other common method. It could be from the thermal expansion difference in the structure or two combined materials with different coefficients of thermal expansion (CTE). The structure tends to bend toward the high CTE side if its temperature is lower then the annealing temperature. Increasing the temperature reverses the situation. As heat source, a common method is to integrate a high resistance material, for example Ti-W or polysilicon, as a thermal resistor. P. E. Kiaditis, V. M. Bright, K. F. Harsh, and Y. C. Lee developed a thermal actuated microrobot to mimic the way six legged insects walk [3]. Its size is 10mm×10mm×0.5mm and the legs can move with two degrees of freedom. Figure 1.3 shows the structure and the dimension of the legs. One side of the polysilicon leg is larger than the other side. Because the wider side expands less when an electric current is passed through the leg, the legs bend toward the wider side. The electro-

thermal actuator array shown in part (a) of Figure 1.3 drags the leg back and forth. This creates the second degree of freedom. The experimental result shows that its speed was 7.55μm/sec at maximum step size of 3.75μm and it was able to transport a 3.06mg mass [3].

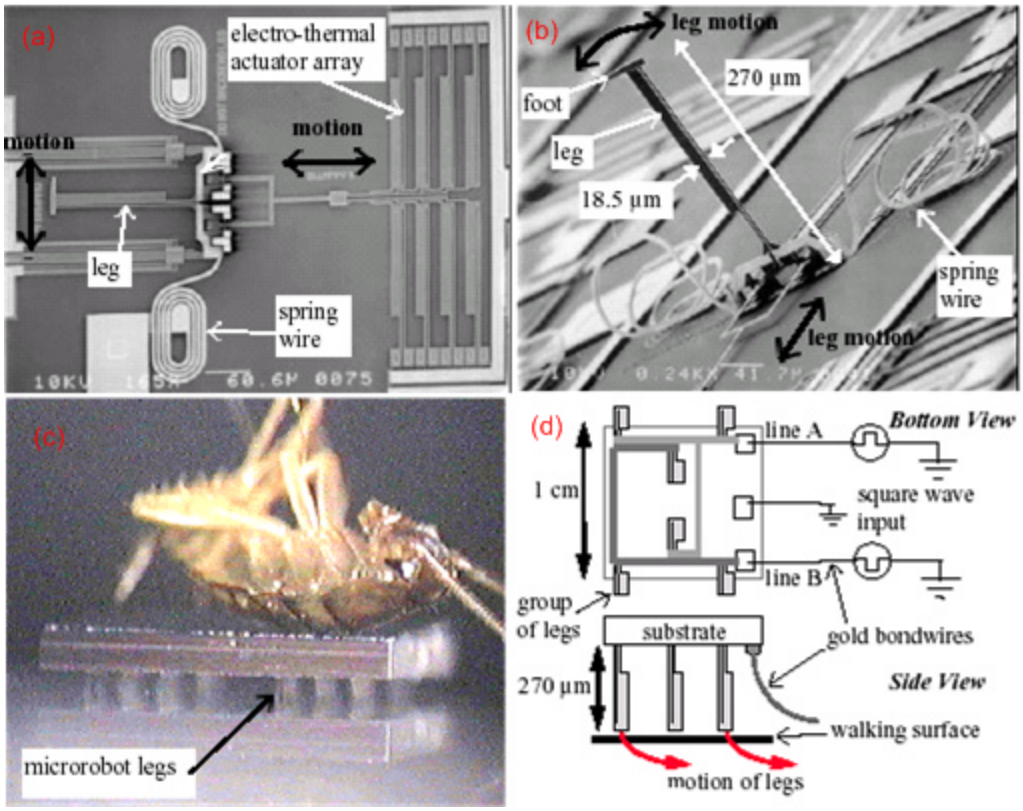

Figure 1.3: Prototype microrobots made with polysilicon micromachining [3]. (a) a SEM picture indicates the structure of the two degrees of freedom leg. (b) dimension of the leg (c) demonstration of bearing an insect (d) a simplified wiring diagram

T. Ebefors, J. U. Mattson, E. Kaelvesten, and G. Stemme declared developing the first walking batch fabricated silicon micro robot able to carry loads [4]. The size of this microrobot is 15mm×5mm×(1 or 1.5)mm. The length of legs is 0.5 or 1mm. Its speed is up to 6mm/sec. The robot' s maximum loading capacity is 2500mg. Part (a) of Figure 1.4 shows the

design of the leg. The movement of each leg is based on a joint with four V-grooves. The V-grooves are filled with polyimide and connected by three polysilicon heaters. Because the long side of the polyimide expands or shrinks more then the short side, the motion of the leg is generated with the changing of the temperature in the V-groove. Part (b) of Figure 1.4 shows the operation principle for driving the microrobot and part (c) is the load test of its maximum 2500mg load capacity.

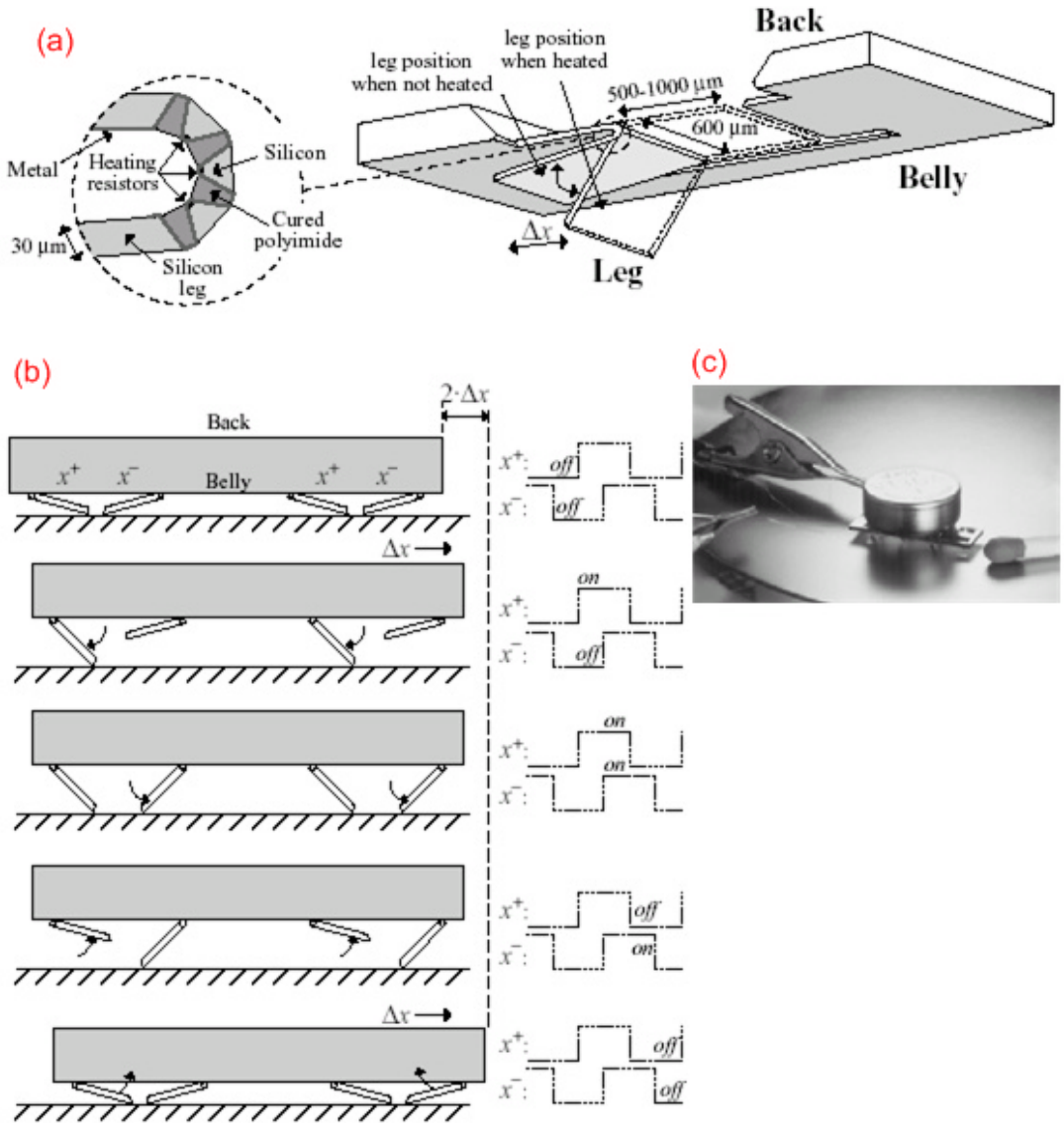

Figure 1.4: A walking silicon microrobot [4]. (a) the design of one leg (b) the operation principle for driving the microrobot (c) the load test of its maximum 2500mg load capacity

1.2 Previous Research of the Micro Cilia Array Chip

The micro cilia array chip was invented by Dr. John Suh [5]. The microrobot is only one of its feasible applications. Its original application was as a distributed microactuator surface for precise positioning and orienting of small parts [6] using programmable force fields [7]. Robert B. Darling used the micro cilia array chip as a positioning stage inside a scanning electron microscope [8]. Mason Terry and his coworkers developed a docking system for microsatellites [9] using the micro cilia array chip. Figure 1.5 shows the idea of the docking system. The free-fly miniature satellites are proposed to dock in a space facility. The landing ground will be tiled with micro cilia array chips and the micro cilia will position the miniature satellite to an accurate alignment.

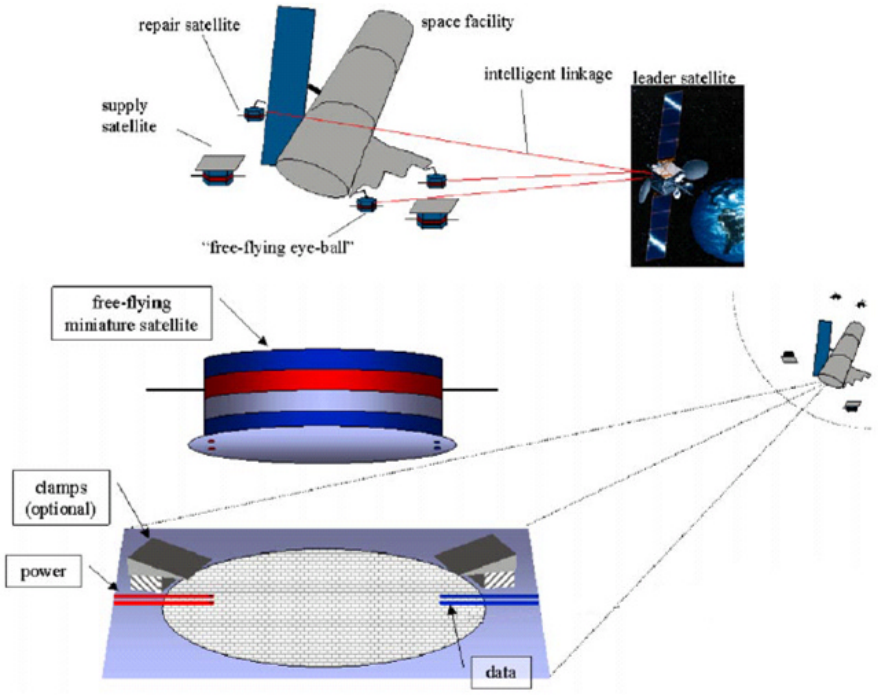

Figure 1.5: A schematic shows the idea of the docking system [9].

Figure 1.6 shows the experimental setup and Figure 1.7 is the picture corresponding to Figure 1.6. The puck is used to simulate a miniature satellite. The air table lifts up the puck using air force to eliminate the influence of friction. The slop adjust knob changes the angle of the air table and also changes the normal force on the micro cilia chips. The experimental result demonstrates a 4cm^2 cilia array capable of docking a 41.2g picosatellite with a 2cm^2 contact area with micrometer precision [9].

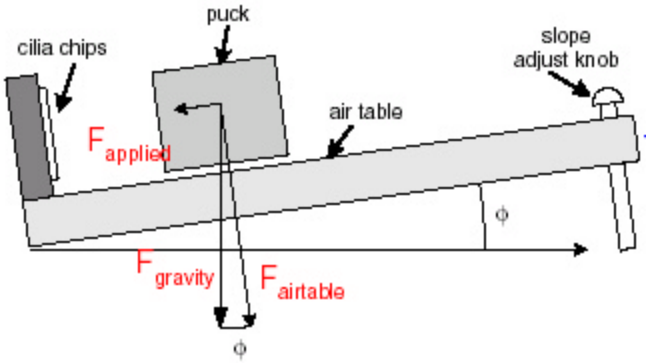

Figure 1.6: The experimental setup of the docking system [9]. The air table lift up the puck using air force and the slope adjust knob changes the normal force on the micro cilia array chips.

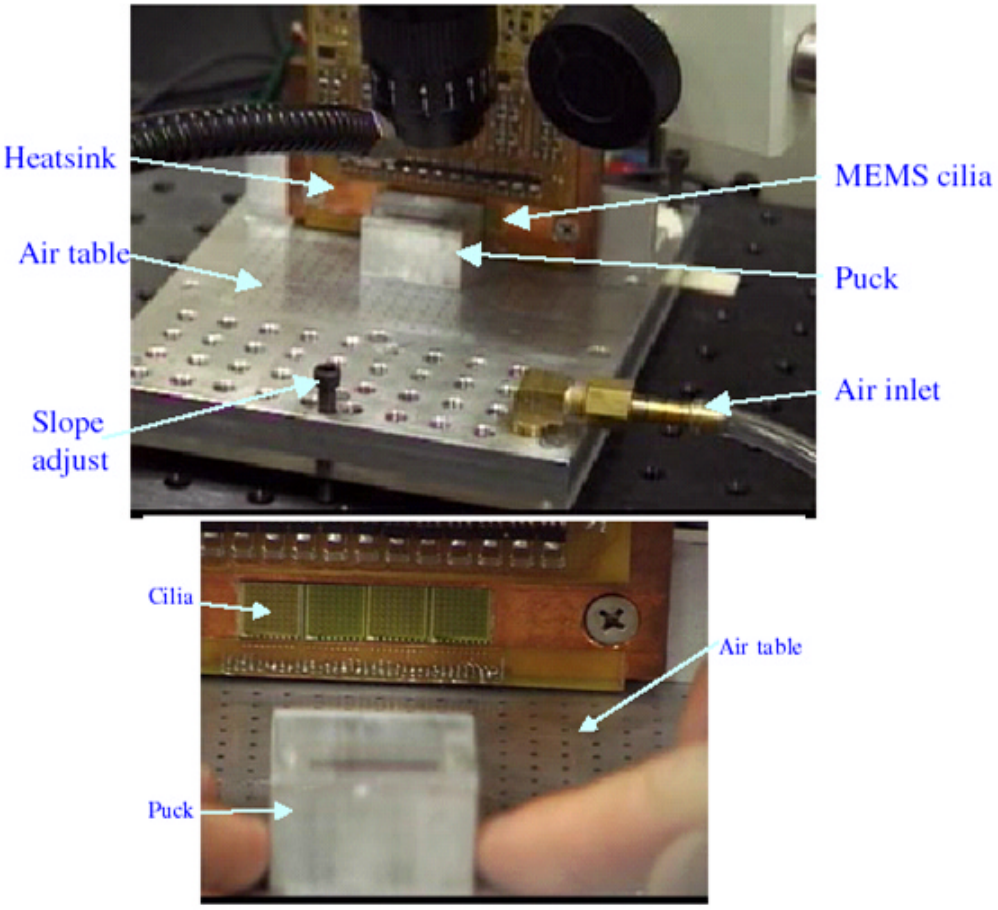

Figure 1.7: The experimental setup pictures of the docking system related to Figure 1.6 [9].

The other significant application of the micro cilia array chip in our lab is the microrobot. Matthew Mohebbi, Mason Terry and Karl F. Böhringer [10] hypothesize that the microrobot' s motion is governed by Equation 1.2. x(t) is the microrobot' s position and t is time. The parameters a, b, and t depend on the operation of the microrobot. Further verification of this model is discussed in Chapter 4.

$$x(t) = at + b(1 - e^{-t/t}) \quad \text{.....(1.2)}$$

The durability of this microrobot was also tested in their work. During testing of the microrobot each cilium has performed approximately 832k actuations with zero failures [10].

1.3 Overview of Thesis

As described above, a microrobot could have various usages. However understanding it is the key issue for assigning a microrobot to proper applications. In this research, we try to systematically understand our microrobot' s characteristics. Chapter 2 is the overview of the microrobot from its structure to its mechanism. Chapter 3 introduces the microrobot's motion tracking system, the controller board, and the experimental setup. Chapter 4 discusses the results of experiments and simulations. The conclusion and future work are described in Chapter 5. Appendix has detailed simulation procedures.

Chapter 2

MICROROBOT OVERVIEW

This chapter gives an overview of the microrobot including the size, the mechanism and the structure of the micro cilium.

2.1 Microrobot Size

The microrobot consists of two 10mm×10mm micro cilia array chips. These chips are firmly bonded to an 18.0mm×12.8mm printed circuit board (PCB). The mass of the microrobot is 0.478g. There are 10 contacts on top of the PCB and another 10 contacts on bottom, connected to the top by vias through the PCB. The PCB is electrically connected to the two chips by gold bond wires at the bottom contacts and electrically connected to nine 25μm diameter control wires at the top contacts, which is from American Wire Gauge (both chips share a common ground wire). Its classification is CDA 110 (the copper grade) and H-Poly Green (insulation type). The wires can be bonded by a normal soldering tool but the insulation needs to be carefully removed. Using soldering iron to burn out the insulation is one way to remove it. Figure 2.1 shows the soldering equipment. Figure 2.2 and 2.3 show the top view and bottom view of the microrobot respectively.

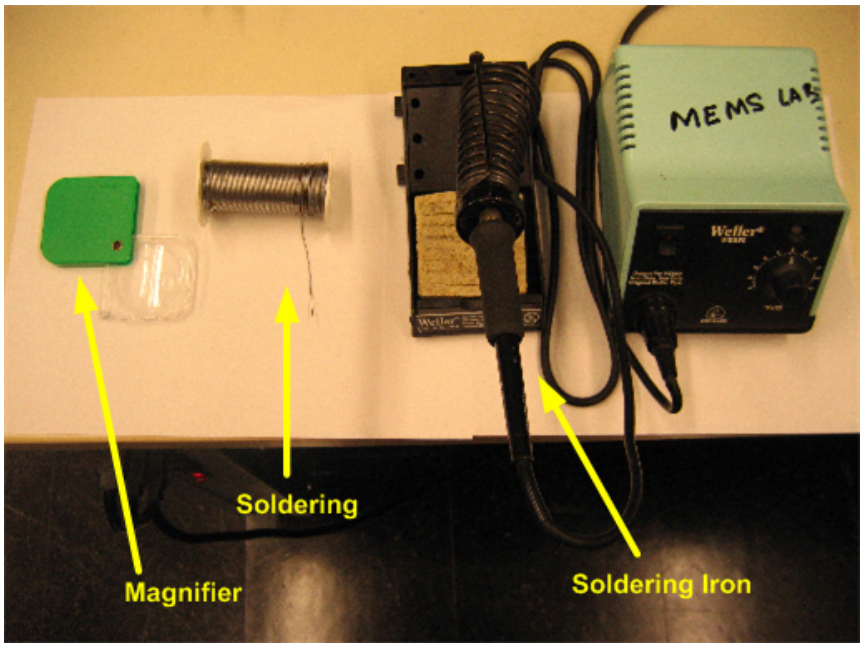

Figure 2.1: The soldering equipment for bonding the control wires on top of the PCB.

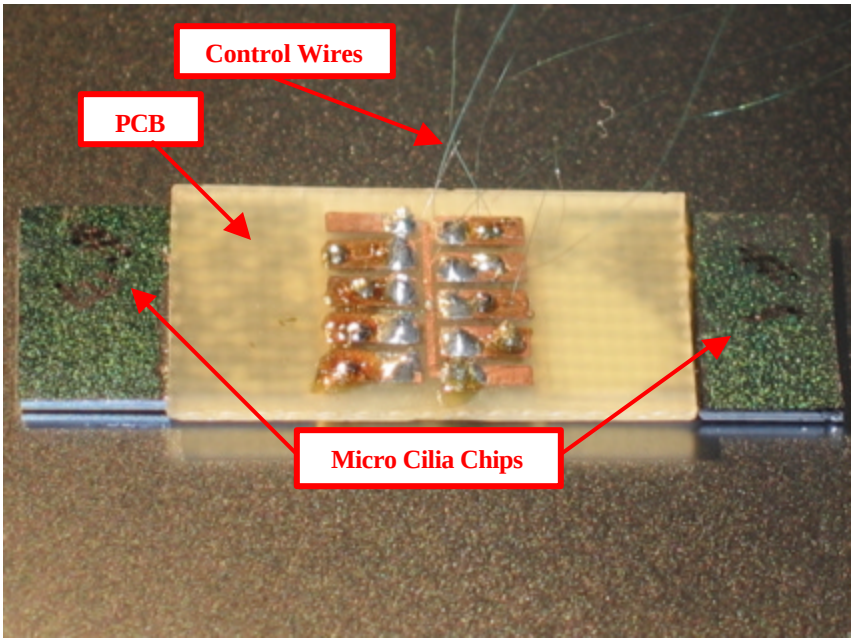

Figure 2.2: Top view of the microrobot. The printed circuit board (PCB) bonds two micro cilia array chips, thus forming the backbone of the microrobot. The contacts on the PCB electrically connect to control wires.

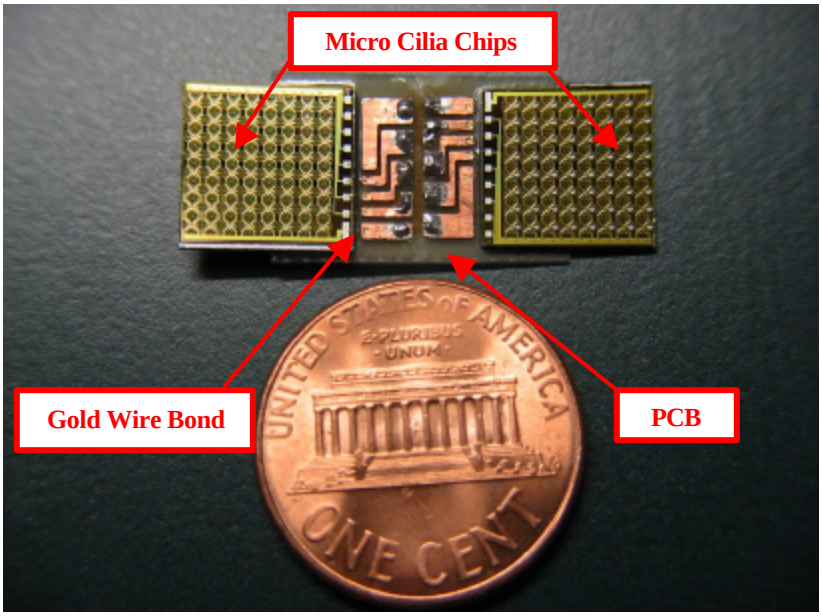

Figure 2.3: Bottom view of the microrobot. The printed circuit board (PCB) bonds two micro cilia array chips. The contacts on the PCB electrically connect to two chips via gold wires.

Figure 2.4 is a schematic of the microrobot. The microrobot's size is about 30mm in length, 10mm in width and the height is about 1mm.

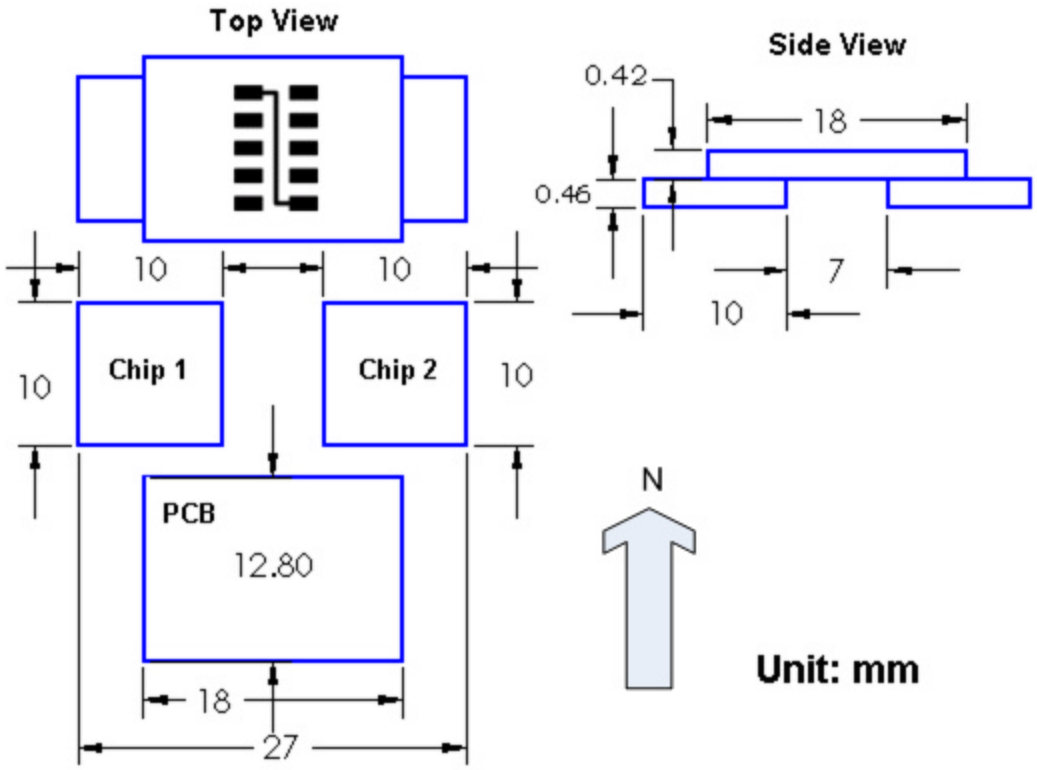

Figure 2.4: The schematic of the microrobot. The microrobot' s size is about 30mm×10mm×1mm.

2.2 Micro Cilia Array Chip

Every micro cilia array chip is 10×10mm and there are 8×8 motion cells in each chip. Figure 2.5 shows the chip and highlights one motion cell. Figure 2.6 is a Scanning Electron Microscope (SEM) picture of motion cells in the unheated state. Each motion cell is 1.1×1.1mm. The micro cilia in each motion cell are independently actuated by four thermal and four electrostatic wires. The thermal wires are labeled as T1 through T4 and the labels E1 through E4 indicate electrostatic wires. All 64 actuators with the same orientation are connected together and therefore actuated together.

In practice, electrostatic actuation has not been used in John Suh's experiments [5]. When the actuators are in the full upward position, 500V of applied bias only produces a downward tip deflection of 15μm. With the help from thermal actuation to pull down the actuators, the holding voltage is 70V. Because a small contribution needs a lot of effort, the electrostatic actuation is not used in the microrobot. For thermal actuation, each wire connects through the Ti-W resistors of the 64 actuators in a series-parallel combination. This makes the overall resistance of 64 actuators the same as that of a single actuator. Figure 2.7 shows the resistance of T1 through T4 and their corresponding contacts on top of the PCB. Part (a) is the orientation of the micro cilia in each motion cell viewed from bottom of the microrobot. The PCB electrically connects the control wires on top and the micro cilia array chips on bottom. The top and bottom contacts connect through vias. Part (b) shows how the contacts for control wires correspond to each micro cilium in the motion cell. Part (c) is the resistance measured from each contact in part B to the power contact.

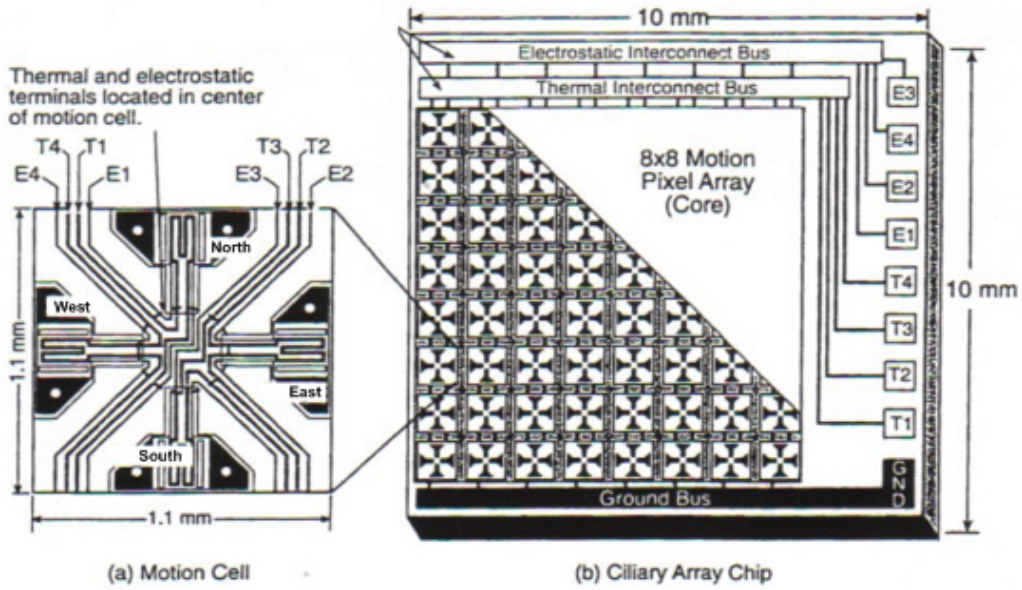

Figure 2.5: Schematic of micro cilia array chip and one motion cell. This figure is scanned from John Suh' s dissertation [5]. The T1 through T4 labels mark the thermal control wires and the E1 through E4 labels mark the electrostatic control wires.

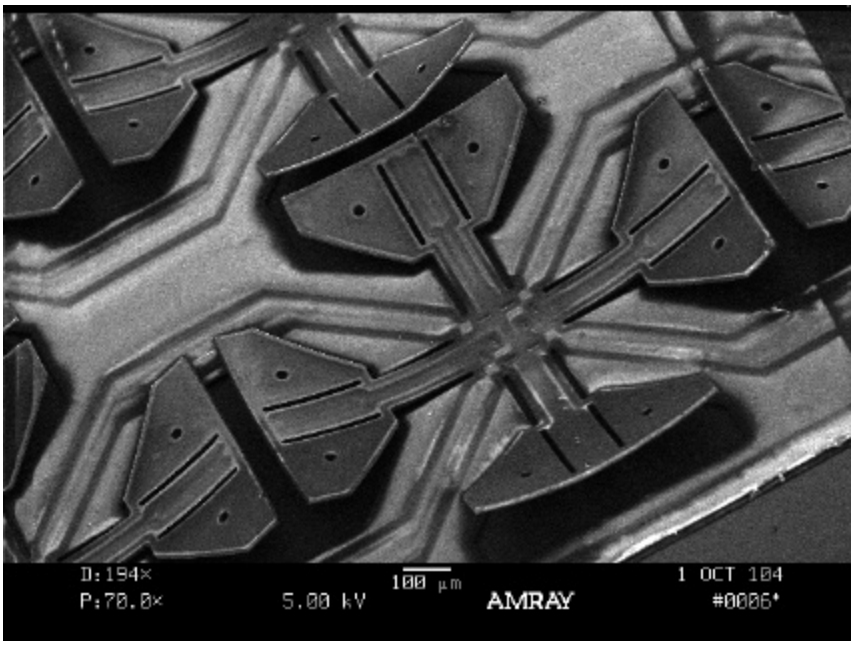

Figure 2.6: SEM picture of the motion cells in the unheated state taken by Xiaorong Xiong at the Washington Technology Center.

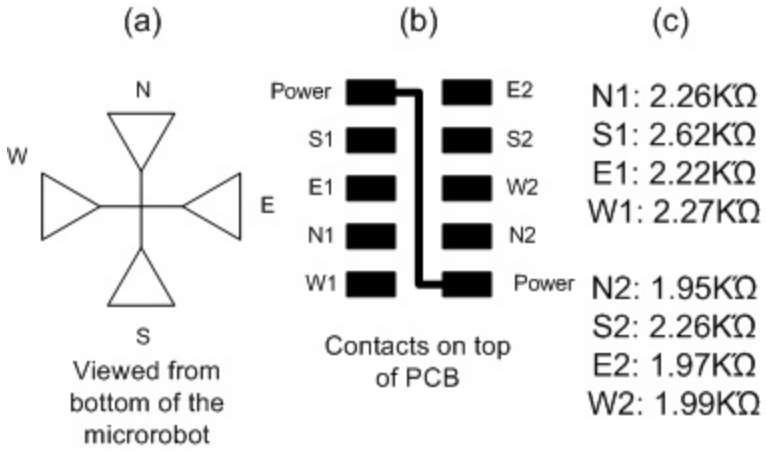

Figure 2.7: The resistance of thermal control wires and the corresponding contacts on top of PCB. N1~W1 is for chip 1 and N2~W2 is for chip 2.

2.3 Micro Cilium Actuator

The micro cilium is a thermal bimorph actuator. Its main structure consists of two polyimide layers with different thermal expansion coefficients and a Ti-W resistor embedded between the polyimide layers. Figure 2.8 shows the detailed layout of the micro cilium.

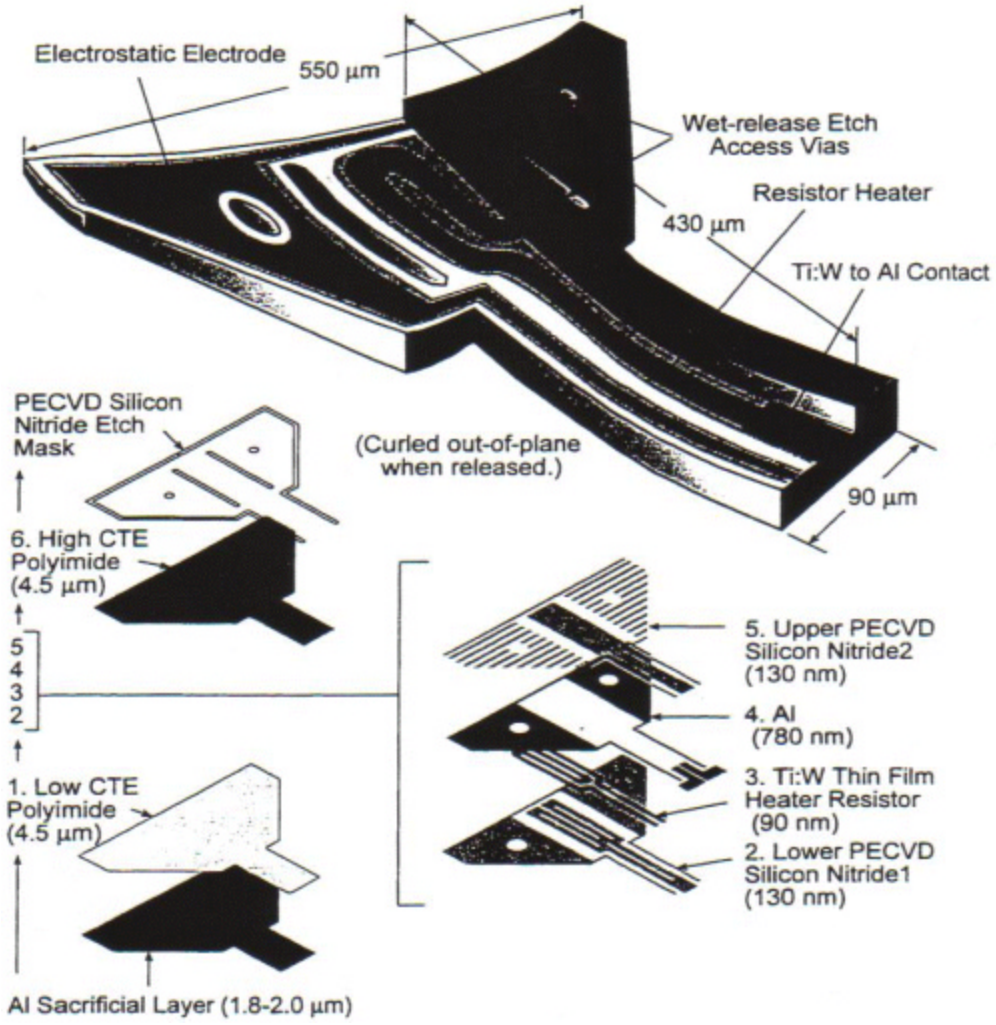

Figure 2.8: The illustration of the micro cilium and the detailed layout of its structure. The thickness of each layer is shown in the parenthesis. This plot is scanned from John Suh' s dissertation [5].

The dimension of the actuator is about 430×550×10μm. It curves toward the side of higher thermal expansion coefficient and is totally flat at 623K. Figure 2.9 is a SEM picture, which shows the lift-up height of the micro cilium in the unheated state. At position A and B, the heights are about 91μm and 117μm respectively.

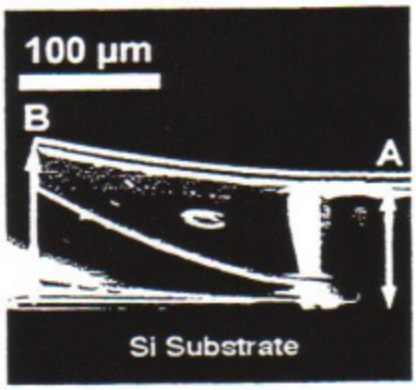

Figure 2.9: A SEM picture scanned from John Suh' s dissertation [5] shows the lift-up height of the micro cilium in the unheated state. The heights at position A and B are about 91µm and 117µm respectively.

From Figure 2.7, averagely the resistance is 2.2kΩ per micro cilium. However there is about 1.5kΩ inside every micro cilium. The rest of it comes from the wiring outside the micro cilium actuator.

Chapter 3

EXPERIMENTS AND METHODS

This chapter talks about the microrobot's motion tracking software, the four-phase motion, the experimental setup and how temperature was measured.

3.1 Four-Phase Motion

On each chip, there are four sets of actuators, which are the microrobot' s legs. These eight sets of legs can be operated independently. This makes the microrobot capable not only of motion in X and Y direction but also of turning to any angle by moving two chips in opposite directions. It means this microrobot has three degree of freedom (X, Y, θ). To simplify the situation, the microrobot' s motion is only tested in a single direction toward east in this project. A four-phase motion is adopted for microrobot control. Figure 3.1 shows the function of four-phase motion. In every cycle of four-phase motion, the robot walks two steps forward. There are two terms, gait frequency and step frequency, used to describe how fast the robot' s legs move. For example, if the robot finishes 25 cycles of four-phase motion in one second, the gait frequency is 25Hz. Because there are four steps in each four-phase motion, the step frequency is 100Hz. In part (a) of Figure 3.1, the red color means the legs lift up. Part (b) of Figure 3.1 only shows two legs to express the four-phase motion, because the north and south legs have no contribution towards moving the robot forward towards the east. The voltage used to actuate the robot is 60V and the LabVIEW code

written by Eric J. Black, an alumnus of the EE MEMS group at University of Washington, is used to control the microrobot.

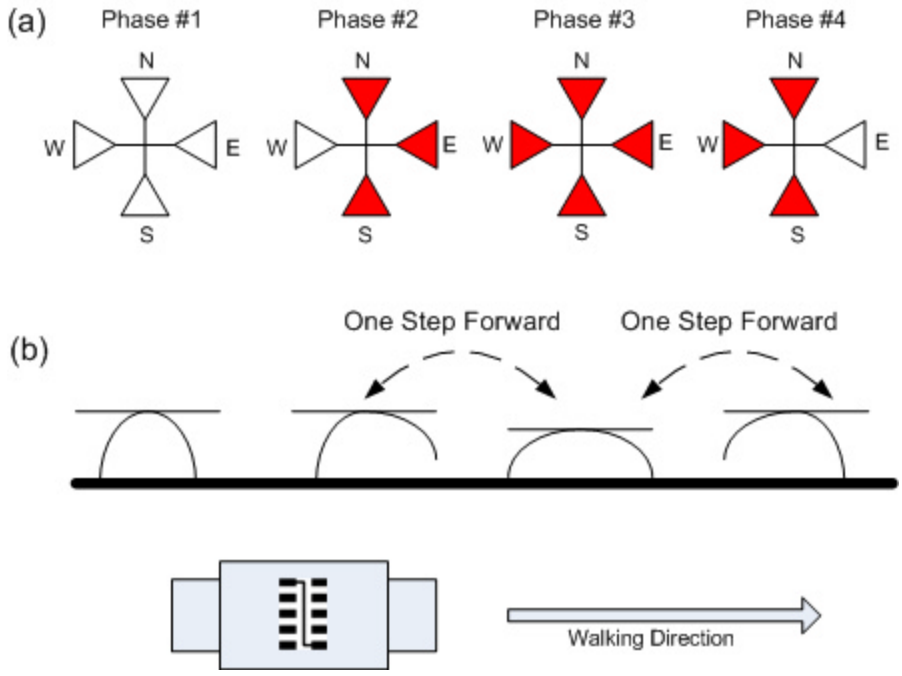

Figure 3.1: A schematic of the four-phase motion. (a) A schematic of one motion pixel. The red color means the leg lifts up. (b) A side view of the four-phase motion corresponding to part (a).

Figure 3.2 shows the LabVIEW interface. This LabVIEW code allows an operator to control the two micro cilia array chips separately but the step frequency is the same for both chips. This code also allows the robot moving diagonally. The basic idea of moving diagonally is still the four-phase motion. For example, the robot walks toward NE direction. The north and east legs are seen as one leg and actuated together. The west and south legs are seen as the other leg. Based on the four-phase motion, these two legs move the microrobot toward NE direction. Besides four-phase motion, there is also a three-phase motion, which skips phase 1 in

Figure 3.1. The idea is to increase the duty cycle of the motion but it is not effective. Jumping from phase 4 to phase 2 causes the robot moving backward. In experiments, the three-phase motion is much slower then the four-phase motion. The setting of quiescent time on the control panel is to turn off the power for a few milliseconds between every cycle of motion. The idea is to decrease the temperature of the robot and the walking surface to boost the speed but it also decreases the duty cycle of the motion. However the effectiveness of the quiescent time has not been studied yet.

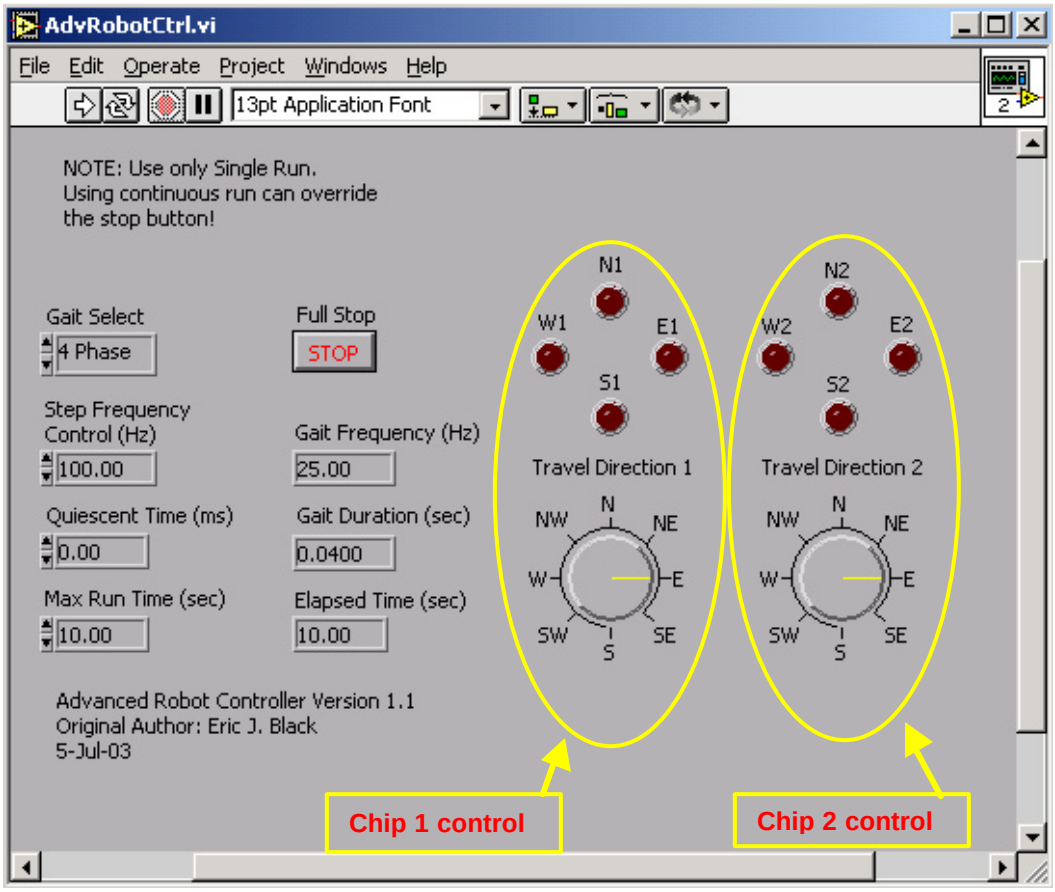

Figure 3.2: LabVIEW interface for microrobot control. It allows an operator to control the motion of the two micro cilia array chips separately.

3.2 Motion Tracking Software

Using the four-phase motion, the microrobot's fastest speed is about 120μm/sec. This is still very difficult to distinguish for the human eye. A proper motion tracking method, which can record the nuance of movement, is required here. The software named ARToolKit is adopted here. It is from the Human Interface Technology Laboratory at the University of Washington. ARToolKit is an augmented reality tool, which can overlay virtual images on the real world for 3D Computer Supported Collaborative Work (CSCW) and many other applications. Only a part of its functions is used in this project to track the motion of the microrobot. The basic principles of how ARToolKit works are as follows. First, a video image is sent into ARToolKit and then ARToolKit searches for square-shaped markers on every frame. Figure 3.3 and 3.4 show the eight markers used in this project and their dimension respectively. The patterns inside the markers are their identifications. ARToolKit can capture several markers at the same time. Second, if the markers are found, the software calculates the position of the camera relative to the markers. Third, the software adds 3D shapes on top of the markers. The ARToolKit screen will show the image of the real world with the virtual shapes on top of the markers. For more information, please refer to http://www.hitl.washington.edu/artoolkit/. The frame rate of the software is about 8 frames per second. ARToolKit not only can provide X, Y and Z position of the markers but also can provide the rotational angles relative to the axes. However in this project, we assume that the microrobot walks on the X–Y plane and only record the X, Y position and rotational angle in the X–Y plane. The tracking markers are printed on a strip of paper and put on the microrobot for ARToolKit to track

the position of the robot. Figure 3.5 shows how the tracking markers are put on the robot. A CCD camera attached on the microscope is used to capture the image of the tracking markers and send it to ARToolKit. Figure 3.6 shows the ARToolKit interface.

Figure 3.3: Eight tracking markers. ARToolKit can recognize these markers and record their positions and rotational angle.

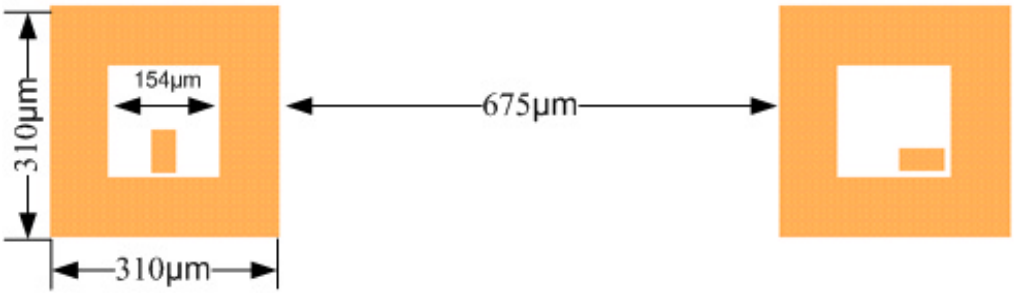

Figure 3.4: The dimension of the tracking markers.

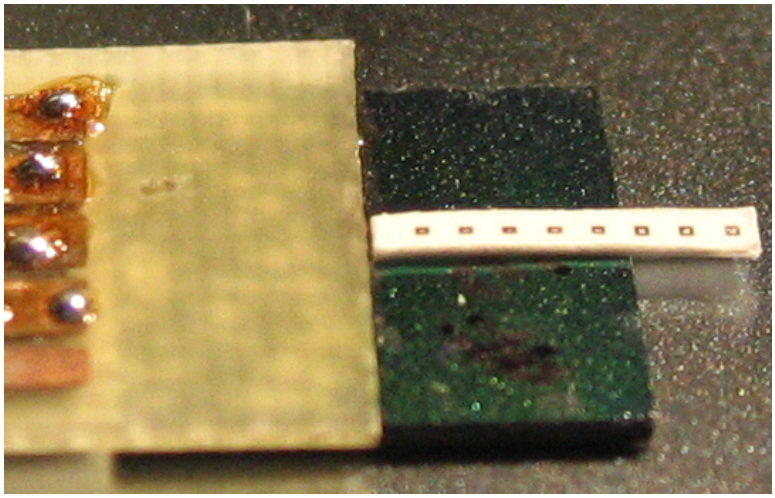

Figure 3.5: The eight tracking markers are printed on a strip of paper and put on the microrobot.

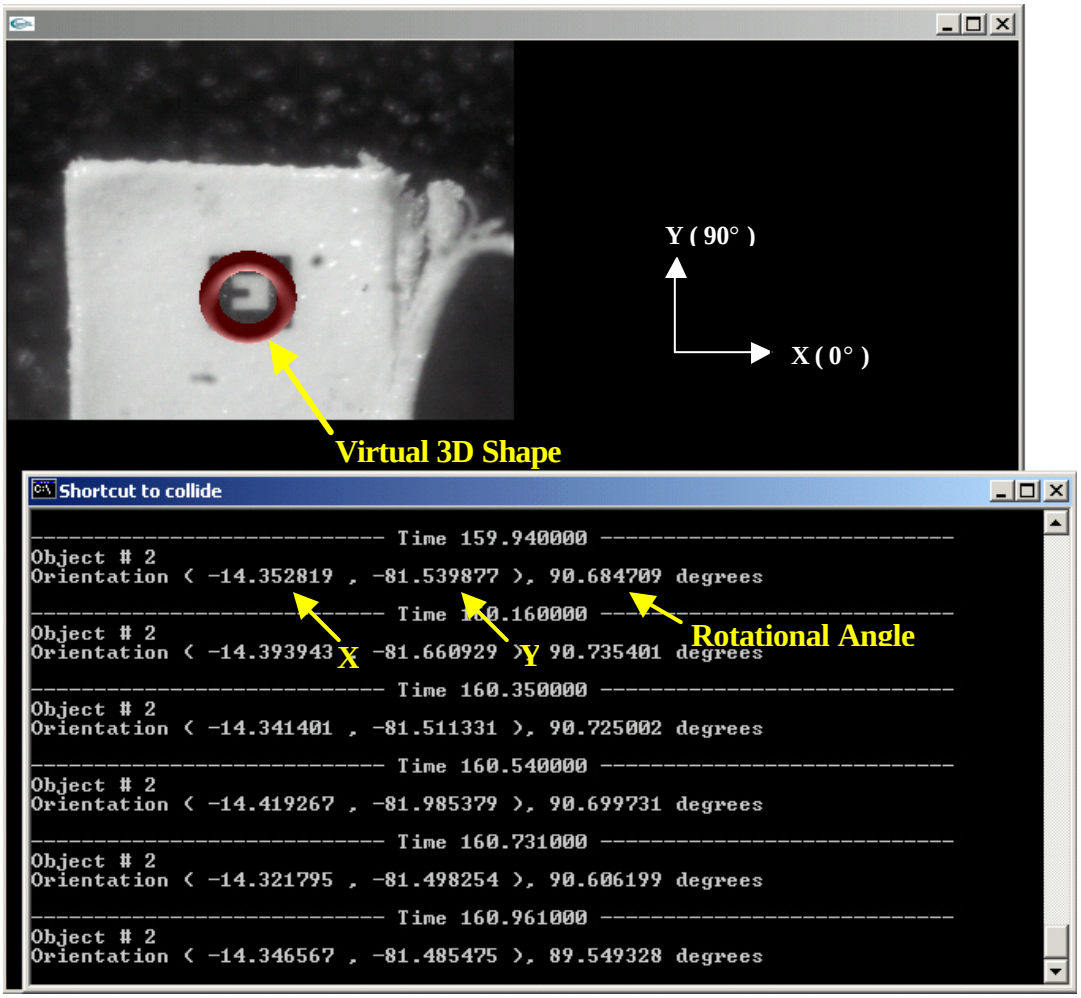

Figure 3.6: ARToolKit interface. The upper part is the output screen of ARToolKit. ARToolKit puts a virtual 3D shape on the recognized tracking marker. The bottom window shows the position and rotational angle recorded by ARToolKit.

Because the image of the tracking markers is captured through a microscope, calibration is needed to link ARToolKit' s coordinate system to the coordinate system of the real world. In this project, the calibration was done manually because it has not been figured out how to specify the calibration in the software. The procedure of manual calibration is as follows. First, the ARToolKit screen is 320 pixels×240 pixels. The total ARToolKit units from left to right and from top to bottom are 263 and 234 units

respectively. Therefore one pixel is 0.822 and 0.975 ARToolKit units in X and Y direction respectively. Second is to put a pattern, whose dimension is known, under the microscope and then calculate the distance of one pixel. After this, the distance of one ARToolKit unit can be found out.

ARToolKit generates a file where the (X, Y, ?) values for each marker are stored together with a time stamp for each frame. ARToolKit can recognize multiple markers in the same frame. This is very useful for keeping track of longer motions, during which several markers pass through the entire limited field of view of the microscope camera. Figure 3.7 shows the whole experimental setup and Figure 3.8 highlights the setup of the microrobot. The microrobot walks on the unpolished side of the three-inch wafer. Two piles of pyrex glass lift up the wafer. This makes it easier to measure the temperature of the walking surface.

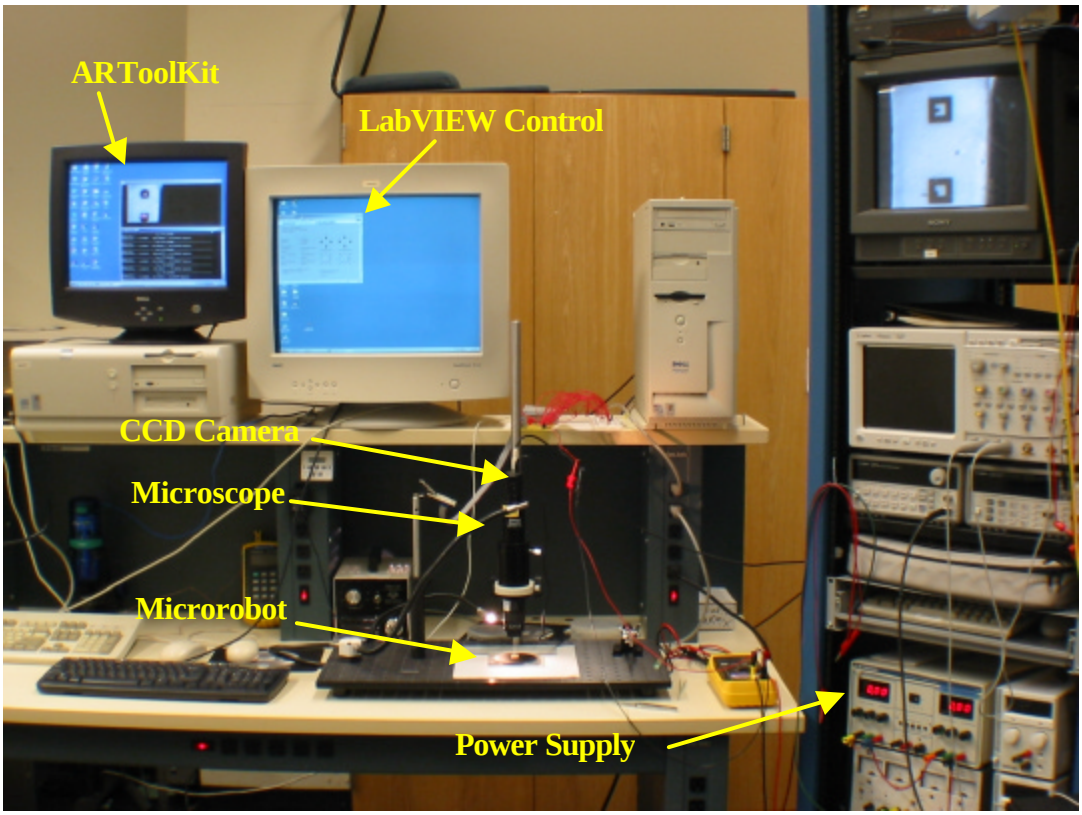

Figure 3.7: The whole experimental setup.

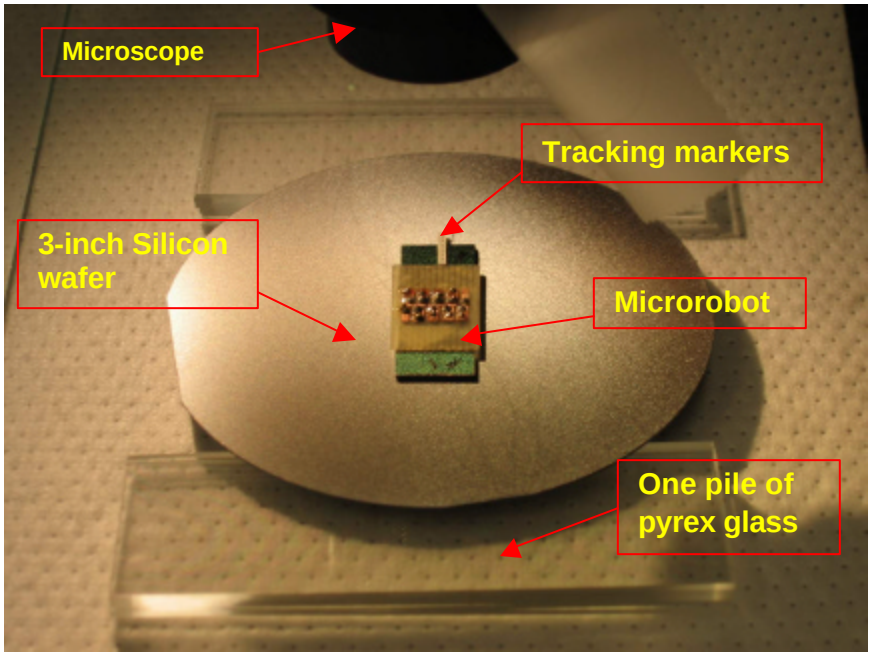

Figure 3.8: Microrobot operational platform. The microrobot walks on a 3-inch silicon wafer. Two piles of pyrex glass lift up the platform. The microscope focuses on the tracking patterns.

3.3 Controller Board

This microrobot is actuated by 60V but the computer can only provide 5V and limited current. A power amplifier PCB is the interface between the computer and the microrobot. A power supply connecting to the power amplifier PCB provides a 60V power source. A NI-DAQ card is installed in the host computer and controlled by the LabVIEW code. This enables the host computer to send 5V to the eight transistors on the power amplifier PCB. These transistors (2N3904) control the current through each set of the legs and there are eight LEDs indicating the on/off state of the transistors. Because the control wires on the robot are too fragile to directly connect to the power amplifier PCB, an intermediate PCB is used to bond the control

wires and connect to the power amplifier PCB. Figure 3.9 shows the power amplifier PCB and Figure 3.10 shows the intermediate PCB.

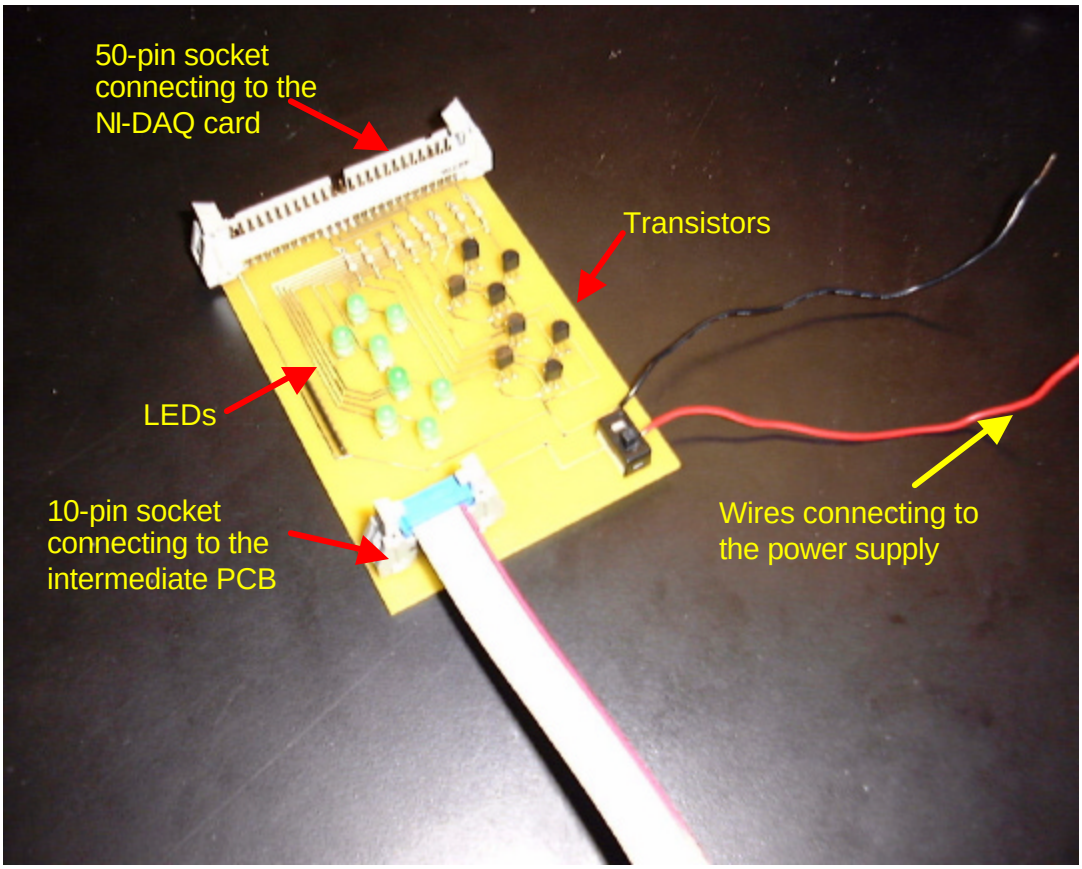

Figure 3.9: The power amplifier PCB connecting to the power supply and the NI-DAQ card in the host computer.

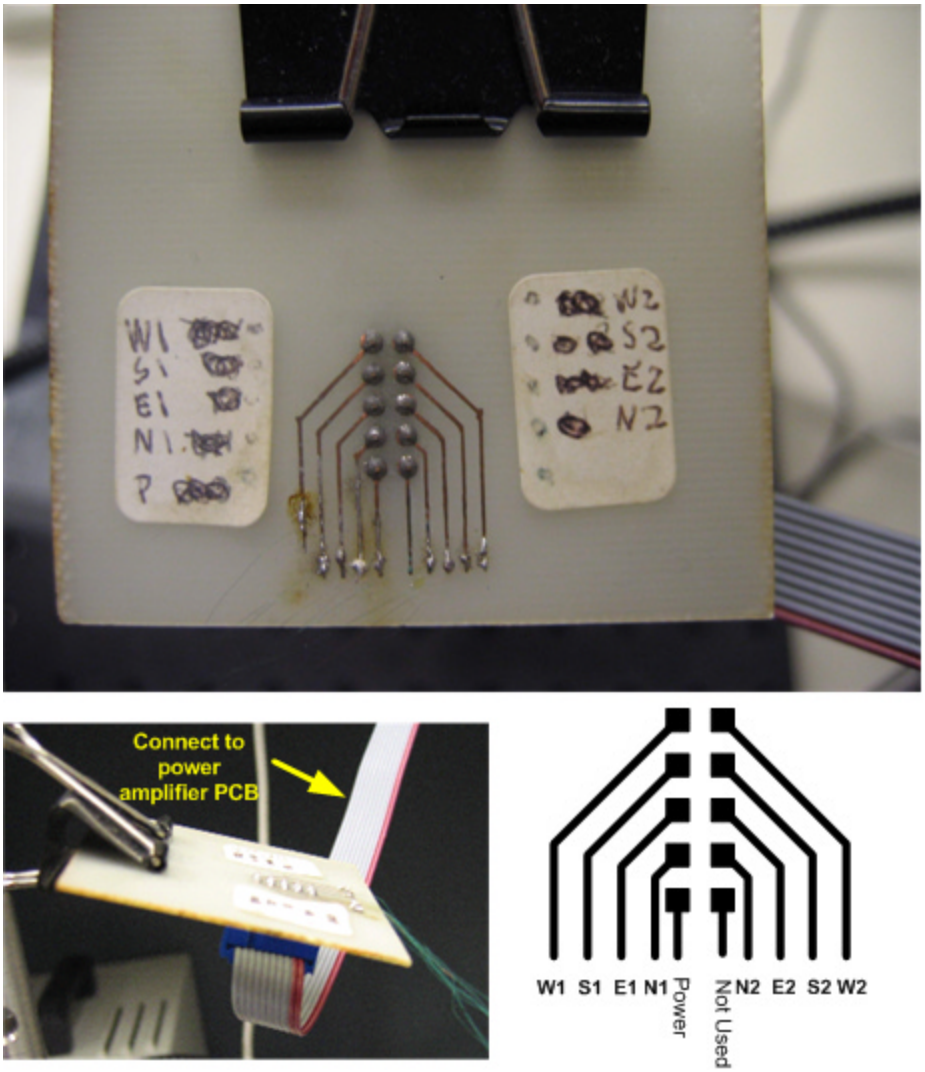

Figure 3.10: The intermediate PCB connecting the control wires and the power amplifier PCB.

3.4 Temperature Measurement

The temperature of the microrobot chip and the walking surface influences the microrobot' s performance and is also used as a calibration reference in the macroscopic simulation introduced in Section 4.5.2. Presently the thermometer with a thermocouple is the only equipment in the lab for

measuring temperature. The thermometer is OMEGA HH501BK and its reading rate is one time per second. The material of the thermocouple is Nickel-Chromium vs. Nickel-Aluminum. Figure 3.11 shows the thermometer and the thermocouple.

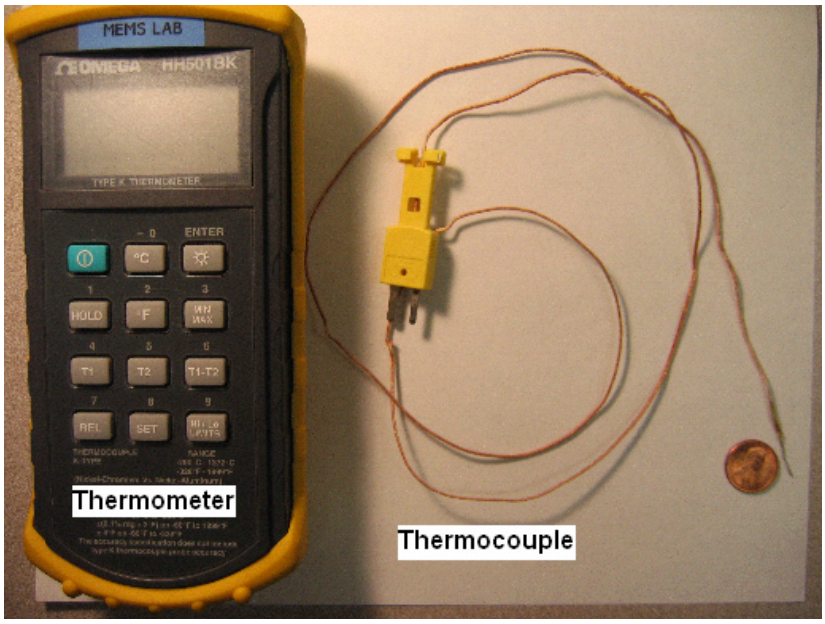

Figure 3.11: The thermometer and thermocouple used for measuring the temperature of the microrobot chip and the walking surface.

For measuring the robot chip's temperature, Figure 3.12 indicates the position of measurement.

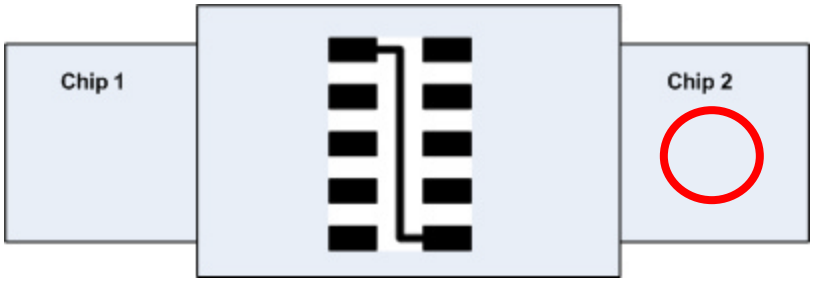

Figure 3.12: The circled position is where the microrobot chip' s temperature is measured.

To influence the robot' s motion as little as possible, the thermocouple was held by hand and lightly touched the robot chip. To measure the temperature of the walking surface, the thermocouple was attached on the bottom of the walking surface, which is the polished side of the 3-inch wafer. Figure 3.13 shows how the thermocouple was attached.

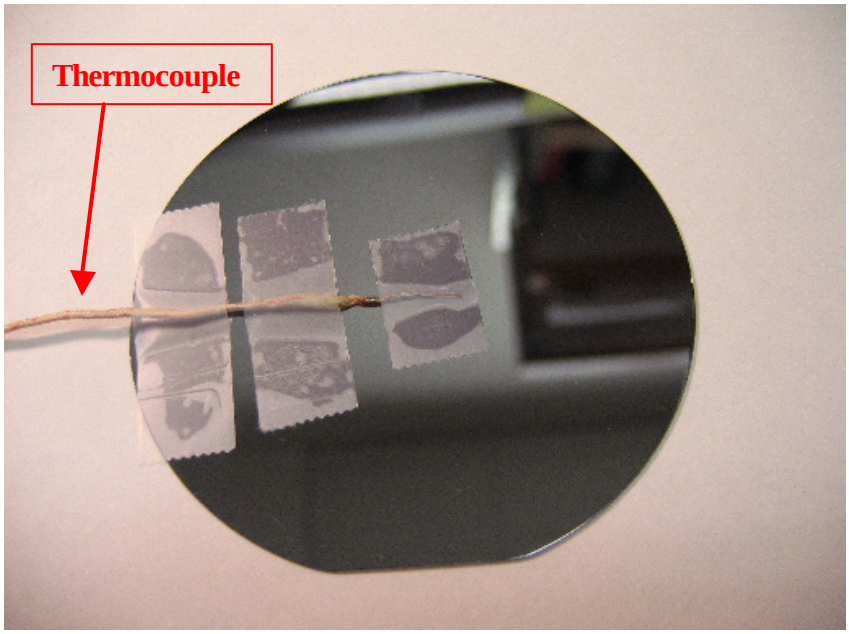

Figure 3.13: The thermocouple was attached on the bottom of the walking surface to measure its temperature.

Chapter 4

RESULTS AND DISCUSSION

The purpose of this project is to understand this microrobot and discover its characteristics as much as possible. Section 4.1 to 4.4 discuss the microrobot speed, the heat dissipation of different step frequencies, the correlation between temperature and speed, and the influence of surface roughness. Section 4.5 discusses a complete strategy of how to simulate the motion of the microrobot and the simulation results.

4.1 The Microrobot Speed

This microrobot is actuated by thermal bimorph actuators. There are many factors to influence robot speed including temperature of walking surface, robot temperature, roughness of walking surface and actuating frequency of legs. Experimental results show that robot speed starts with a high initial value and then decays exponentially to a stable speed. Approximately the robot speed reaches a stable stage after running for 25 seconds.

In previous research [10], they hypothesize that the motion of the microrobot is governed by the following equation.

$$x(t) = at + b(1 - e^{-t/t}) \quad \text{.....(4.1)}$$

This model represents robot position as a combination of a linear term, $at+b$, and an exponentially decaying term, $-be^{-t/t}$. By differentiating Equation 4.1 with respect to time, the robot speed can be represented with the following equation.

$$V(t) = a + \frac{b}{t}e^{-t/t} \quad \text{.....(4.2)}$$

From Equation 4.2, the initial speed $V(0)$ is $a+\frac{b}{t}$, the speed of steady state $V(\infty)$ is a, and t is the time constant which describes the speed decay. The best fit of Equation 4.1 to experimental data is determined by minimum square fit. Figures 4.1 ~ 4.8 show the experimental data and curve fitting results of position versus time and also speed plots. The speed plots are based on Equation 4.2 using constants a, b, and t generated from best-fit results of Equation 4.1.

(a)

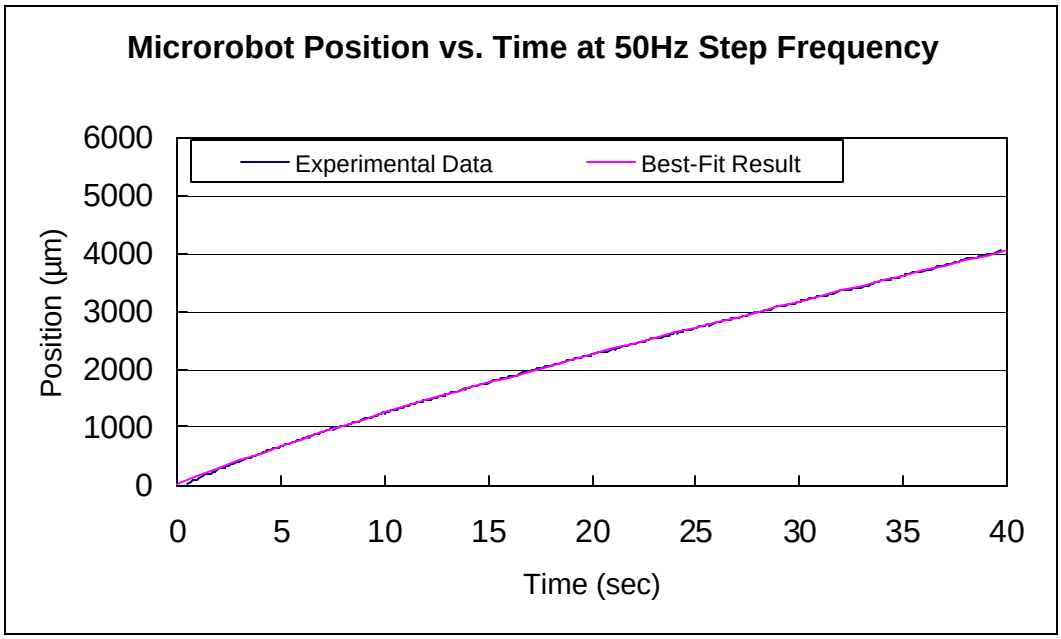

(b)

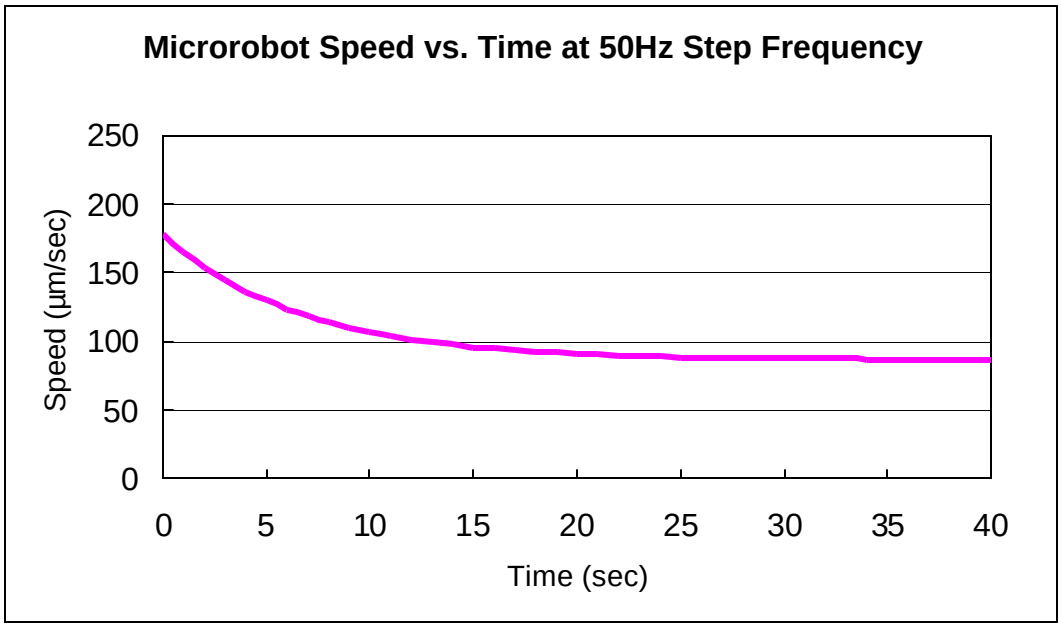

Figure 4.1: (a) Experimental data and curve fitting results of position versus time (b) speed versus time. $V(0)$ and $V(\infty)$ are 178.32 μm/sec and 86.59 μm/sec respectively.

(a)

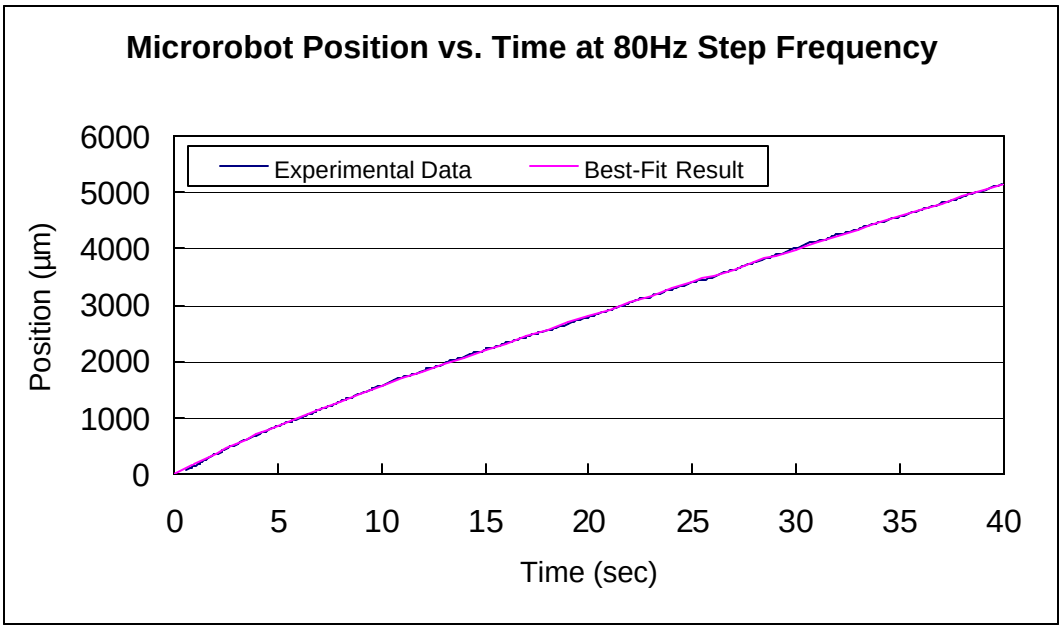

(b)

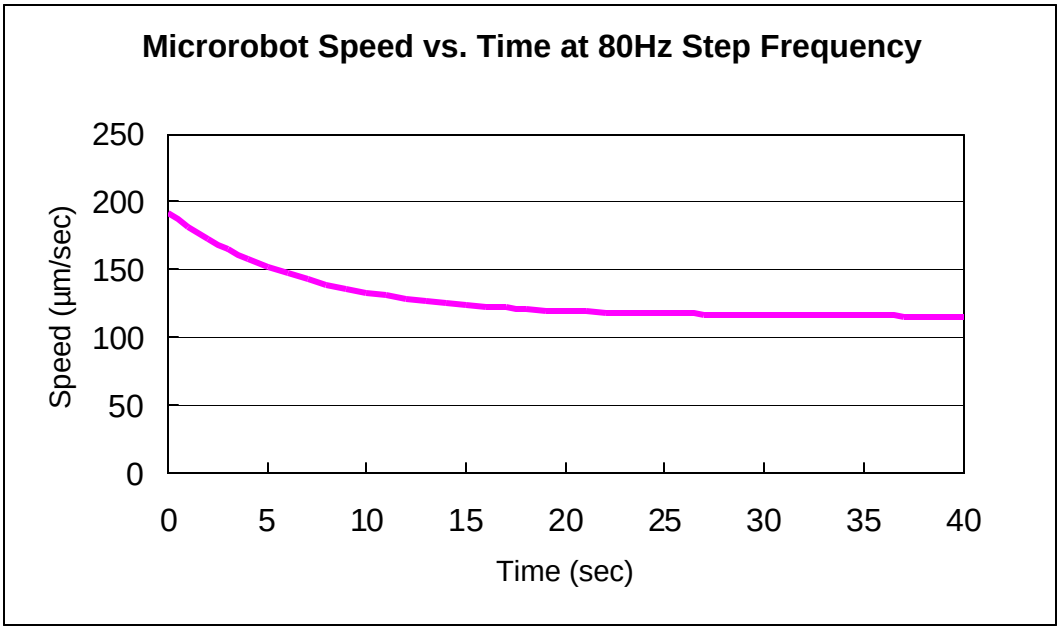

Figure 4.2: (a) Experimental data and curve fitting results of position versus time (b) speed versus time. $V(0)$ and $V(\infty)$ are 192.61 μm/sec and 115.77 μm/sec respectively.

(a)

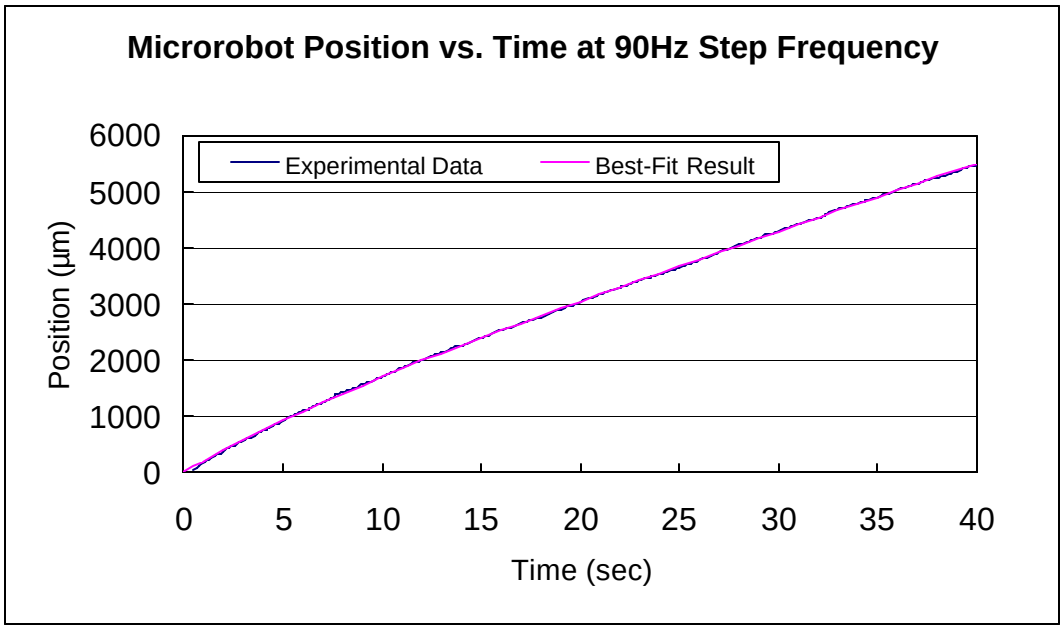

(b)

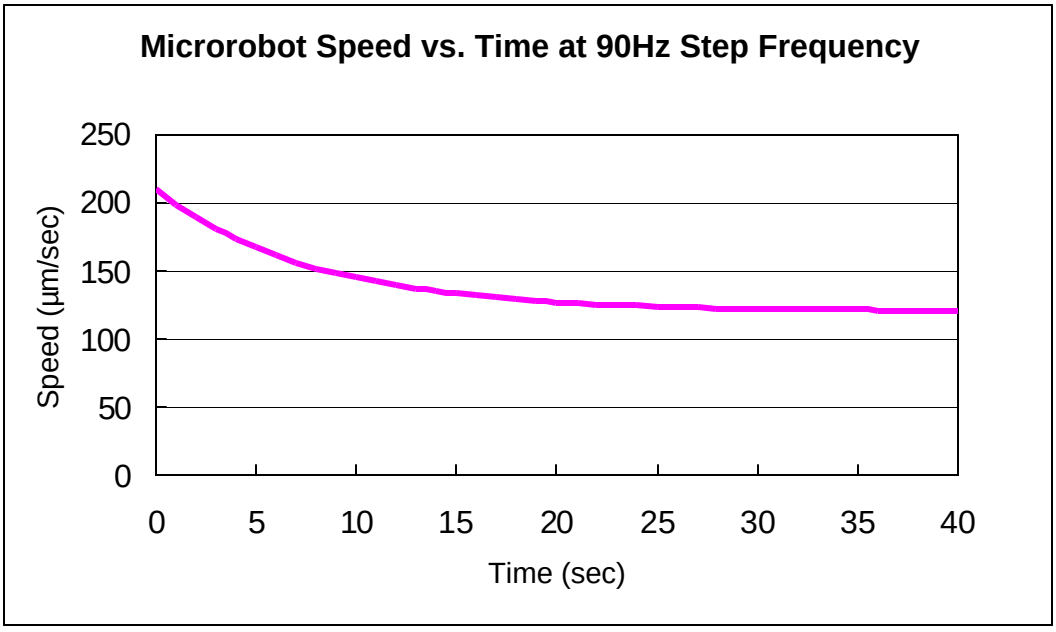

Figure 4.3: (a) Experimental data and curve fitting results of position versus time (b) speed versus time. $V(0)$ and $V(\infty)$ are 209.40 μm/sec and 120.40 μm/sec respectively.

(a)

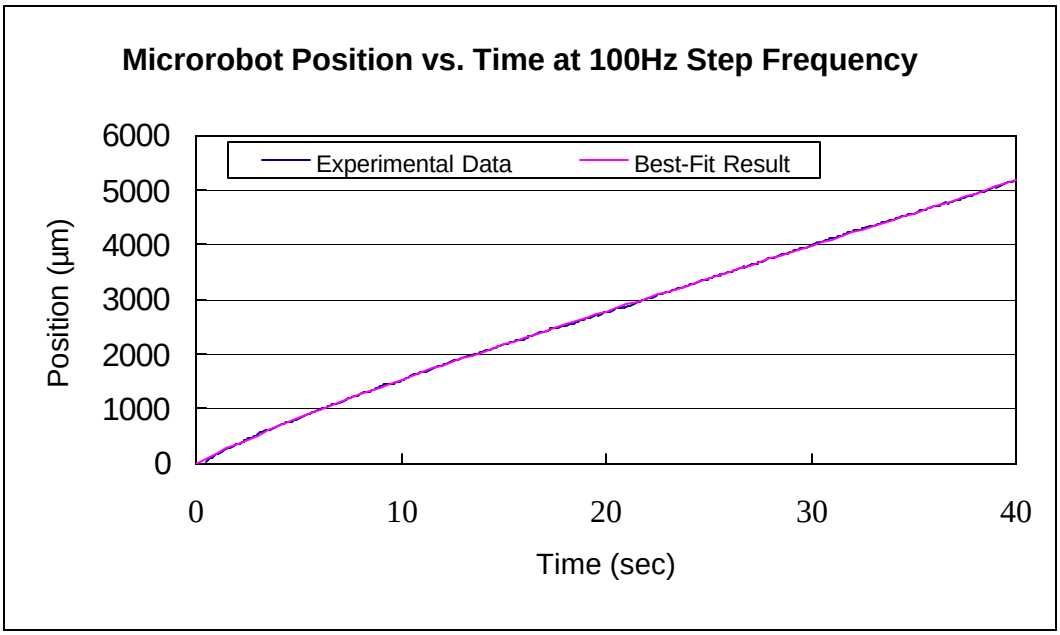

(b)

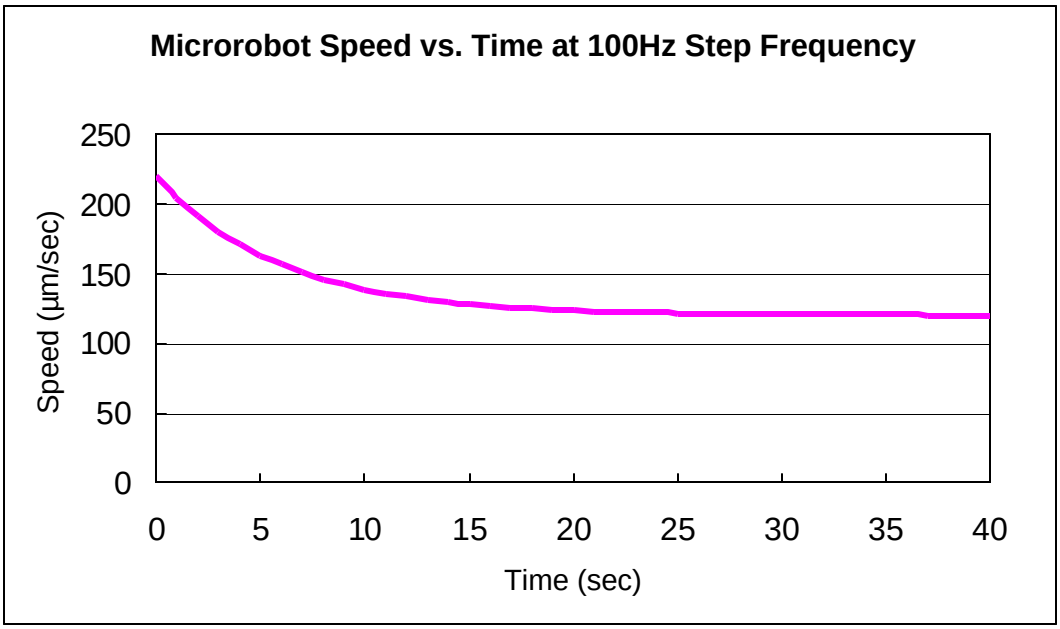

Figure 4.4: (a) Experimental data and curve fitting results of position versus time (b) speed versus time. $V(0)$ and $V(\infty)$ are 224.35 μm/sec and 124.50 μm/sec respectively.

(a)

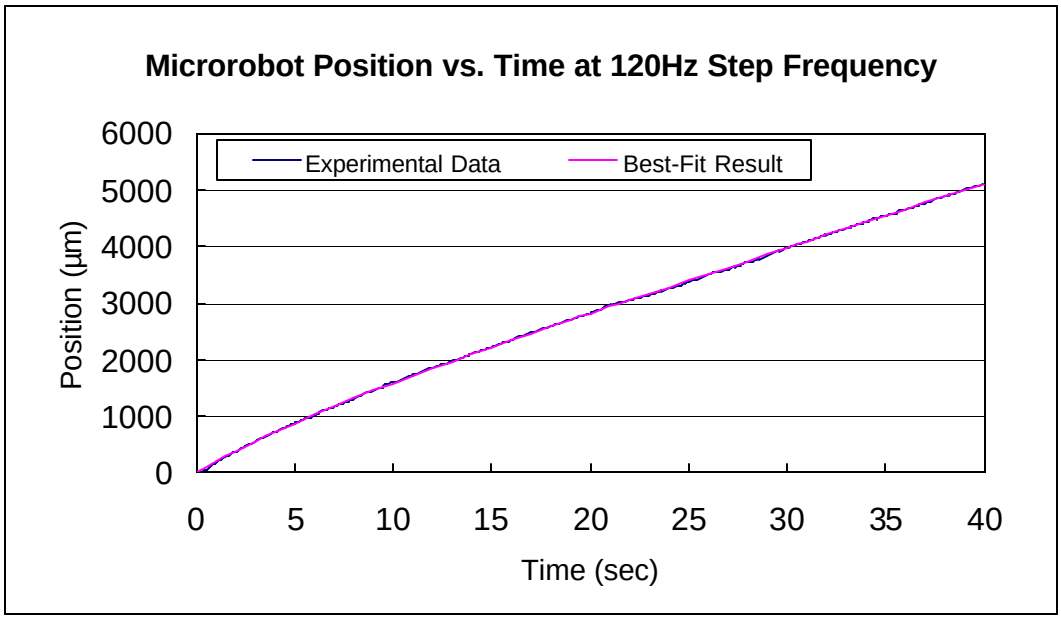

(b)

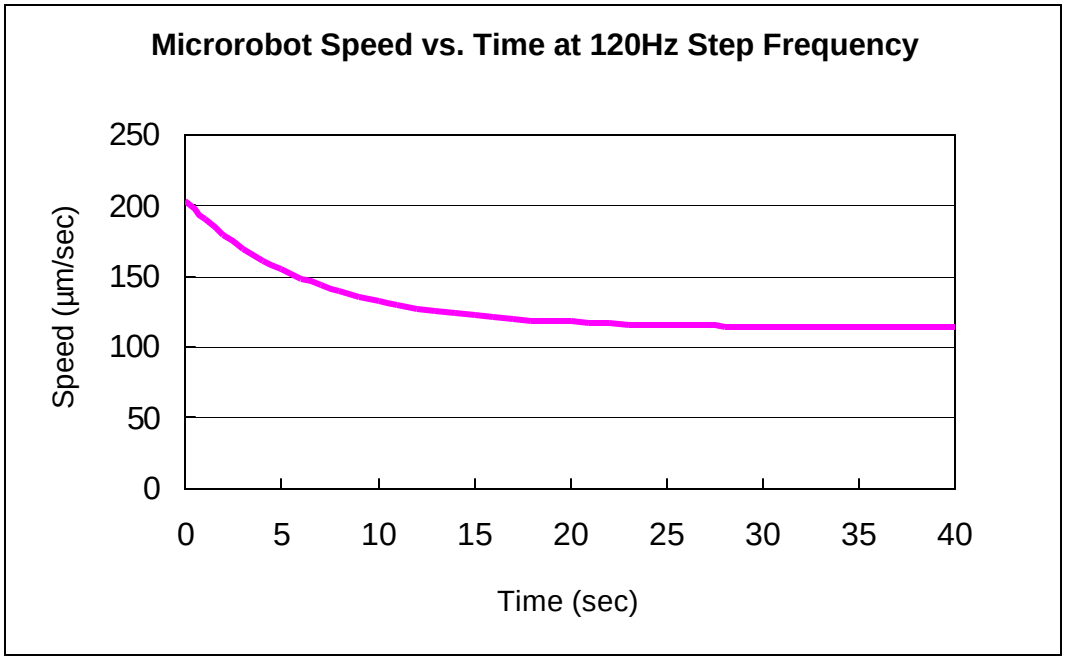

Figure 4.5: (a) Experimental data and curve fitting results of position versus time (b) speed versus time. $V(0)$ and $V(\infty)$ are 203.33 μm/sec and 113.53 μm/sec respectively.

(a)

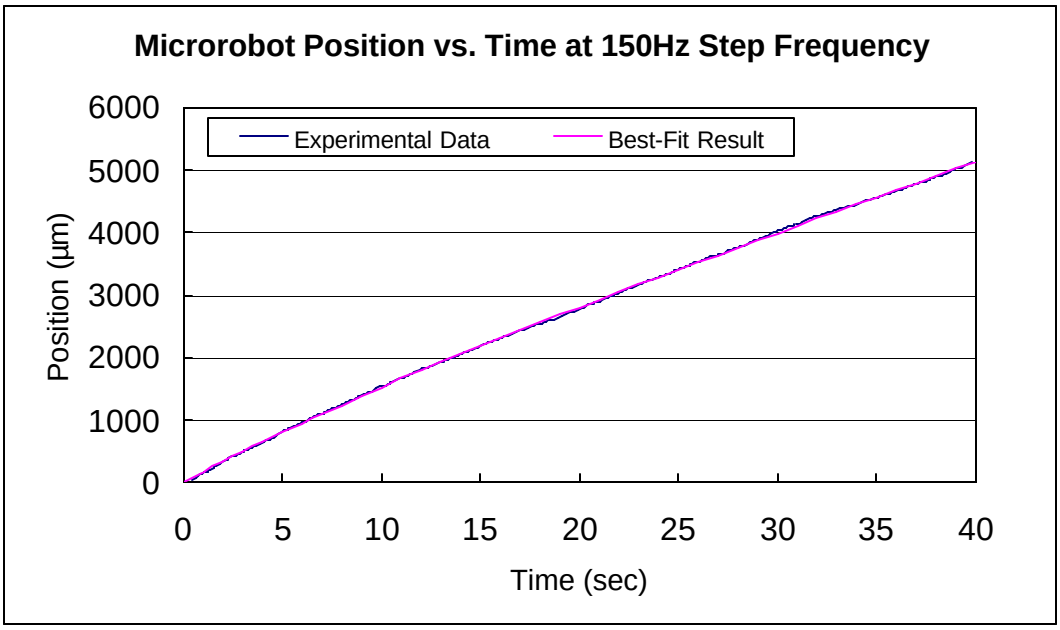

(b)

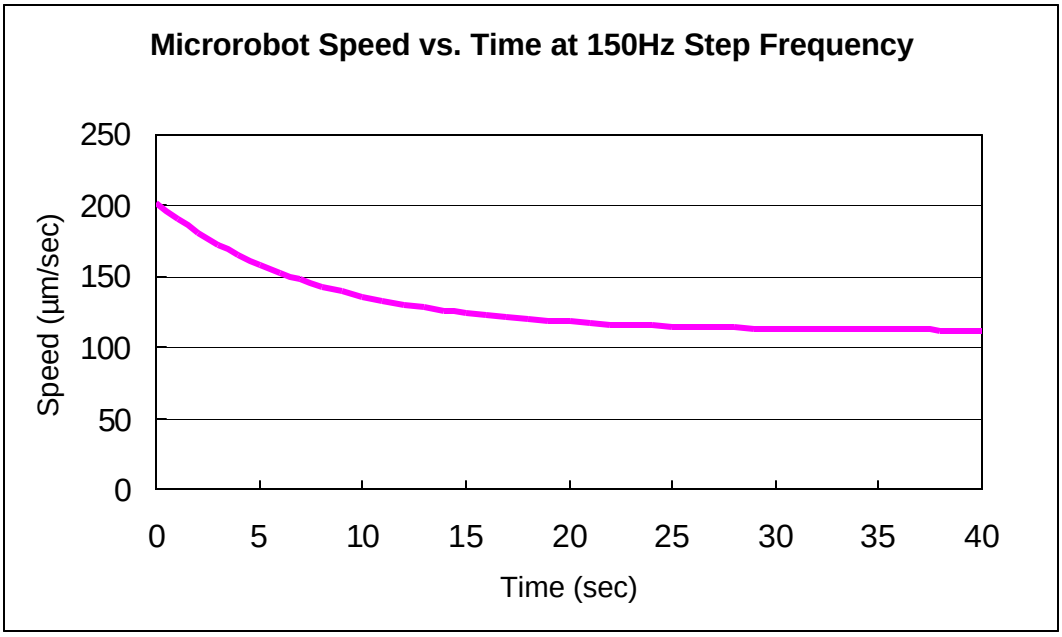

Figure 4.6: (a) Experimental data and curve fitting results of position versus time (b) speed versus time. $V(0)$ and $V(\infty)$ are 201.90 μm/sec and 111.58 μm/sec respectively.

(a)

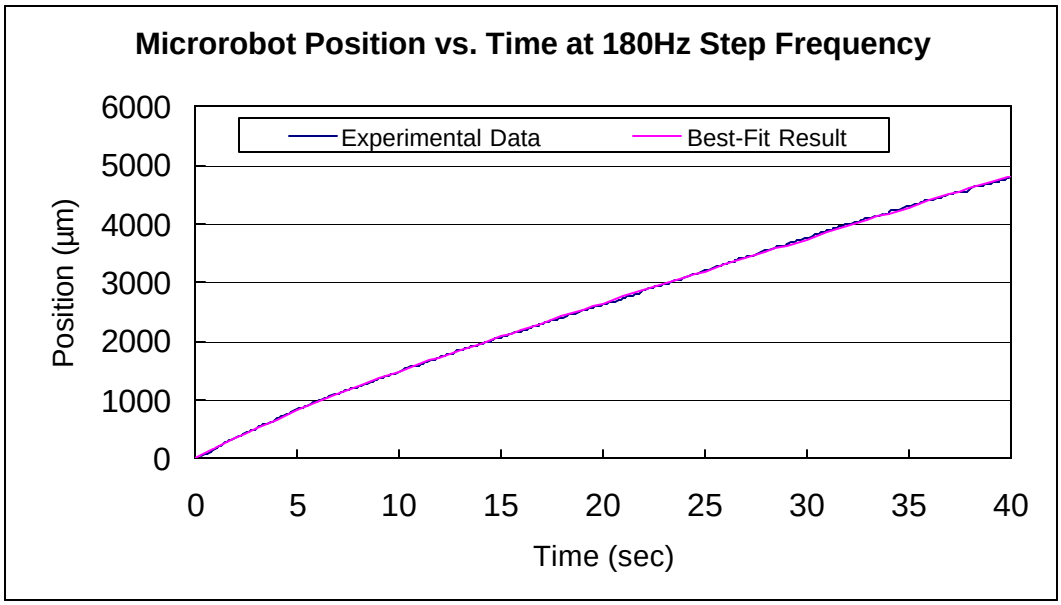

(b)

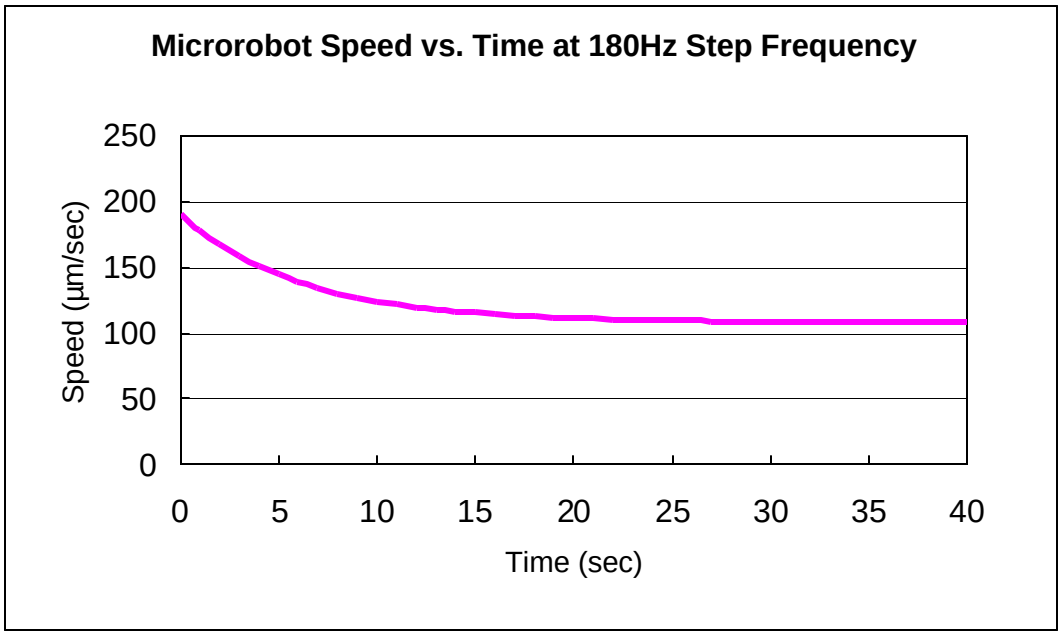

Figure 4.7: (a) Experimental data and curve fitting results of position versus time (b) speed versus time. $V(0)$ and $V(\infty)$ are 190.05 μm/sec and 107.95 μm/sec respectively.

(a)

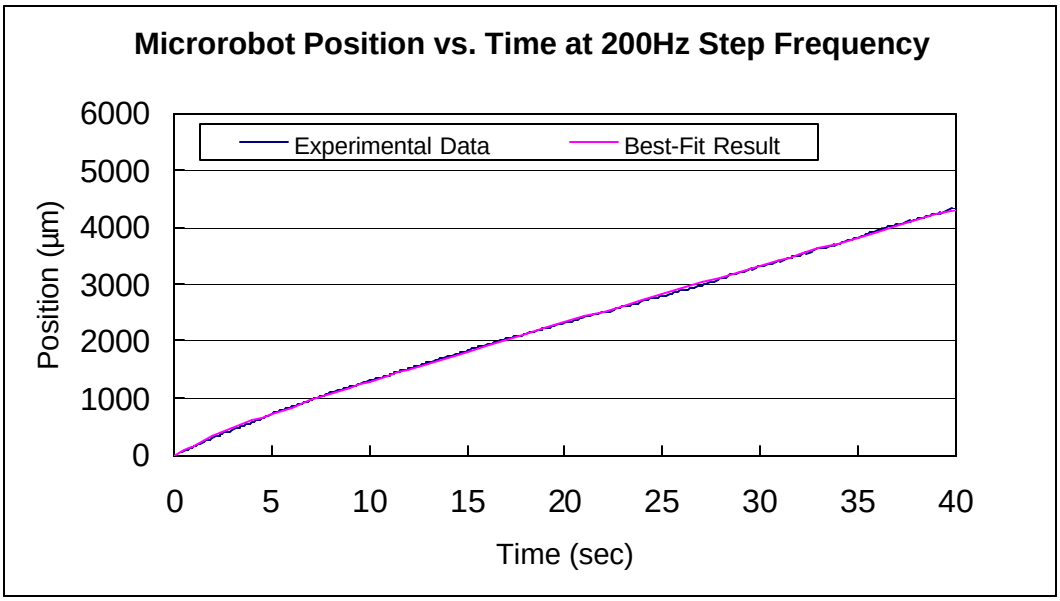

(b)

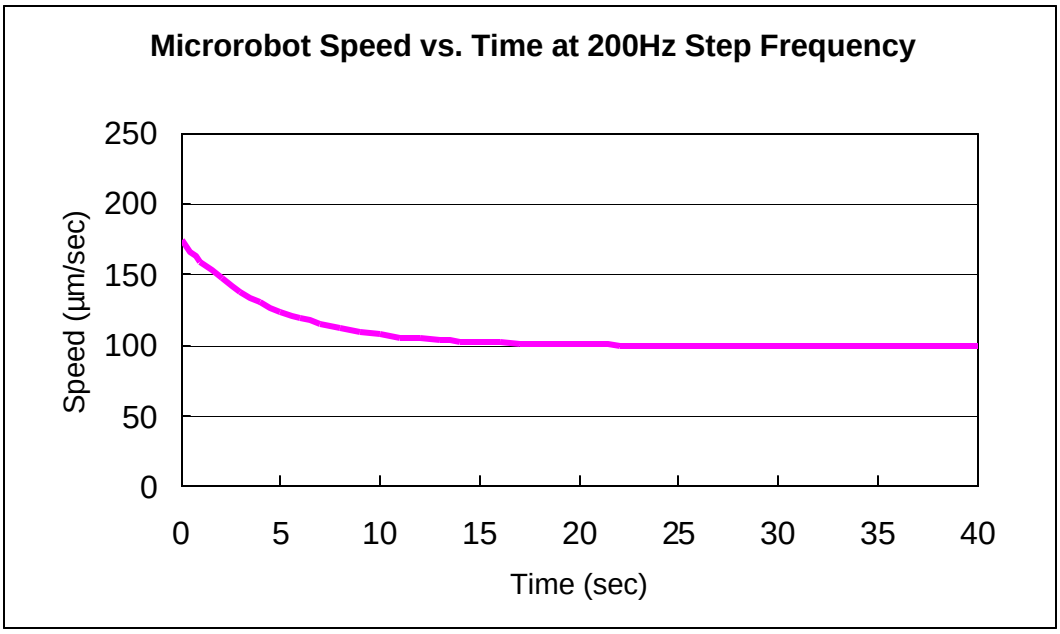

Figure 4.8: (a) Experimental data and curve fitting results of position versus time (b) speed versus time. $V(0)$ and $V(\infty)$ are 174.04 μm/sec and 99.71 μm/sec respectively.

When comparing all the speed plots of different step frequencies like Figure 4.9, it can be seen that although the robot speed is influenced by several factors, these speed plots have similar decaying tendency. In the speed model, the t constant describes speed decay. From Figure 4.10, it is also apparent that all the t constants of these step frequencies have similar values. From investigating the four-phase motion, the heat dissipation can have the same or very close duty cycle between different step frequencies at certain conditions and the heat system is the same. This causes close values of time constant.

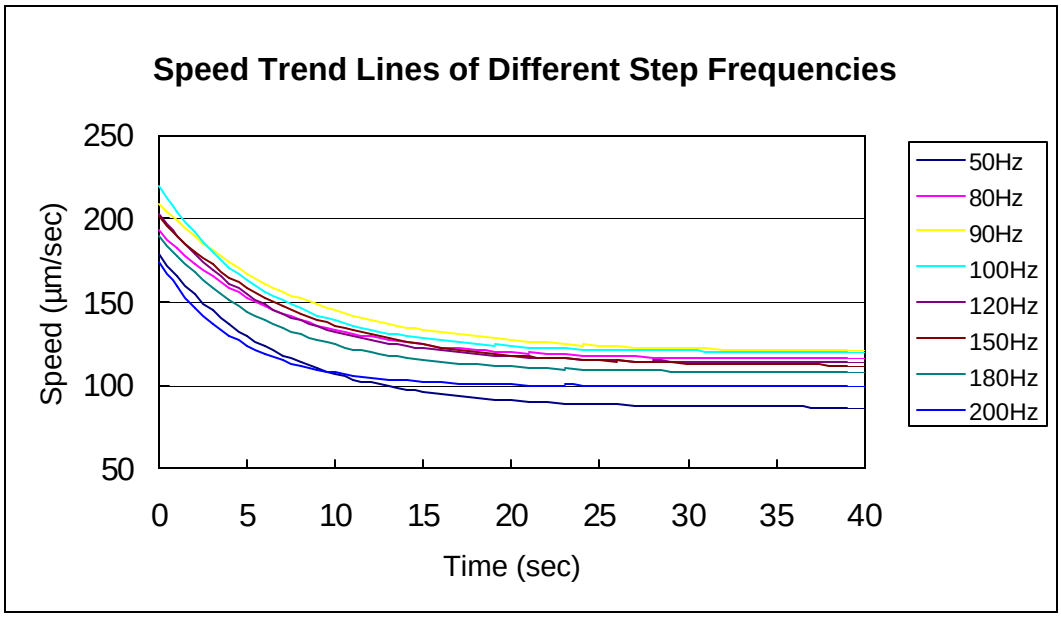

Figure 4.9: Speed plots of different step frequencies. There is a very similar decaying tendency between these plots.

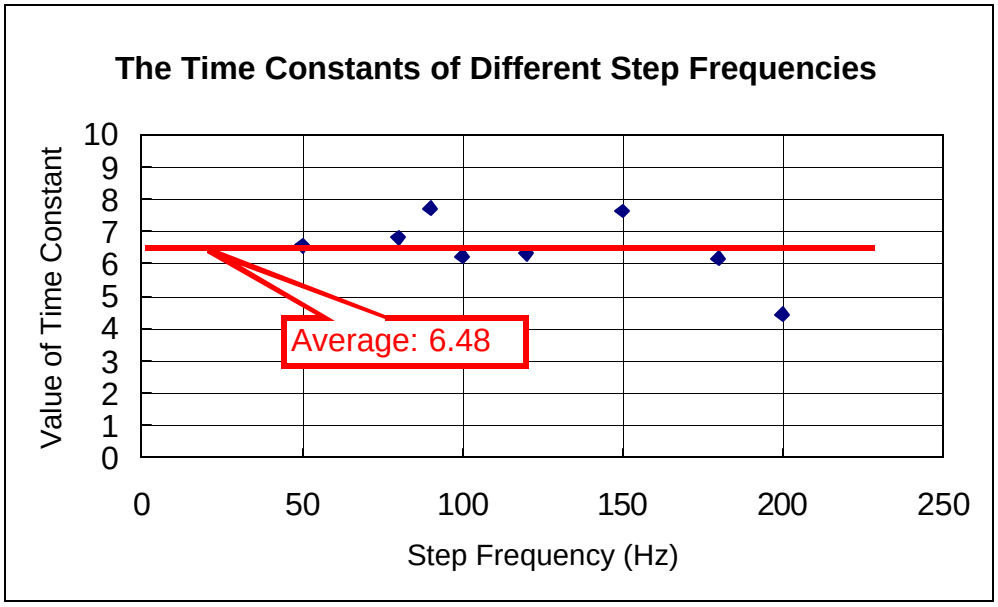

Figure 4.10: The time constants t of different step frequencies. Most of them spread between 6.1 ~ 7.7.

4.2 The Heat Dissipation of Different Step Frequencies

There is an interesting phenomenon shown in section 4.1. Although robot speed can be influenced by several factors, the experimental results of robot speed at different step frequencies have a very similar decaying tendency. We hypothesize that the speed decay is related to temperature increase in the robot chip and the walking surface. The heat dissipation from the microrobot directly relates to the temperature increase.

The applied voltage on the microrobot is 60V. The 64 legs having the same orientation dissipate averagely 1.65W heat when they are actuated. Figure 4.11 shows the heat power dissipated from one cilia array chip in each phase of the four-phase motion. Because the legs in every motion pixel are

actuated in the same way, Figure 4.11 only uses one motion pixel to express them.

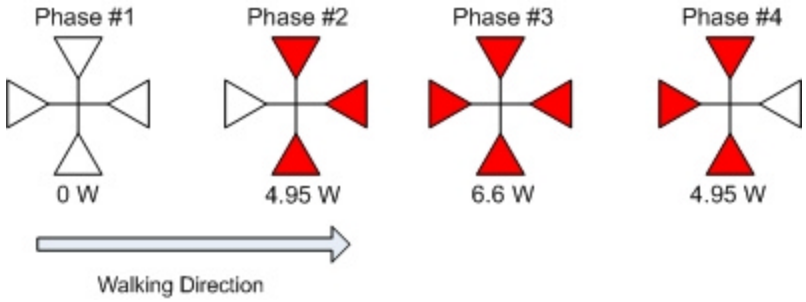

Figure 4.11: The heat power dissipated from one cilia array chip in each phase of the four-phase motion.

Figure 4.12 is the comparison of energy dissipation between 100Hz and 200Hz in 0.04 second. It shows that the same amount of energy is dissipated in 0.04 second. This situation will be the same for longer operation time. The same amount of energy means the same temperature increase. Figure 4.13 shows the temperature measurements of 100Hz and 200Hz step frequency on the microrobot chip and the walking surface for 40 seconds. Because of the same temperature increase, the plots of 100Hz and 200Hz overlap.

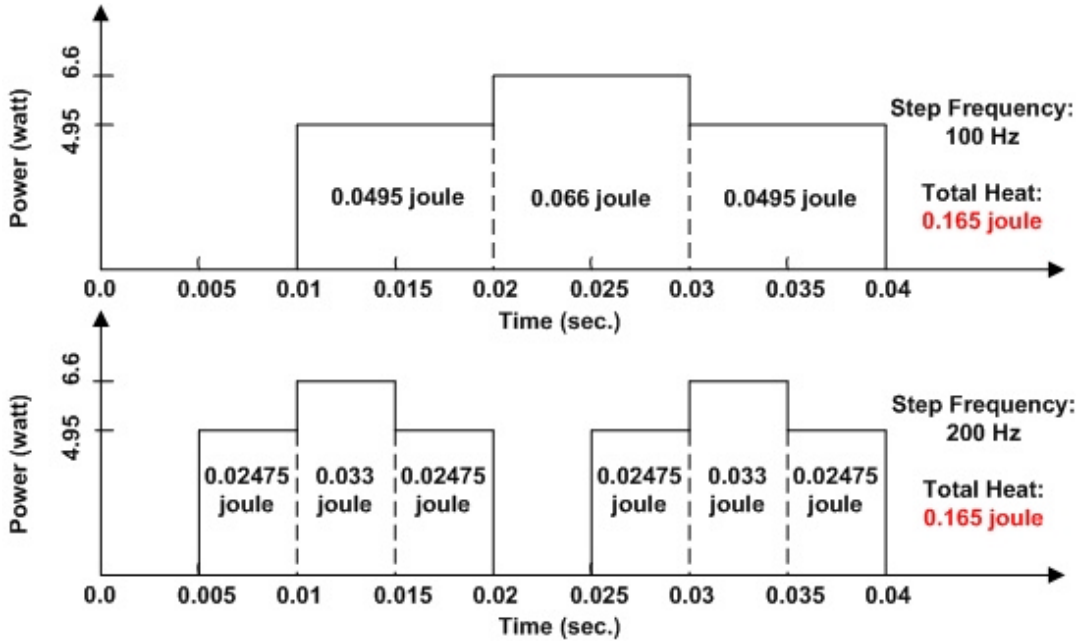

Figure 4.12: The energy dissipation of 100Hz and 200Hz step frequency. The same amount of energy is dissipated in 0.04 second.

(a)

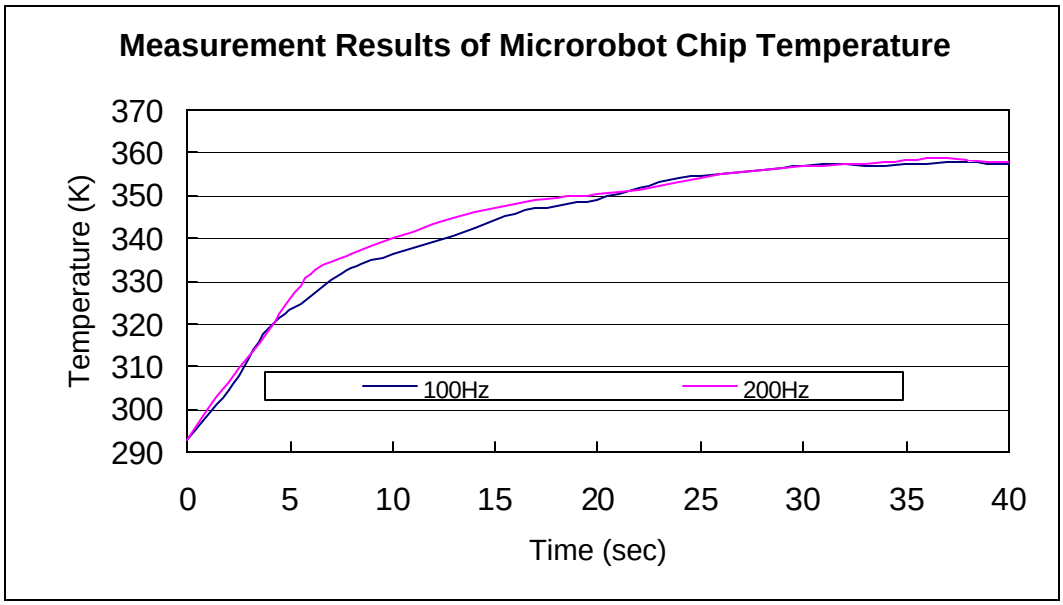

(b)

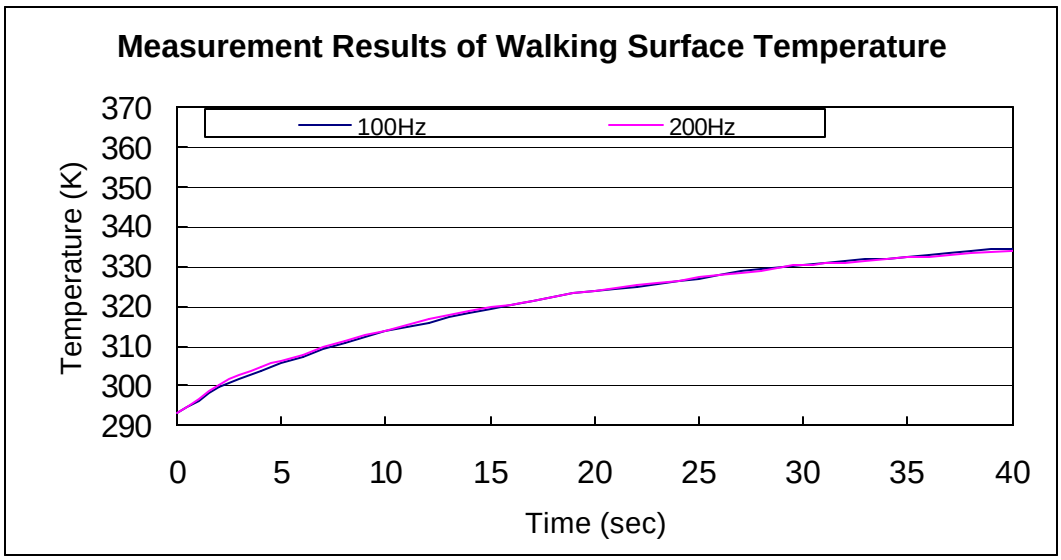

Figure 4.13: Temperature measurements of 100Hz and 200Hz step frequency on (a) microrobot chip (b) walking surface

In other words, the energy dissipation is the same but is spread into a different number of divisions depending on the step frequencies. This explains the phenomenon that the speed plots at different frequencies share very similar speed decay.

However, this is not always true in every kind of situations. If the operation time is not a multiple of $4*\frac{1}{step\_frequency}$, the last cycles of four-phase motion will be cut off before completion. For example, if the operation time is 0.04 second and the step frequency is 25Hz, there is no heat dissipation in 0.04 second. Figure 4.14 shows the calculation results of energy dissipation for different step frequencies in one second. When the step frequency is above 50Hz, the heat dissipation at different frequencies is already very similar. In general, if the total operation time is greater or equal to $n*\frac{4}{step\_frequency}$, then the relative deviation from the average heat dissipation is less than a factor $\frac{1}{n}$.

Therefore, to make heat dissipation independent of frequency, either operation time should be long enough or operation frequencies should be high enough. Then the influence of changing operation frequency to heat dissipation, which relates to speed decay, can be ignored.

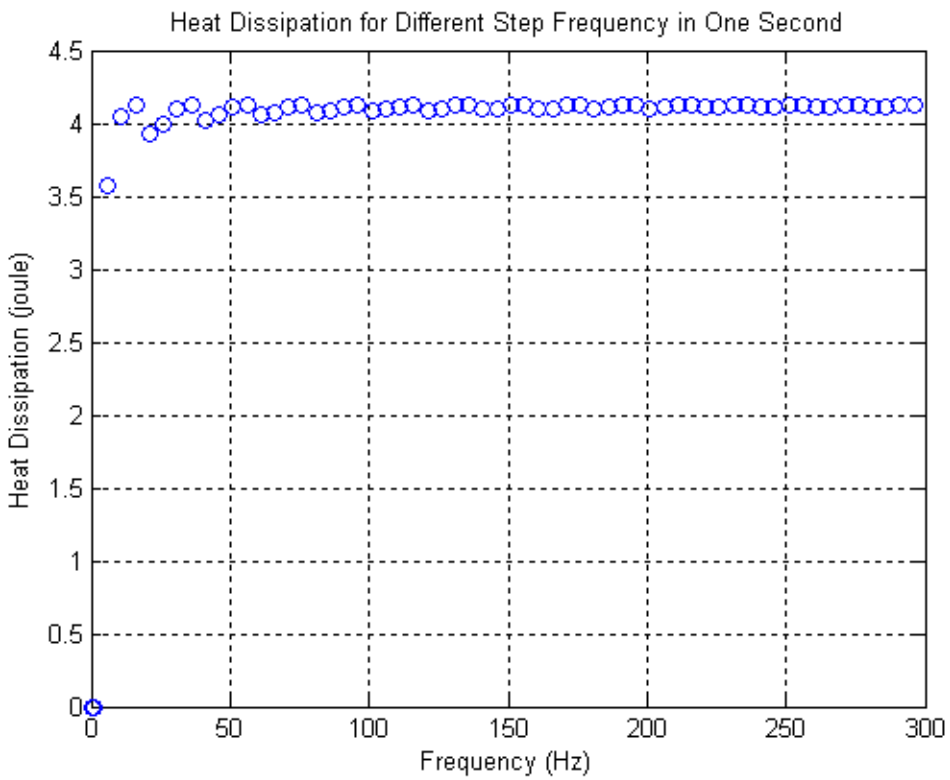

Figure 4.14: Calculation results of heat dissipation for different step frequencies in one second. Above 50Hz, the value is almost a constant.

4.3 The Correlation Between Temperature and Speed

From the discussion in Section 4.2, it can be seen that robot speed closely relates to the temperature of robot chip and walking surface. They are the dominating boundary conditions for the heat transfer between robot chip and walking surface. If the assumption that robot speed at a certain moment mainly depends on the temperature of robot chip and walking surface at that moment is correct under a premise that surface roughness and robot weight are the same, using temperature as a feedback is a feasible and good way for robot control.

A simple experiment was performed to verify the assumption. A thermocouple was attached underneath the walking surface and just beneath one of the two cilia array chips. The robot began to run for 20 seconds, stopped running for 10 seconds and then resumed running for 10 seconds. The temperature displayed on the thermocouple was recorded simultaneously. Figure 4.15 shows the comparison of temperature and robot speed. The temperature at 30^{th} second was close to that of 8^{th} second. The speed at 30^{th} second was also close to that of 8^{th} second. In both cases, temperature and speed show virtually identical profiles. This is a good indication that the assumption was correct. There are an infinite number of ways to achieve a certain temperature depending on different ways of operation. This important property of the microrobot increases much of the flexibility in robot operation.

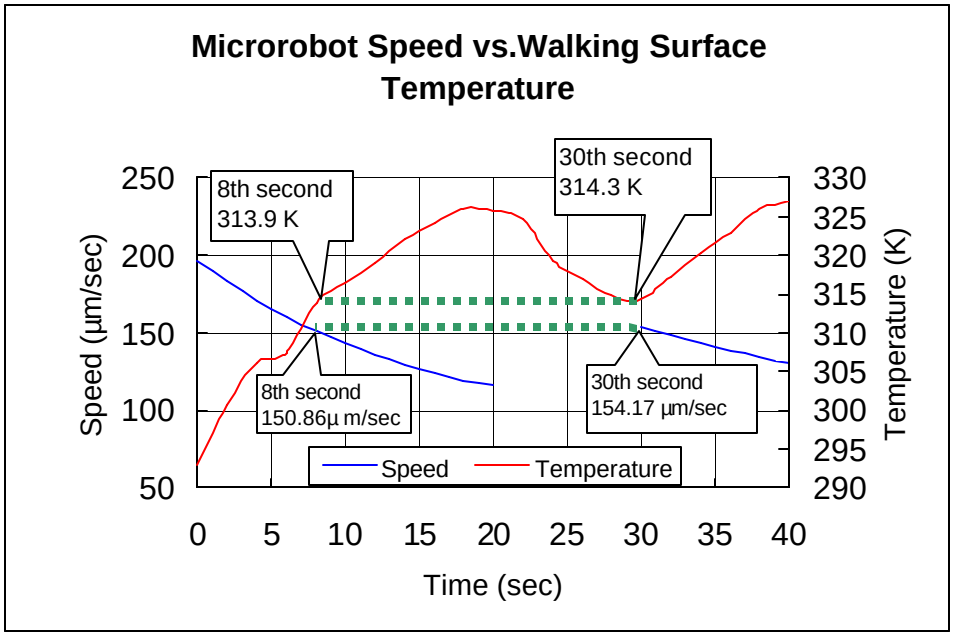

Figure 4.15: The comparison of microrobot speed and walking surface temperature. The microrobot ran for 20 seconds, stopped running for 10 seconds and then resumed running for 10 seconds.

4.4 The Influence of Surface Roughness

The importance of temperature is shown in previous sections. The influence of surface roughness is the other consideration to microrobot motion. At the present setup, the robot walks on the unpolished side of a 3-inch silicon wafer. Two experiments were performed. The first one was at 100Hz step frequency and the second one was at 1000Hz step fequency. The web links below connect to the videos taken in these two experiments. The frame rate of the videos is 30 frames/second.

Experiment Video at 100Hz Step Frequency on 3-Inch Silicon Wafer:

www.ee.washington.edu/research/mems/videos/100hz_on_3inch_wafer.mpg

Experiment Video at 1000Hz Step Frequency on 3-Inch Silicon Wafer:
www.ee.washington.edu/research/mems/videos/1000hz_on_3inch_wafer.mpg

In the experiments, the robot has very smooth motion at 100Hz step frequency but when the frequency was up to 1000Hz, the walking surface seems to become "sticky". The robot speed had obvious fluctuations. Because the robot has smaller step size at higher frequency, it is assumed that the walking surface becomes relatively rough for smaller step size. The relatively uneven surface hinders the robot from moving forward.

Because the frame rate of motion tracking software doesn't match robot's motion cycle, this will cause a variation at speed calculation in experimental results. During every cycle of motion, the robot moves two steps forward. For 100Hz, averagely the robot moves about 6 steps between every frame but it happens that software can also catch 5 or 7 steps between every frame if it records the position of the robot at different timing in a cycle of motion. This causes about ±16.67% variation on the speed. For 1000Hz, averagely the robot moves about 60 steps between every frame but 59 or 61 steps are also possible depending on the timing. This causes about ±1.67% variation on the speed. Figures 4.16 and 4.17 show the speed calculations from experimental results, the best-fit curves and the variation ranges of speed. The speed calculations are the average speed between every frame. It can be seen in Figure 4.16 and 4.17 that the robot speed at 1000Hz step frequency has a lot more speed fluctuations outside the variation range.

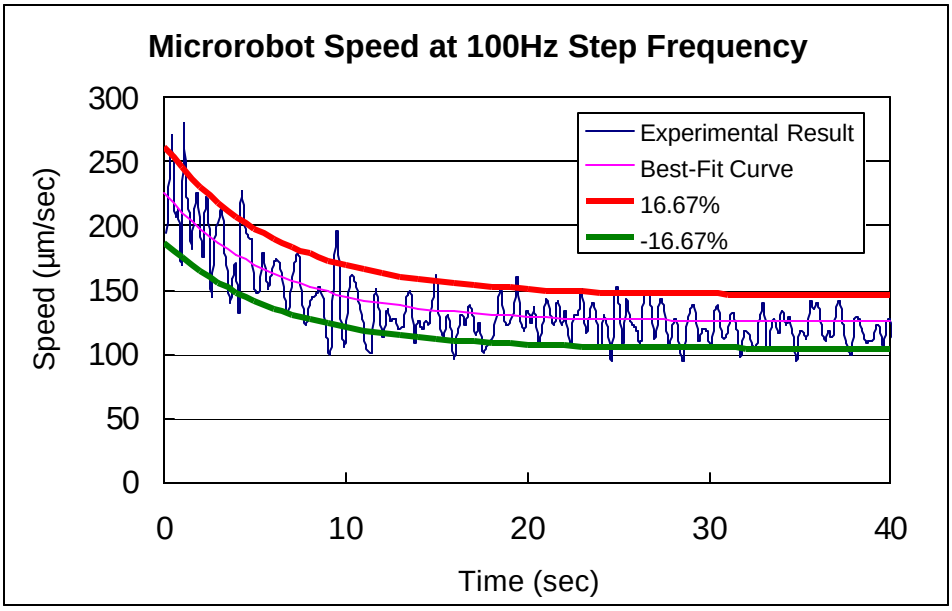

Figure 4.16: Experimental result, best-fit curve and variation range. It shows that the speed is within variation range. This means that the influence of surface roughness is not severe.

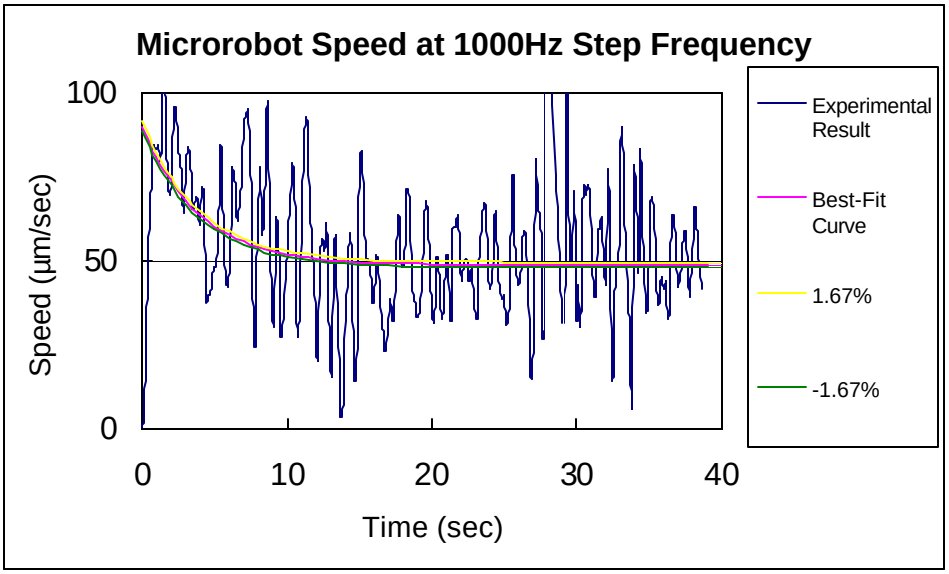

Figure 4.17: Experimental result, best-fit curve and variation range. It shows that the speed is well outside the variation range. This means that the influence of surface roughness is very severe.

To do further verification for the assumption, two more experiments were performed. In the experiments, the walking surface was exchanged to two pieces of glass with the same size and thickness. Glass A has a polished surface but glass B was dipped into HF solution to get a rougher surface. Figure 4.18 shows the comparison of these two glasses. The microrobot walked on both glass A and B at 10Hz and then 100Hz step frequencies. The web links below connect to the videos taken in these two experiments. The frame rate of the videos is 30 frames/second.

Experiment Video at 10Hz Step Frequency on Glass A:
www.ee.washington.edu/research/mems/videos/10hz_on_smooth_glass.mpg

Experiment Video at 100Hz Step Frequency on Glass A:
www.ee.washington.edu/research/mems/videos/100hz_on_smooth_glass.mpg

Experiment Video at 10Hz Step Frequency on Glass B:
www.ee.washington.edu/research/mems/videos/10hz_on_rough_glass.mpg

Experiment Video at 100Hz Step Frequency on Glass B:
www.ee.washington.edu/research/mems/videos/100hz_on_rough_glass.mpg

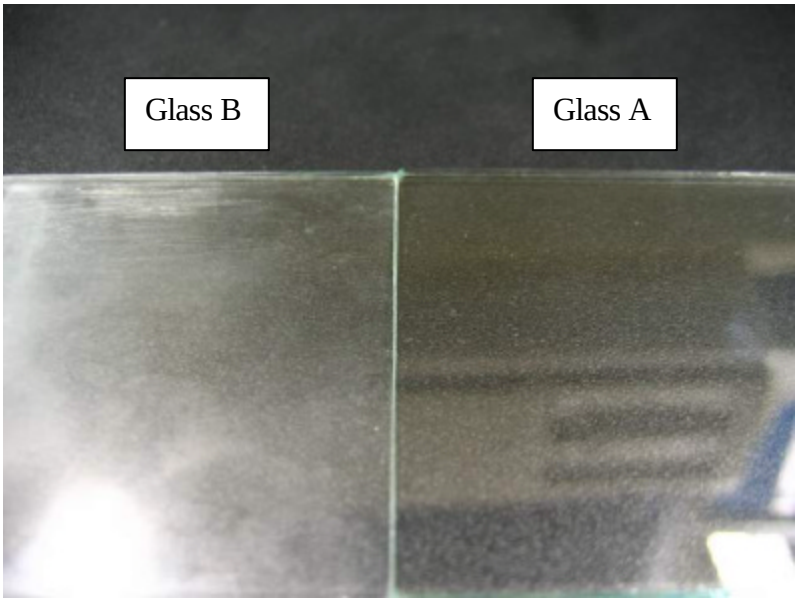

Figure 4.18: The comparison of glass A and B. Glass A has a polished surface. Glass B was dipped into HF solution to get a rougher surface.

At 10Hz step frequency, the robot' s motion has no big difference on both glass A and B. However at 100Hz step frequency, the robot has smooth motion on glass A but can't even move forward on glass B. Figure 4.19 and Figure 4.20 show the surface roughness measurement of glass A and B. The height between highest and lowest position is about 0.3μm on glass A and about 6.5μm on glass B. Basing on the robot speed, the effective step size at 100Hz step frequency is 1.25μm. Because step size is proportional to lift-up height, at 1.25μm step size the lift-height is about 7μm. At 10Hz step frequency, the lift-up height is about 15μm. The robot' s legs have higher chance to get tripped on rough surface at 100Hz step frequency.

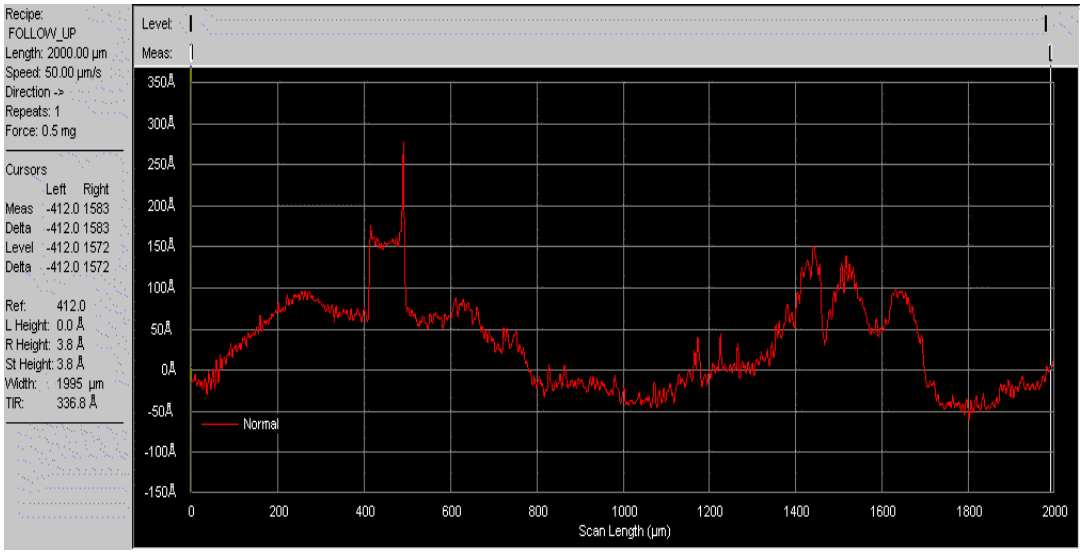

Figure 4.19: Surface roughness measurement of glass A in Figure 4.18 taken by Cheng-Chun Lee at the Washington Technology Center. The heigth between highest and lowest position is about 0.3µm.

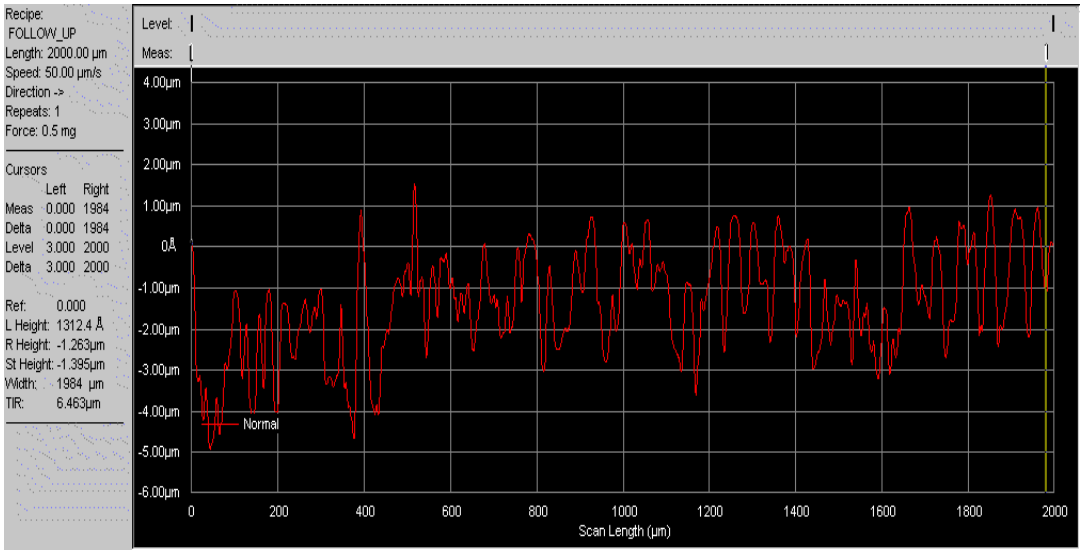

Figure 4.20: Surface roughness measurement of glass B in Figure 4.18 taken by Cheng-Chun Lee at the Washington Technology Center. The length between highest and lowest position is about 6.5µm.

4.5 Simulations

From observation and experiments, many characteristics of this microrobot have been found, and these characteristics are useful for robot control. It is the heating-up and cooling-down in the micro cilium actuators that make the microrobot move. The heat transfer inside the small 120μm gap between robot chip and walking surface dominates the performance of the microrobot. To understand the heat transfer inside the gap is the best way to fully understand the microrobot. However, it is very difficult to measure it from an experiment. Computer simulation is specifically useful for this kind of situation. ANSYS is a very sophisticated simulation software. It has broad academic and industrial usage. Structural, thermal and CFD (Computational Fluid Dynamics) simulations were performed in this project. The list below is the outline of Section 4.5:

4.5.1 describes the general considerations in the simulations.

4.5.2 describes the experimental idea about how to simulate the temperature of the robot chip and the walking surface inside the gap.

4.5.3 describes the simulation of the micro cilium.

4.5.4 compares the lift capacity of the micro cilium with that of the micro cilium model.

4.5.5 describes the FSI simulation, which is a CFD and structure coupled simulation.

4.5.1 Simulation Considerations

Before the simulation, it is important to understand what kind of problem it is. Figure 4.21 is a schematic of the microrobot. Heat is dissipated from the

robot legs. The top and bottom air layers are the media, which transfer heat dissipated from every micro cilium to the robot chip and the walking surface. Then the heat dissipates from the robot chip and the walking surface into the surroundings. What makes the simulation difficult is that the robot legs are always moving and the air layers are always changing. As the robot runs for longer time, the temperature of the robot chips and the walking surface becomes higher and the thickness of the gap becomes smaller.

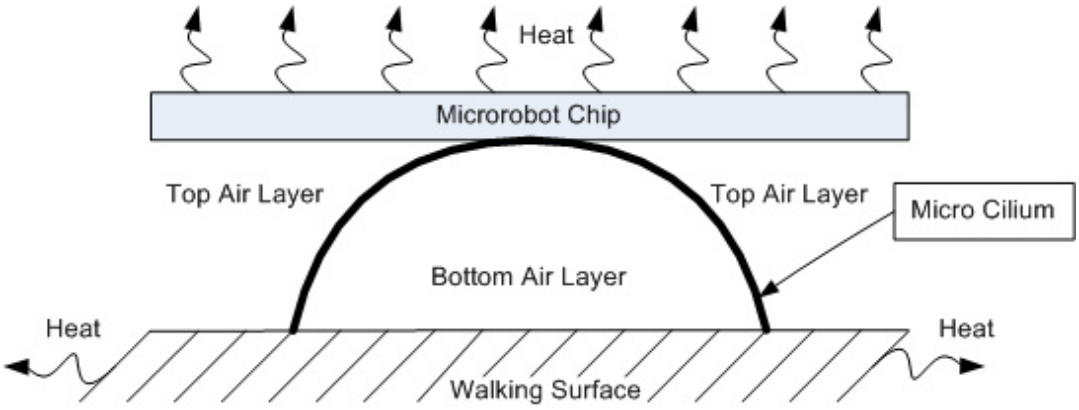

Figure 4.21: A schematic of the microrobot. The top and bottom air layers are the main media, which transfer heat dissipated from every micro cilium to the robot chip and the walking surface.

The strategy is to use a CFD simulation for air layers. The boundary conditions in the CFD model are the temperature of the microrobot chip and the walking surface inside the gap. A thermal model can simulate these boundary conditions. The following sections describe the details of these simulations and the complete simulation procedures are in the Appendix.

4.5.2 Macroscopic Simulation

Figure 4.22 shows the experimental setup of this project. The microrobot walks on top of a 3-inch silicon wafer and two piles of pyrex glass lift up the wafer by 5mm. Because the surface temperature of the robot chip and the walking surface inside the gap cannot be measured, this simulation is to generate the temperature for the CFD simulation as boundary conditions. To get the temperature, it is necessary to consider the heat generation from the robot as well as the heat dissipation from the whole system including the robot chip, the walking surface and the surface of the pyrex glass. Technically it is difficult to simulate the macroscopic geometry and also include the detailed microscopic structure. An idea inspired from a heat transfer phenomenon, Thermal Contact Resistance, was tried here. The contact resistance phenomenon is shown in Figure 4.23. In composite systems, the temperature is discontinuous across the interface between two materials. This temperature change is due to what is known as the thermal contact resistance, $R''_{t,c}$. It is defined in Equation 4.3 [11].

$$R''_{t,c} = \frac{T_A - T_B}{q''_x} \quad \text{.....(4.3)}$$

q''_x: Heat flux

T_A and T_B: The temperature of material A and B

Because of surface roughness, two materials cannot perfectly contact and there are many small holes in the interface. In many cases, air fills them. This situation is very similar to the gap between the robot chip and the walking surface. The 512 legs connect the robot chip and the walking

surface. The rest of the space is filled with air. In Figure 4.23, the heat transfer characteristic of the interface between two materials is simply expressed as a thermal contact resistance just like a layer of material with a constant thermal property. Therefore it was assumed that the gap between the robot chip and the walking surface could be expressed by simpler geometry.

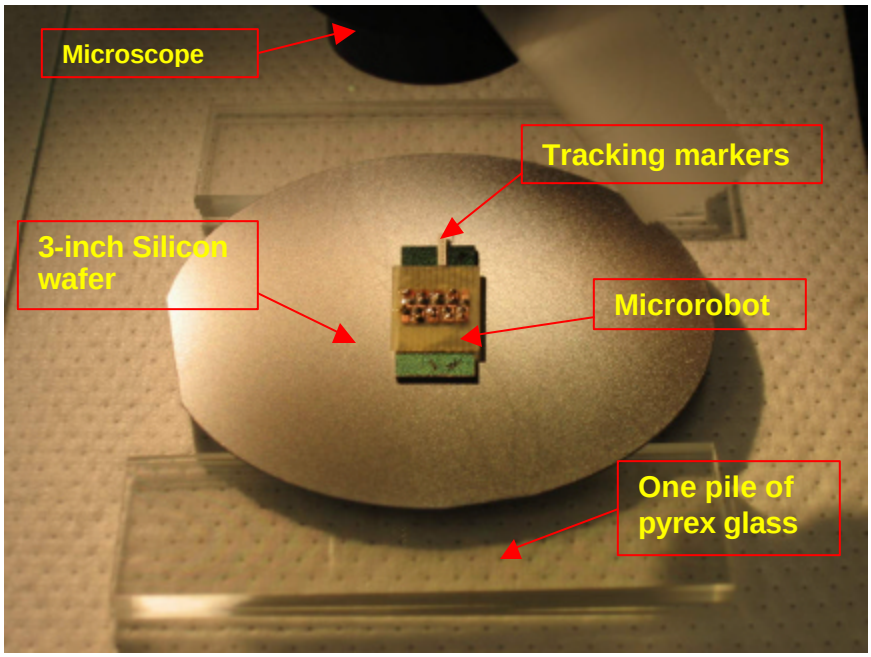

Figure 4.22: Microrobot operational platform. The microrobot walks on a 3-inch silicon wafer. Two piles of pyrex glass lift up the platform. The microscope focuses on the tracking patterns.

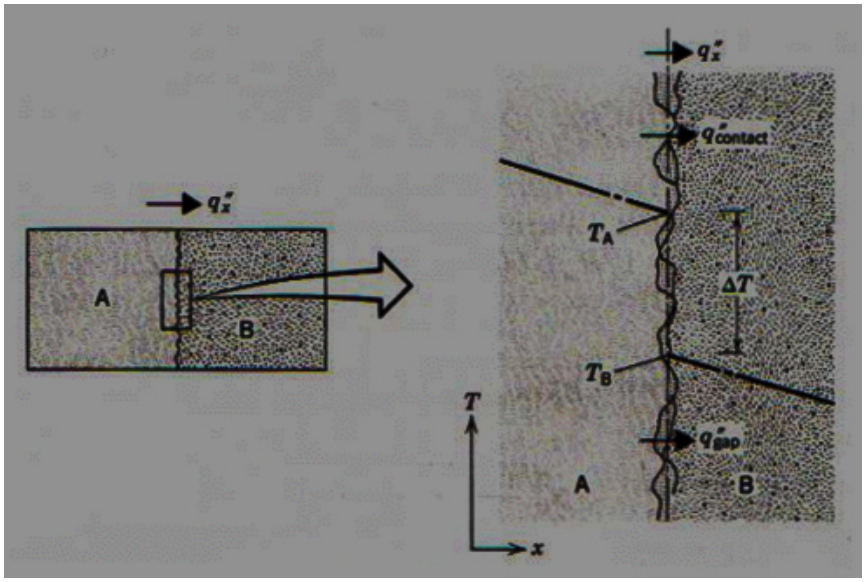

Figure 4.23: Temperature drop due to thermal contact resistance. This plot is scanned from Introduction to Heat Transfer [11].

Based on the setup in Figure 4.22, Figure 4.24 shows the model in this simulation. There are a few assumptions applied on this model. A small gap sandwiched by two flat plates is classified as "open cavity" in the heat transfer problem. For Rayleigh numbers less then a critical value of $Ra_{L,c} = 1708$, buoyancy forces cannot overcome the resistance imposed by viscous forces and there is no advection within the cavity [11]. In this case, the operation temperature is 293K ~ 623K. The Rayleigh number is never over 120.

$$Ra_L = \frac{g \cdot b \cdot \Delta T \cdot L_c^3}{u \cdot a} \quad \text{.....(4.4)}$$

This means there is only heat conduction within the gap. Therefore the gap is simplified into solid layers. Comparing with normal composite systems, the case in this project is more complex because there is heat generation in

the gap, the area of the robot chip and the walking surface is very different, and the structures in the gap are not steady. Hence it was assumed that a single layer of structure is not enough to represent the gap and three layers were used. Here is the second simplification. The robot has the highest speed at 90Hz ~ 100Hz step frequency. Because the microrobot only moves about 5mm in 40 seconds at 90Hz ~ 100Hz, the robot' s movement is ignored in this simulation, i.e., all layers are considered stationary in this simulation.

(a)

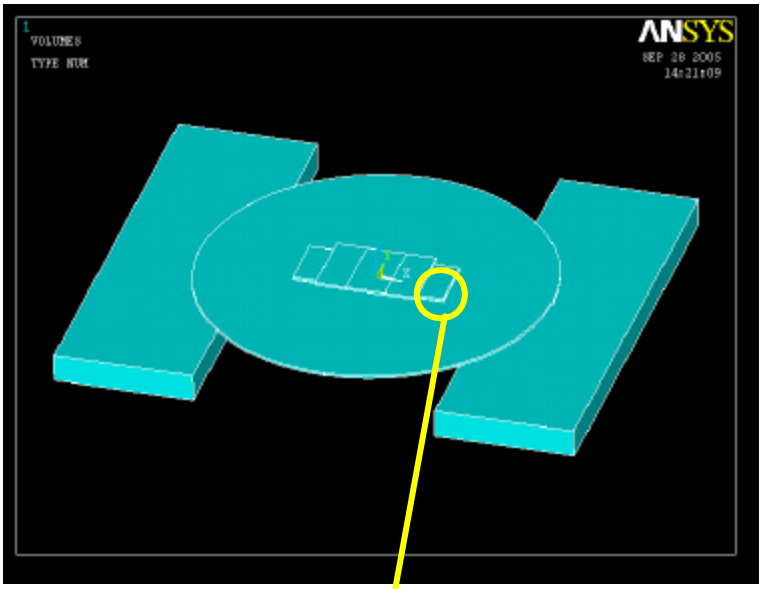

(b)

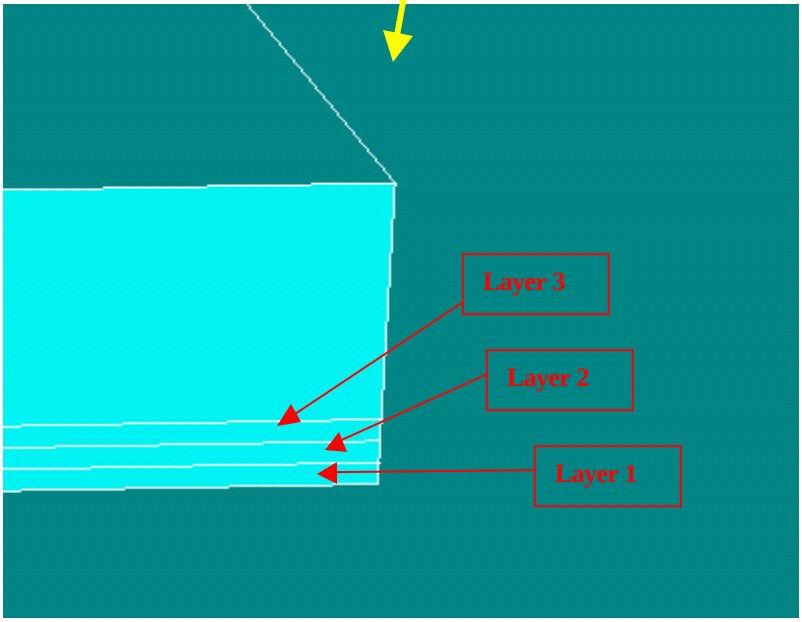

Figure 4.24: The model for macroscopic simulation. (a) full view of the model (b) highlight of the structure between microrobot chip and walking surface.

In heat transfer analysis, the ratio of the thermal conductivity to the heat capacity is an important property termed the thermal diffusivity a, which has units of m^2 / s [11].

$$a = \frac{k}{r \cdot c_p} \quad \text{.....(4.5)}$$

It measures the ability of a material to conduct thermal energy relative to its ability to store thermal energy. Materials of larger a will respond quickly to changes in their thermal environment, while materials of small a will respond more sluggishly, taking longer to reach a new equilibrium condition [11]. Although there are micro cilia inside the gap, they are very thin and the volume is small. Air is volumetric majority inside the gap (about 97.3%). Therefore air's density r and specific heat c_p at 300K are applied in the three layers. There are two ways to transfer heat from the micro cilia into the robot chip and the walking surface. The first is via the top and bottom air layers and the second is via the junctions and contacts of the micro cilia to the robot chip and the walking surface respectively. Therefore the thermal conductivity k of this gap is an unknown. In the simulation, the layer 2 is in charge of heat generation and its thermal conductivity is set as air's thermal conductivity at 300K. For the layer 1 and 3, their thermal conductivities are used as adjustable factors. The temperature of the robot chip and walking surface shown in Figure 4.13 is the reference for the simulation to do calibration. Figure 4.25 shows the comparison of the measurement and simulation results for the microrobot's heat-up curve. Figure 4.26 shows the comparison of cool-down curve. Because there is no rule to follow, the calibration was done by trial and error. Furthermore Figure 4.25 also shows

that the simulation results at 100Hz and 200Hz overlap. This agrees with the discussion in section 4.2 where it was stated that the heat generation at 100Hz and 200Hz step frequency has the same duty cycle. This simulation has tried an experimental idea. Although the result is close to the measurement, it still needs more experiments in the future to test its validity.

(a)

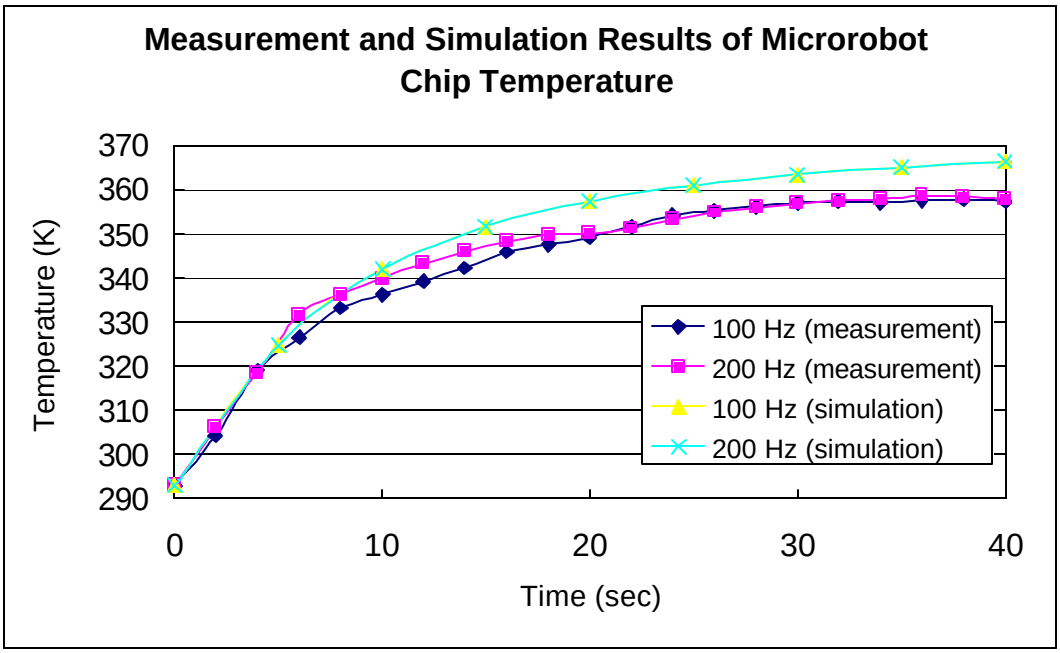

(b)

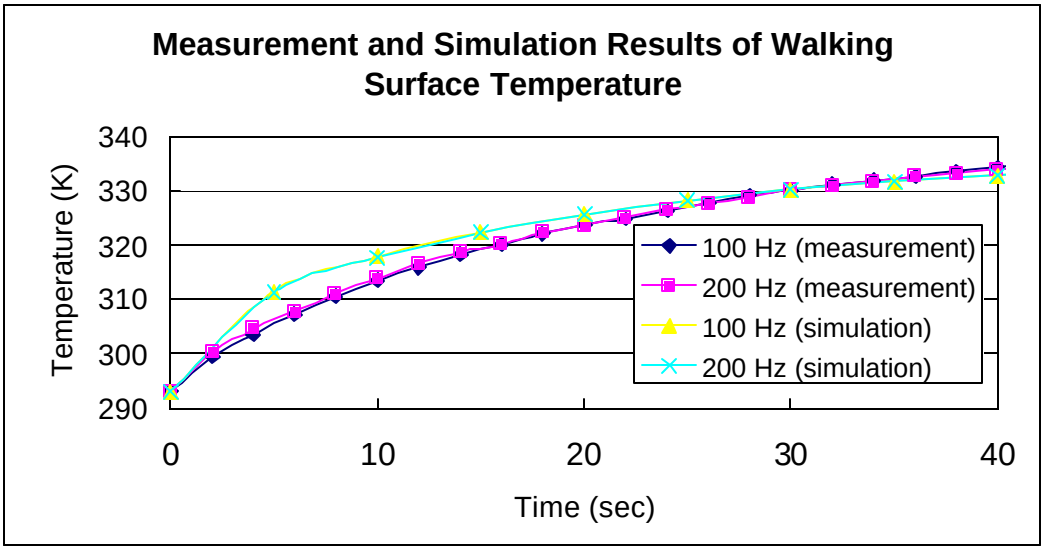

Figure 4.25: Temperature comparison of measurement and simulation results in the microrobot chip and the walking surface for heat-up curve.

(a)

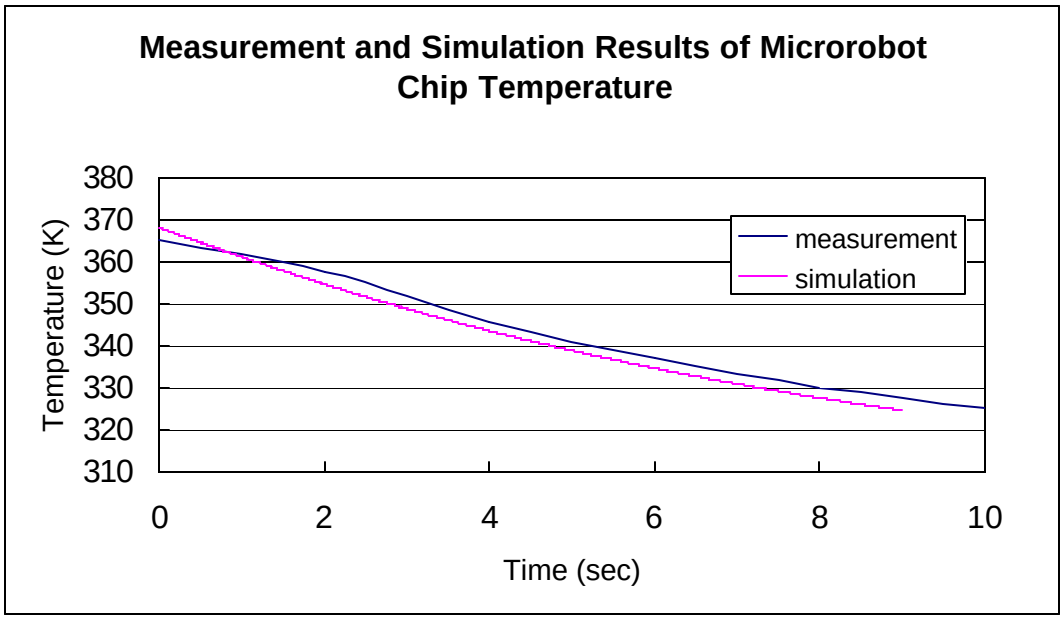

(b)

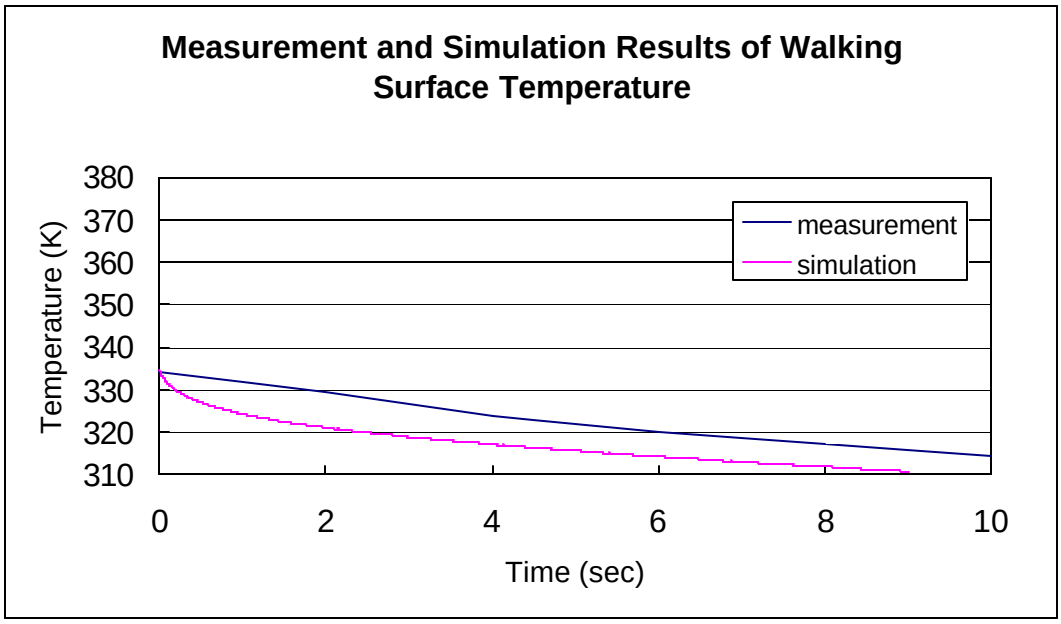

Figure 4.26: Temperature comparison of measurement and simulation results in the microrobot chip and the walking surface for cool-down curve.

Besides the heat transfer inside the gap, the heat dissipation from the robot chip and the walking surface into the surroundings through heat convection is the other key part in this simulation. The heat convection coefficient h is the dominating factor and it is temperature dependent. A surface with higher temperature has higher value of h. The geometry of the surface determines what empirical equation should be used to calculate h. Nusselt number is the dimensionless temperature gradient at the surface. It provides a measure of the heat convection and has an important relation with heat convection coefficient h shown in Equation 4.10. The k_{air} is the thermal conductivity of air.

$$\frac{h \cdot L_c}{k_{air}} = Nu \quad \text{.....(4.6)}$$

With this relation, the heat convection coefficient h can be found out and then applied into the simulation as a boundary condition. For detailed information, please reference Appendix A.

4.5.3 Micro Cilium Simulation

The final goal is to understand the heat transfer of the microscopic gap between the robot chip and the walking surface. The macroscopic simulation provides the boundary conditions for further microscopic simulations. To build a model representing the micro cilium is the first step of microscopic simulations. Because there is no detailed dimension from John Suh, the designer of this micro cilia array chip, all the dimensions are measured from SEM and microscope pictures. In order to be close to the

real situation, the simulation model is built as close to the real structure as possible. For the convenience of comparing, Figure 2.8 is shown in Figure 4.27 again and Figure 4.28 is the layout of the simulation model. The polyimide layers in 1 and 6 are the main layers having low ($2\,10^{-6}\,{}^{\circ}C^{-1}$) and high ($50\,10^{-6}\,{}^{\circ}C^{-1}$) coefficient of thermal expansion (CTE) respectively. The silicon nitride layers in layer 2 and 5 are stiffening layers to enhance the lifting capacity of the actuator. Compared with the Young' s modulus of the polyimide layers (8.6 and 2.7 GPa), the silicon nitride layers have a much larger value (183 GPa). Layer 3 is a heater resistor. It is routed by a Ti-W wire. Layer 4 is an Aluminum layer for electrostatic purpose. The main differences between the real structure and the simulation model are at layer 2 and 3. For simplification, the spine of layer 2 and 3 was built as continuous layers in the simulation model instead of the contour of the Ti-W resistor. Because of layer 5, it is reasonable to assume that the clearances in the spine of layer 2 and 3 are filled with silicon nitride. Since Ti-W has much higher Young' s modulus (340 GPa) than that of silicon nitride (183 GPa), this makes the simulation model stiffer.

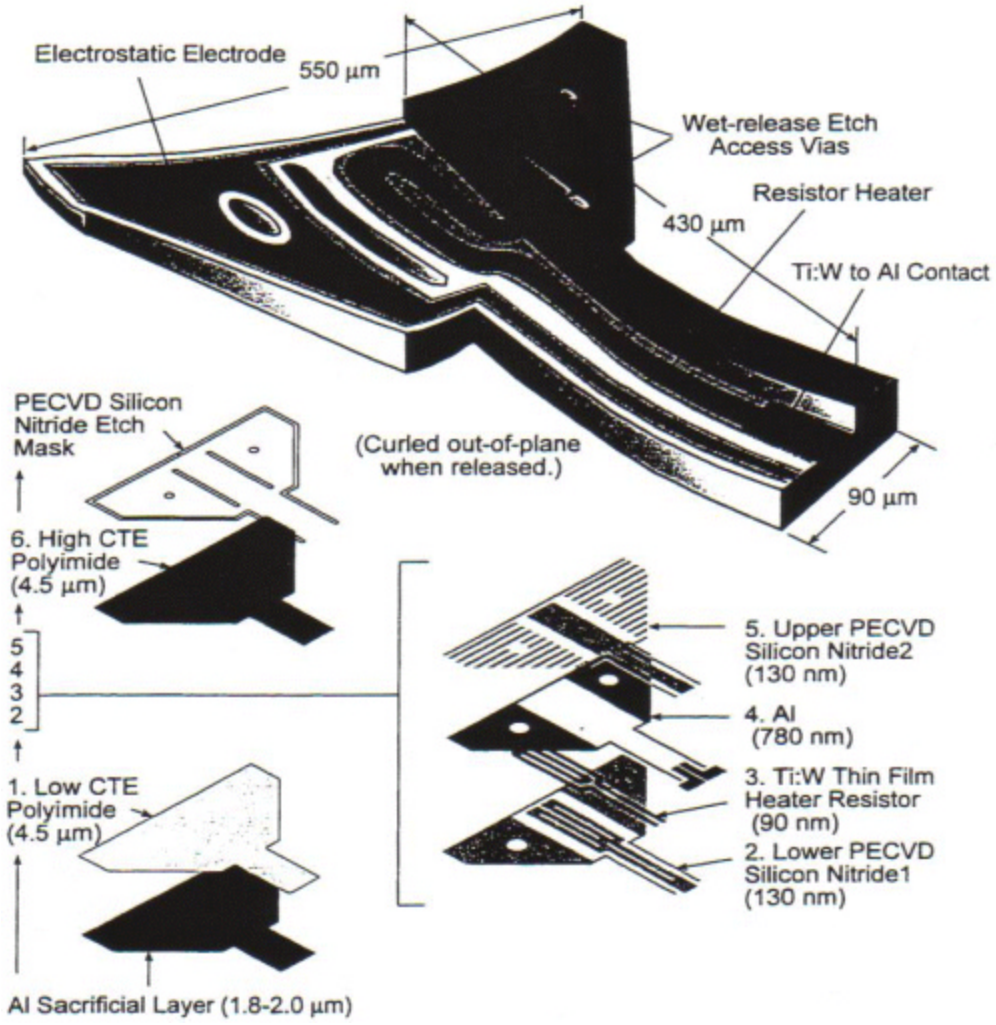

Figure 4.27: The illustration of the micro cilium and the detailed layout of its structure. The thickness of each layer is shown in the parenthesis. This plot is scanned from John Suh' s dissertation [5].

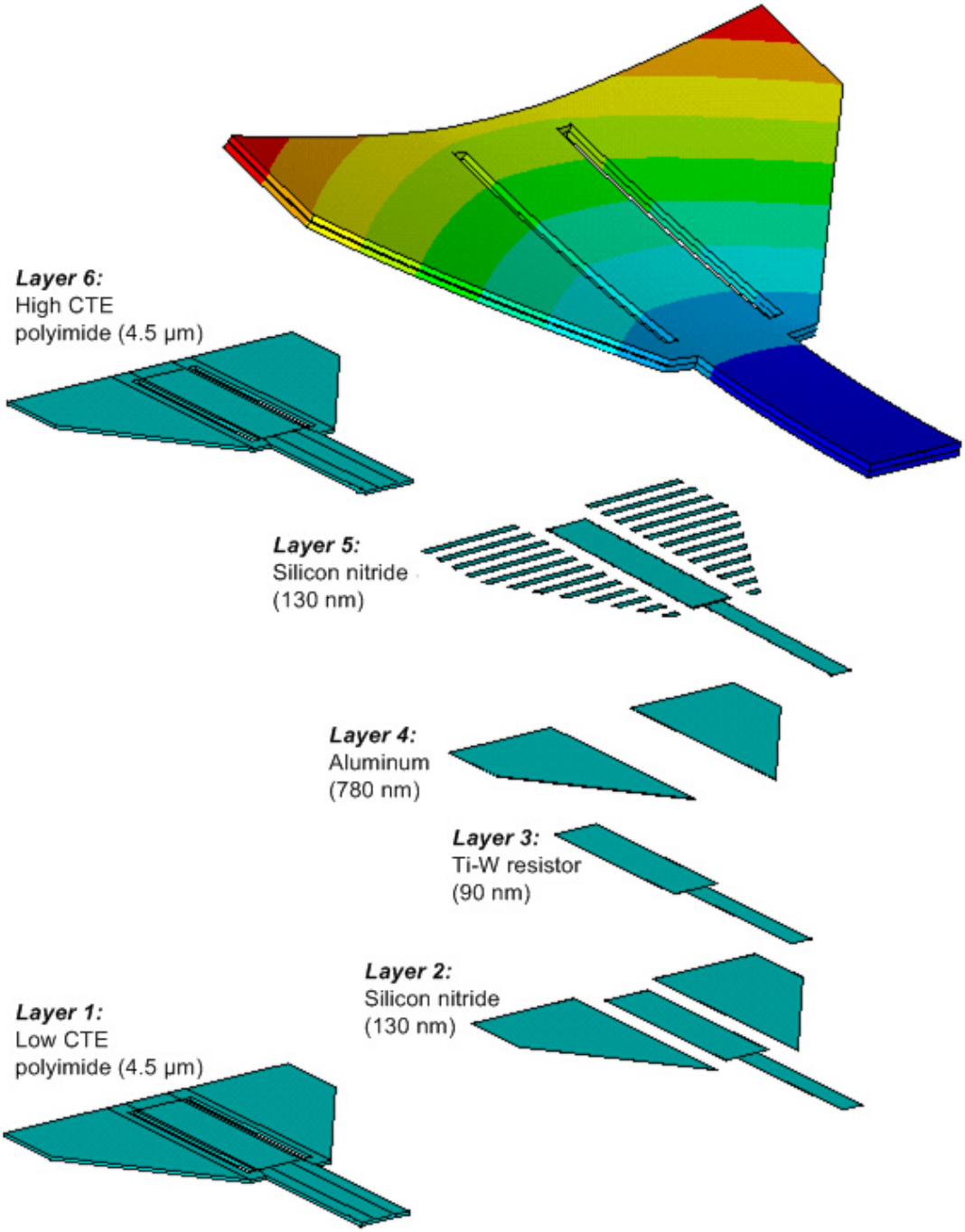

Figure 4.28: The illustration of the simulation model representing the micro cilium. The thickness of each layer is shown in the parentheses.

Figure 4.29 shows the result of steady state simulation. The micro cilium is at 25°C, room temperature, as defined in John Suh' s dissertation. It will totally lie down at 350°C. The height at position A and B are 116.73μm and 84.02μm respectively. The step size, which is the X direction displacement, is 3.83μm. John Suh' s measurement result [5] shows the height at position A and B are 117μm and 91μm respectively and the step size is 20μm. The simulation result has larger radius of curvature causing smaller step size because of stiffer spine.

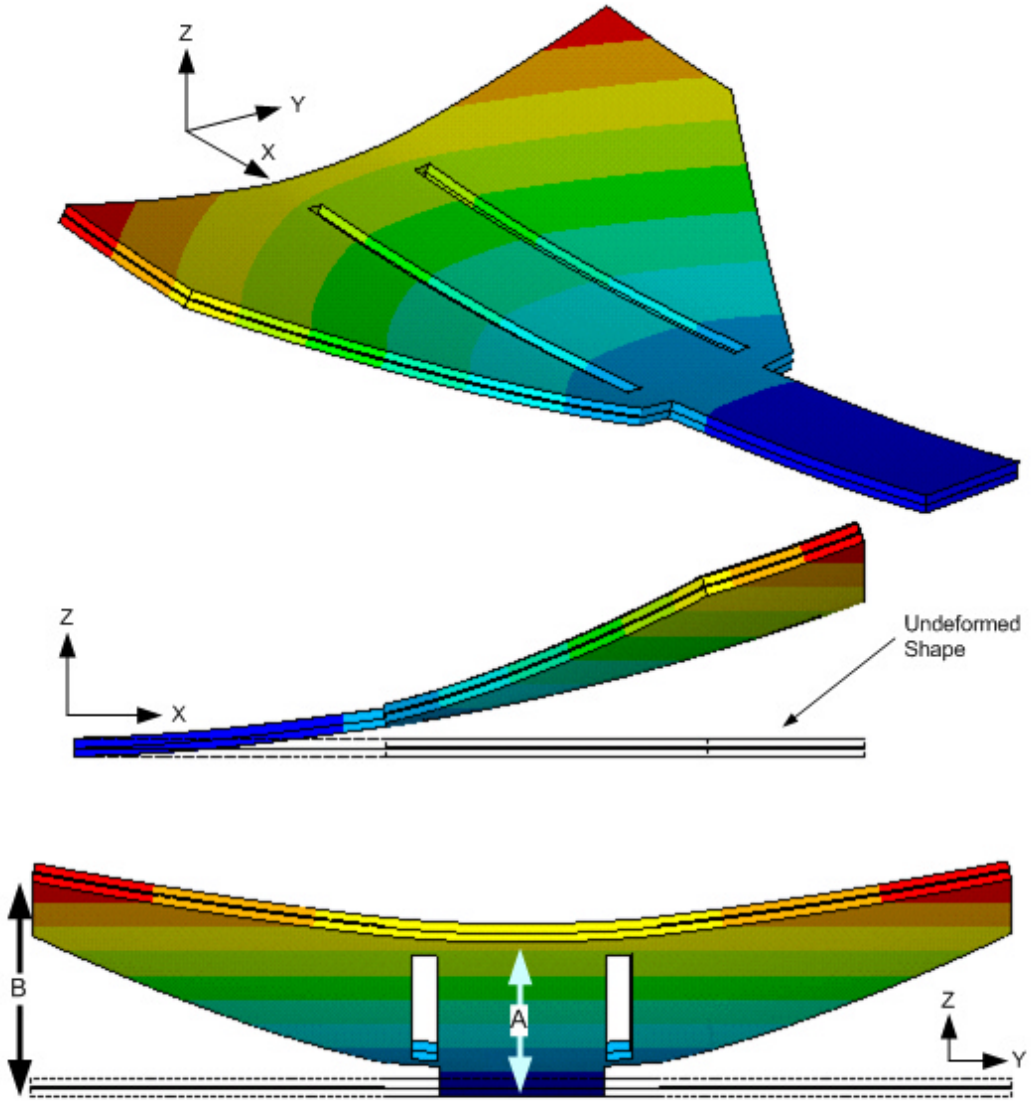

Figure 4.29: The simulation result of the micro cilium. The height of position A and B are 116.73μm and 84.02μm respectively. The X direction bending is 3.83μm.

4.5.4 Lifting Capacity

To test the lifting capacity, the following experiment was performed. Using the four-phase motion, in Figure 3.1 the robot moves one step forward from

phase 2 to phase 3 and moves the other step forward form phase 3 to phase 4. During these two steps, every micro cilia array chip uses 64 legs to support the microrobot' s weight. This means that these 128 legs need to be able to lift the robot up or the robot will not have any motion. In the experiment, the step frequency was 100Hz and the mass was gradually added on the microrobot until there is no movement anymore. The result shows that the microrobot can bear at maximum 3.524g. Figure 4.30 shows how the robot bears the mass.

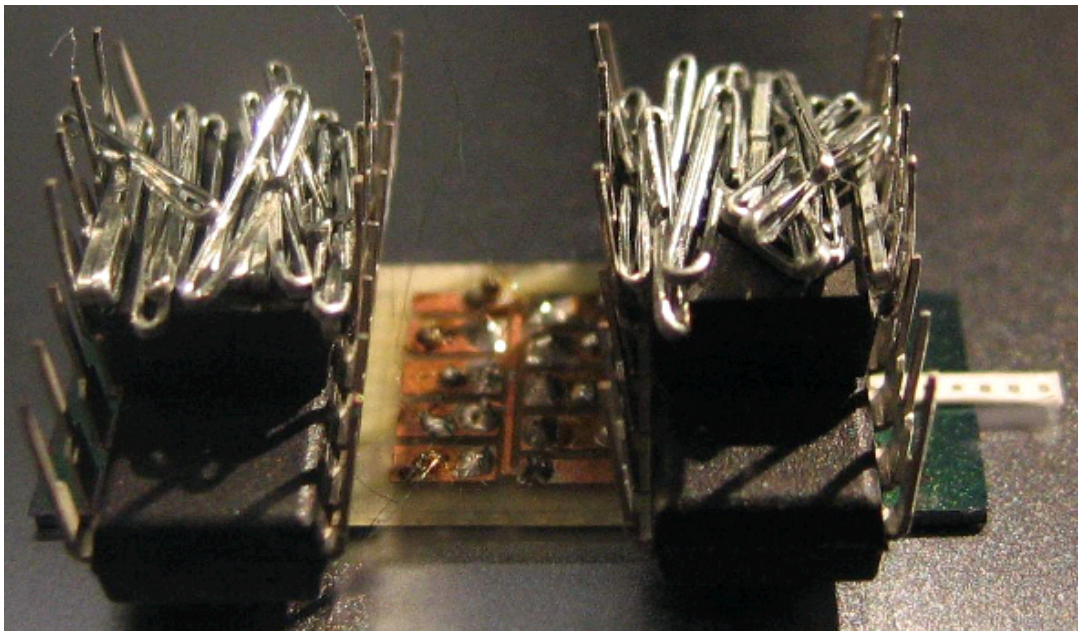

Figure 4.30: The microrobot can bear at maximum 3.524g consisting of two 16 pin ICs, two 8 pin ICs and 30 staples.

In the experiment, the mass includes two 16 pin ICs (0.983g each), two 8 pin ICs (0.464g each) and 30 staples (0.021g each). Figure 4.31 ~ 4.33 shows the dimension of them.

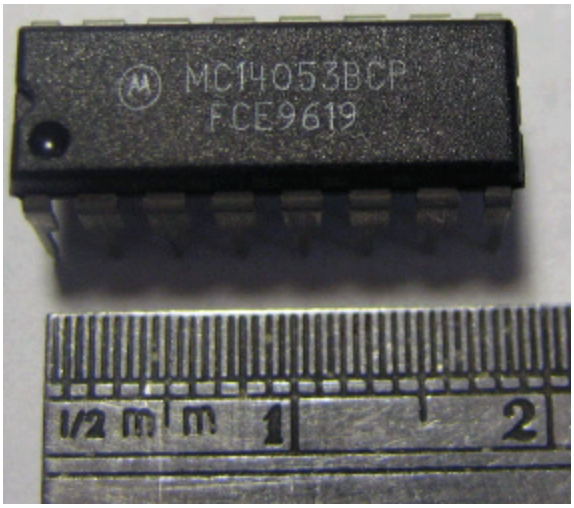

Figure 4.31: A 16 pin IC. It is about 2cm and 0.983g.

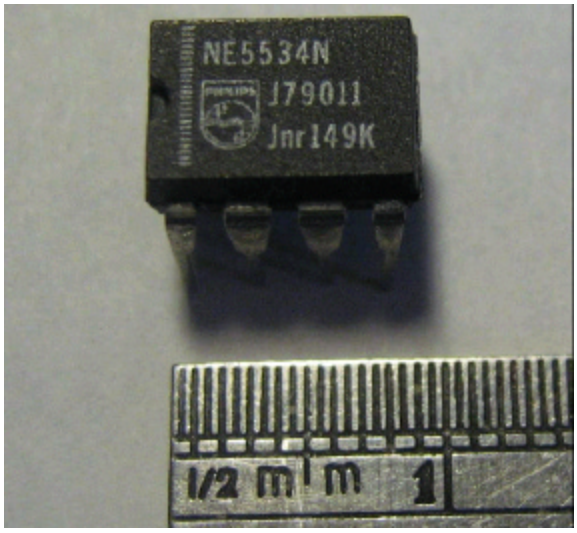

Figure 4.32: An 8 pin IC. It is about 1cm and 0.464g.

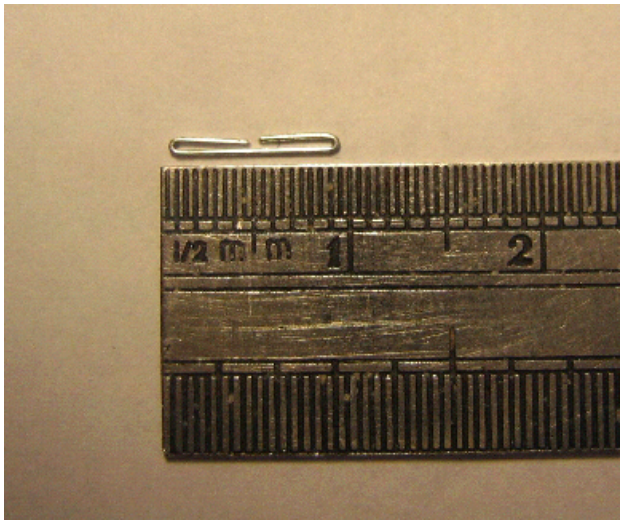

Figure 4.33: A staple. It is about 1cm and 0.021g.

Including the mass of the microrobot, which is 0.478g, 128 legs need to bear 4.002g. This means 306.40μN force on each micro cilium. Because every actuator uses two front tips to touch the walking surface, each tip bears 153.20μN force. The same force is applied on the simulation model and Figure 4.34 shows the result. The simulation result indicates that the micro cilium is totally flat. In the real situation, the spine of the micro cilium will touch the microrobot chip when it gradually lies down. If this is included in the simulation, the model will need more force to be flattened because the micro cilium gradually becomes shorter and requires more force to create enough bending moment to lay it down. A force bigger then 153.20μN will be needed to totally flatten the simulation model. This indicates that the simulation model is stiffer then the real micro cilium. However this simulation model is already close to the real situation.

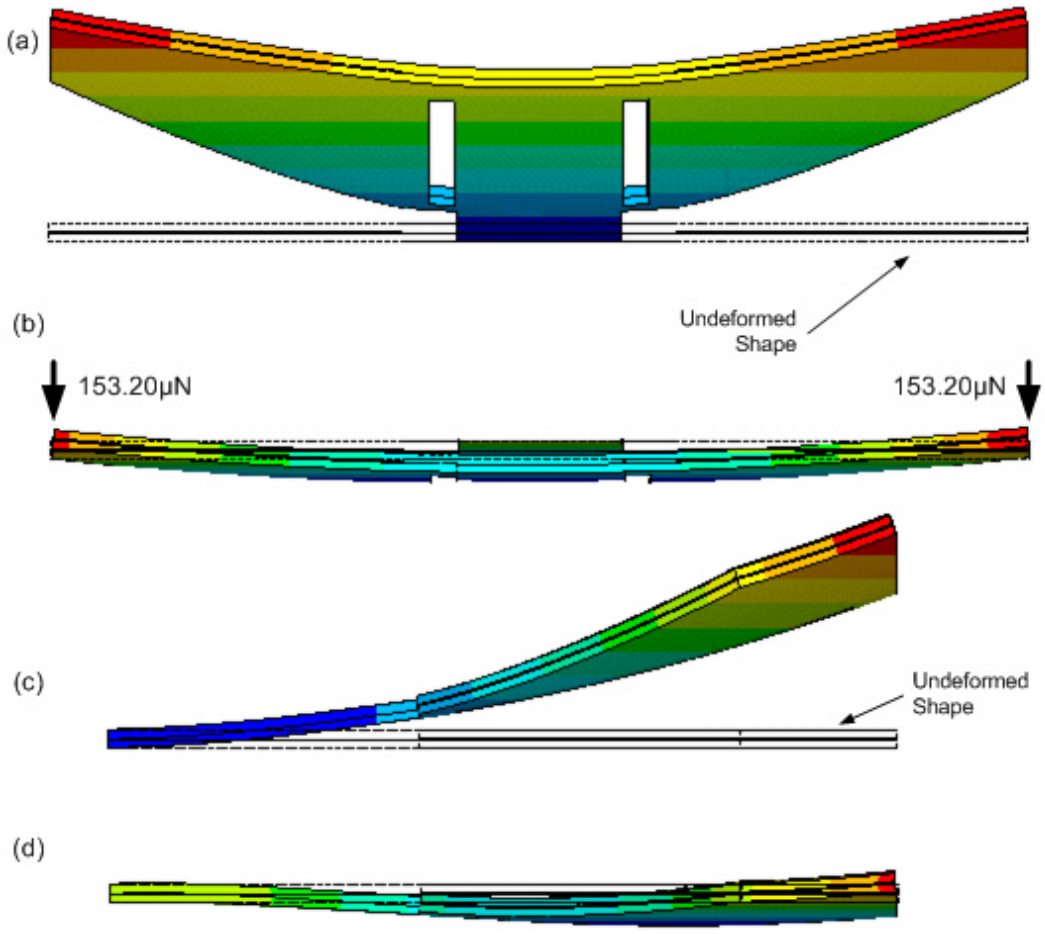

Figure 4.34: The simulation result of applying force on the micro cilium. (a) front view before applying force (b) front view after applying force (c) side view before applying force (d) side view after applying force

4.5.5 FSI Simulation

This is the last step of the simulations in this project. It is about using the fluid and solid interaction simulation, which is a CFD and structure coupled simulation, to represent the heat transfer of the top and bottom air layers shown in Figure 4.21. Although the simulation is not successful, this section describes the considerations in the simulation and also the reasons for failure.

To predict the heat transfer of the top and bottom air layers, only considering one micro cilium is not enough. Figure 2.5 is quoted in Figure 4.35. The four actuators in every motion cell dissipate heat at different timings in each four-phase motion and the heat transfer in the air is influenced from all four actuators. Furthermore, the Ti-W resistor wiring outside the actuators is also a part of the heat source. Therefore it is more appropriate to consider a whole motion cell instead of one single actuator.

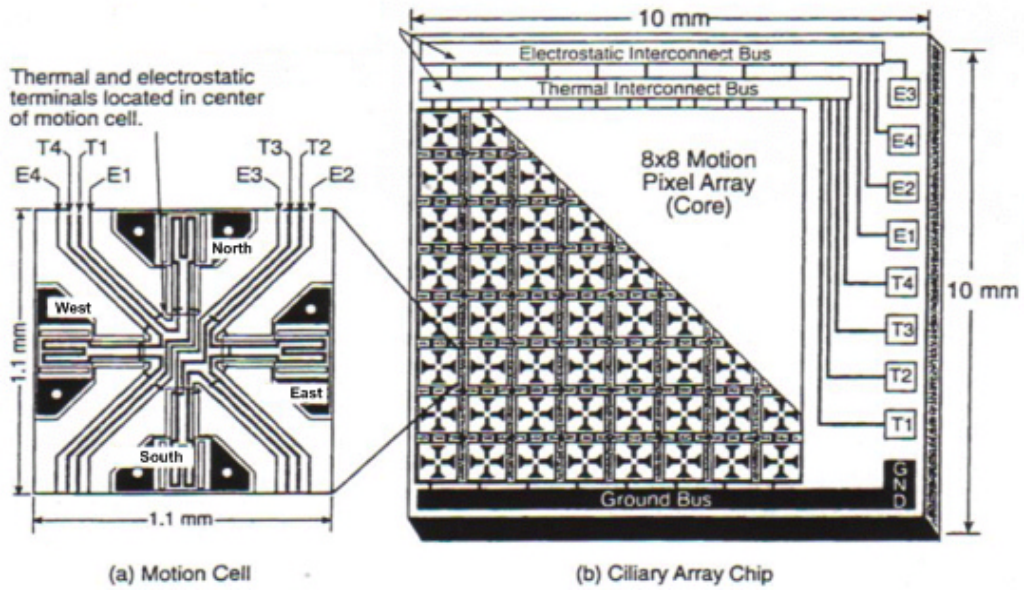

Figure 4.35: Schematic of micro cilia array chip and one motion cell. This figure is scanned from John Suh' s dissertation [5]. The T1 through T4 labels mark the thermal control wires and the E1 through E4 labels mark the electrostatic control wires.

This simulation is performed in ANSYS using Fluid-Solid Interaction (FSI) simulation. Typical fluid-solid interaction applications include the following [12]:

1. Problems that involve coupling of thermal, structural, or electrical fields with flow fields.

2. Problems that involve flow induced structural motion.

3. Problems that involve flow caused by solid deformation.

This project belongs to category 1 and 3. The model of this simulation includes a solid part and a fluid part. The solid part is composed of four micro cilia and the Ti-W resistor wiring outside the actuators. The fluid part represents the air enclosing the solid part. Figure 4.36 explains the solid part of the model and Figure 4.37 shows the solid part, fluid part and their combination.

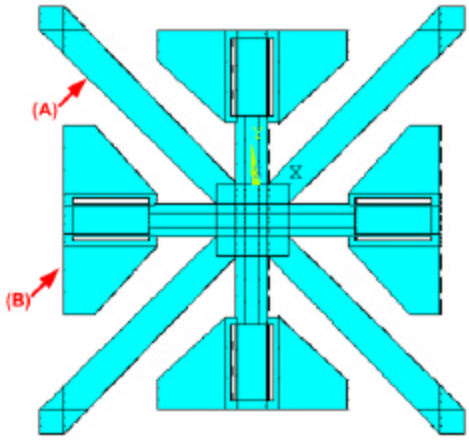

Figure 4.36: The solid part of the FSI simulation model. (A) The Ti-W resistor outside the micro cilia (B) the micro cilia

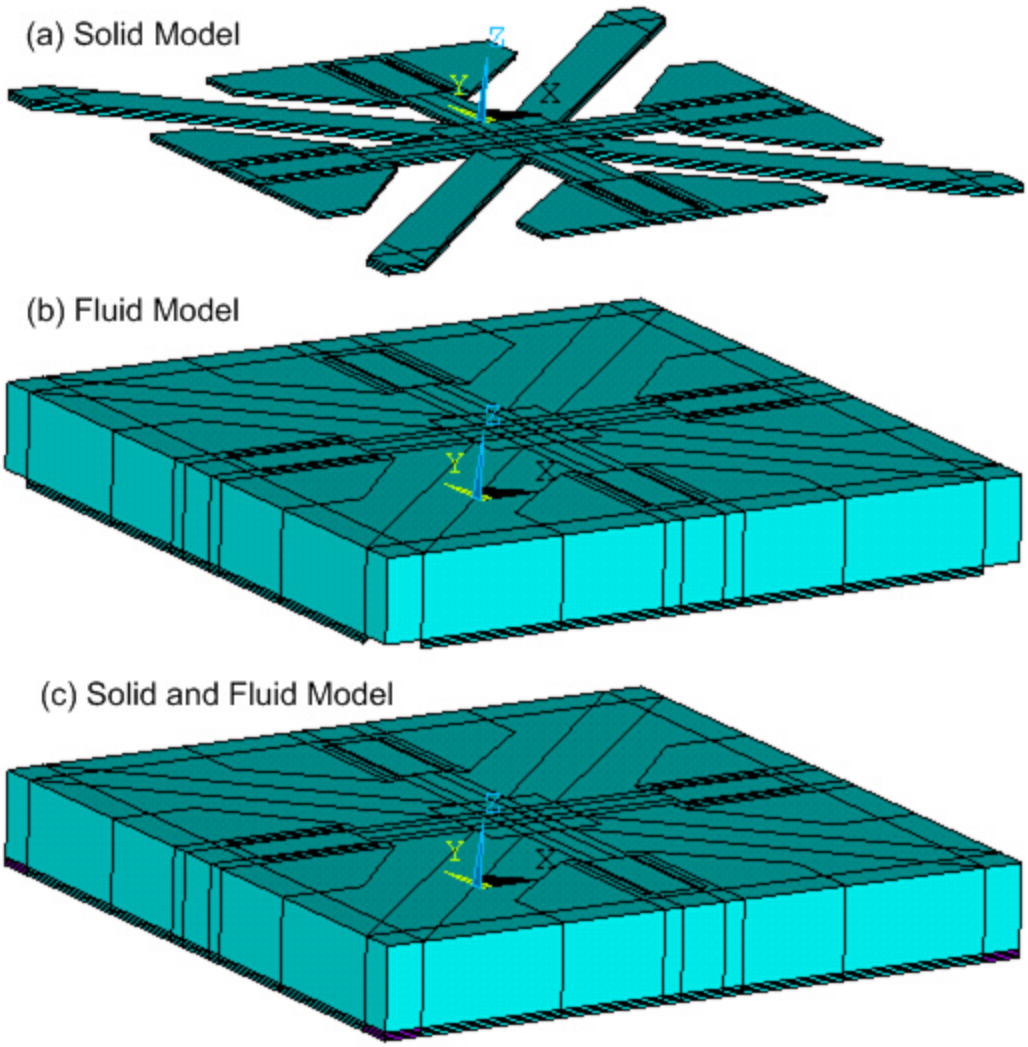

Figure 4.37: The composition of the FSI simulation model. (a) solid part (b) fluid part (c) combination. The solid model is enclosed by the fluid model.

Figure 4.38 shows the length, width and thickness of the fluid part. Since the solid is enclosed by the fluid, the dimension of the fluid part also represents the dimension of the whole model. The model is cut into several pieces for the purpose of meshing. This model is set as micro cilia array chip facing up and the micro cilia are fully flat. They curve up depending on their temperature during the simulation.

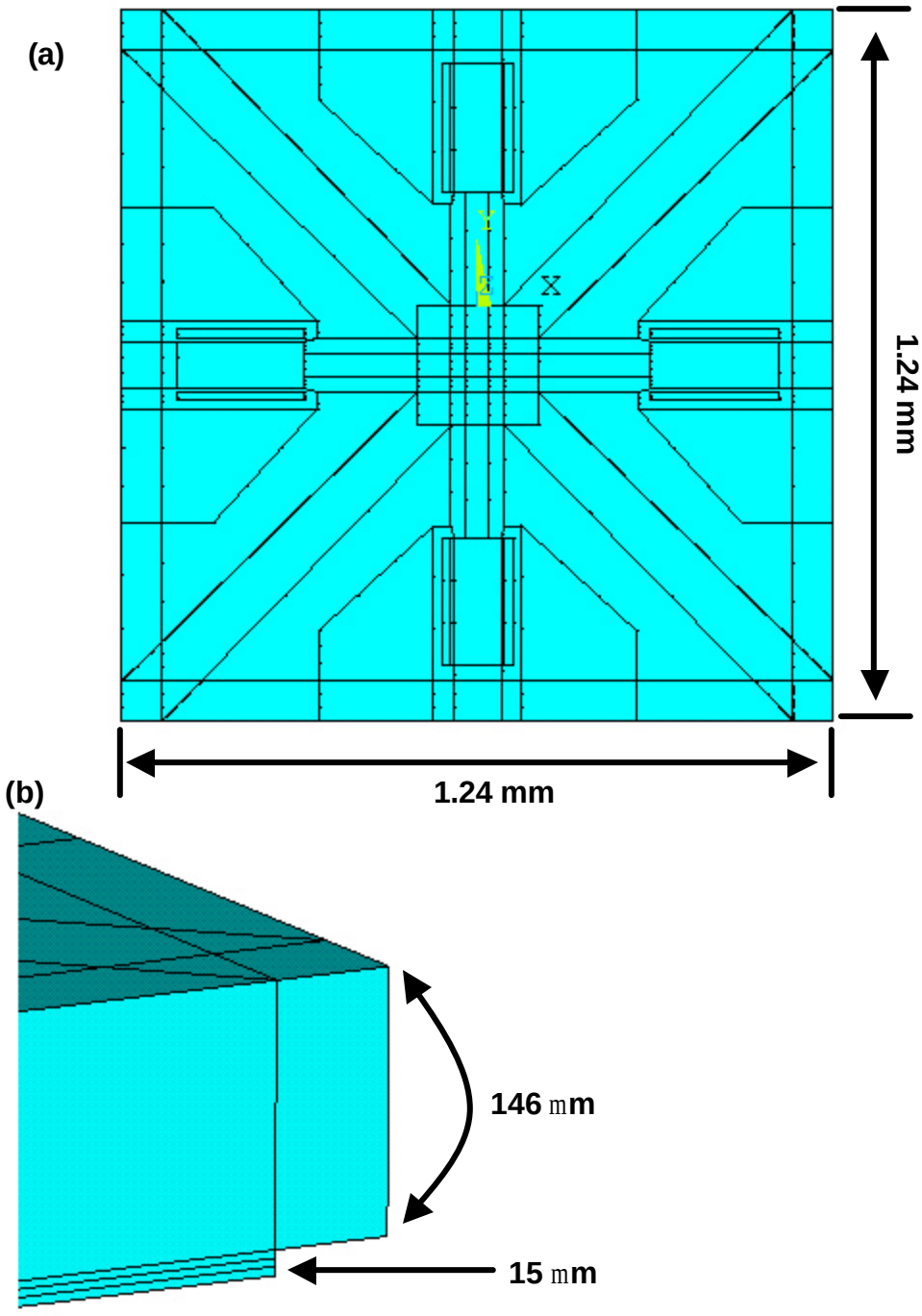

Figure 4.38: The length, width and thickness of the fluid part in the simulation model.

The fluid speed induced by the robot's movement was ignored because with the viscosity force of air and the retardation from the micro cilia, the fluid speed is unknown. The area of one motion cell is 1.1mm×1.1mm and the thickness of the gap between robot chip and the walking surface is about 120μm. This simulation model is larger because if flow fluctuations are close to any boundary, it will increase the possibility of divergence in the simulation.

Figure 4.39 shows the solution algorithm of the FSI simulation. The fluid-solid interaction solver solves the equations for the fluid and solid domains independently of each other. It transfers fluid forces and heat fluxes and solid displacements, velocities, and temperatures across the fluid-solid interface. The algorithm continues to loop through the solid and fluid analyses until convergence is reached for that time step [12].

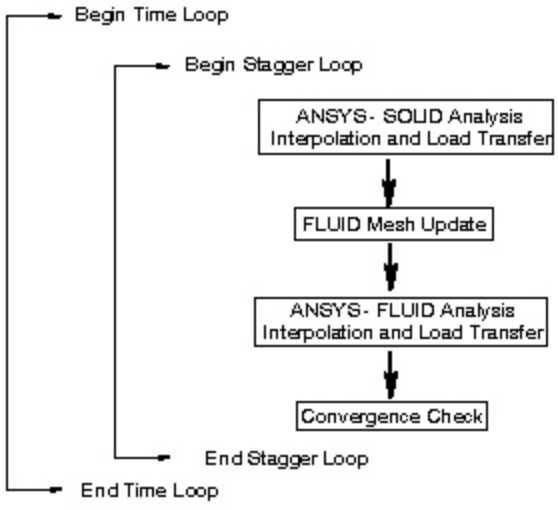

Figure 4.39: Fluid-Solid Interaction Solution Algorithm copied from ANSYS manual [12].

Although this simulation covers most factors in the real situation, the simulation never converged. There are two main reasons. First, this model is large and needs a huge number of elements. This causes an unacceptably slow convergent process. Second, the fluid simulation is intrinsically sensitive and can easily diverge the calculation. The gap between the robot chip and the walking surface is narrow. The flow fluctuations caused by the motion of the micro cilia are too close to the boundaries. Although the model was already built larger than the physical system, it is still not large enough. By further expanding the model, it will lose realism.

Chapter 5

CONCLUSION AND FUTURE WORKS

All possible applications of this microrobot base on the degree of understanding to the microrobot. Summing up this research, the micro robot shows its predictable and controllable characteristics for further applications. In this chapter, the summarized results will be described in the conclusion section. The unfinished work and the next step of research are discussed in the future work section.

5.1 Conclusion

The characteristics of this microrobot have been extensively studied. The microrobot' s motion model from previous research [10] can closely fit the experimental results. Our experiments also show that the microrobot's speed has a strong correlation to the temperature of the robot chip and its walking surface. This makes the temperature a good feedback factor for the microrobot control in the future. From studying the heat dissipation in the four-phase motion, it appears that with proper control the influence of changing step frequency can be decreased and the stability of the robot speed increases. This can have a contribution to increasing the accuracy of the robot control. The lifting capacity test shows that the microrobot can carry 7.4 times its own mass, which is 3.524g. Because practically information about the heat transfer inside the gap between the robot chip and the walking surface is difficult to be observed from experiments, the

simulation software provides a method to compensate for it. The simulations begin from macroscopic model to detailed microscopic model. Although the FSI simulation is not successful, the macroscopic simulation and the micro cilium model have provided a foundation for a future simulation model, which would be used to represent the high-resolution structures and heat transfer inside the gap.

5.2 Future Works

This microrobot is omnidirectional and able to move in three degrees of freedom (X, Y, ?). In this research, only the motion in one degree of freedom (DOF) was studied. Although the motion in other DOFs had been tested in previous research [10], the motion model, Equation 4.1, which fit very well in this research, has not been fully verified in other degrees of freedom.

The LabVIEW code for the robot control already provides much flexibility to operate the microrobot. However it has not been able to change operational factors, like step frequency, simultaneously while running. Furthermore the microrobot' s motion has strong correlation to the temperature of the robot chip and its walking surface. The quiescent time set in the LabVIEW code can influence the temperature of the robot chip and its walking surface but also influence the duty cycle of the robot' s motion. It would be interesting to see what impact the quiescent time can make.

Simulation is an important tool for understanding the microrobot. Because the FSI model covers the detailed structure of the motion cell and its

success could provide much valuable information about the temperature distribution of the micro cilia, how micro cilia' s motion induces air flow and how the heat generation from micro cilia influences each other, it is still worthy trying to conquer its technical problem. Since the micro cilium model is close to the real situation, it is probably a good approach to use the high speed camera for capturing the microrobot' s movement in Z direction, which would lead to an estimate of the heat transfer inside the gap. Then the assumptions and estimations could be tested on the micro cilium model.

Although the macroscopic simulation is an experimental idea, it could probably become a helpful tool. By continuously improving the structure in the gap and doing finer calibration to match the reference temperature, the heat transfer between the robot chip and the walking surface in the simulation could help understand the heat transfer in the reality.

LIST OF REFERENCES

[1] S Hollar, A Flynn, C Bellew, K S J Pister, "Solar Powered 10 mg Silicon Robot," *IEEE MEMS*, Kyoto, Japan, Page(s):706 – 711, January 19-23 2003.

[2] C. Levey, C. McGray, D. Rus, and M. Sinclair, "Untethered Micro-Actuators for Autonomous Micro-robot Locomotion: Design, Fabrication, Control, and Performance", *Robotics Research* eds. P. Dario and R. Chatila. Springer-Verlag (London) 2005, pp.502—516

[3] Kiaditis, P.E.; Bright, V. M.; Harsh, K. F.; Lee, Y.C. "Prototype microrobots for micro positioning in a manufacturing process and micro unmanned vehicles", Micro Electro Mechanical Systems, MEMS '99. Twelfth IEEE International Conference, 1999 Page(s):570 – 575, 17-21 Jan 1999

[4] T. Ebefors, J. U. Mattson, E. Kaelvesten, G. Stemme, "A Walking Silicon Micro-Robot", the 10th Int. Conference on Solid-State Sensors and Actuators (Transducers' 99), Sendai, Japan, pp 1202-1205, June 7-10, 1999

[5] John Suh, "Polyimide-Bimorph Ciliary Actuator Arrays: Demonstrations Of A CMOS Compatible Microfabrication Technology", Ph.D. dissertation, Stanford University, CA, February 2001

[6] K. F. Böhringer, J. F. Suh, B. R. Donald, G. T. A. Kovacs, "Vector Fields for Task-level Distributed Manipulation: Experiments with Organic Micro Actuator Arrays." *IEEE International Conference on Robotics and Automation (ICRA)*, pp. 1779-1786, Albuquerque, New Mexico, April 20-25, 1997

[7] K. F. Böhringer, B. R. Donald, Lydia Kavraki, Florent Lamiraux, "Part Orientation with One or Two Stable Equilibria Using Programmable Vector Fields." *IEEE Transactions on Robotics and Automation,* 16(2):157-170, April 2000

[8] R. B. Darling, J. W. Suh, and G. T. A. Kovacs, "Ciliary Microactuator Array for Scanning Electron Microscope Positioning Stage," J. Vac. Sci. Tech. A, vol. 16, no. 3, pp. 1998-2002, May/Jun. 1998

[9] Mason L. Terry, Joel Reiter, Karl F. Böhringer, John W. Suh, and Gregory T. A. Kovacs, "A Docking System for Microsatellites Based on MEMS Actuator Arrays." IOP Journal of Smart Materials and Structures 10(6):1176-1184, December 2001.

[10] Matthew H. Mohebbi, Mason L. Terry, Karl F. Böhringer, John W. Suh, and Gregory T. A. Kovacs, "Omnidirectional Walking Microrobot Using MEMS Thermal Cilia Arrays" ASME International Mechanical Engineering Congress and Exposition (IMECE'01), no. 23824, New York, NY, November 11-16, 2001

[11] Frank P. Incropera, and David P. De Witt, "Introduction To Heat Transfer (2nd Edition)", John Wiley & Sons Book Co., New York, NY, 1990

[12] "Fluid-Solid Interaction Solver", Chapter 3, Coupled-Field Analysis Guide, ANSYS Release 8.1 manual

[13] Eric C. Guyer, and David L. Brownell, "Handbook of Applied Thermal Design", McGraw-Hill Book Company, New York, NY, 1989

Appendix A

MACROSCOPIC SIMULATION

A.1 Dimension and Material Properties

Figure A.1, A.2 and A.3 are the dimensions of the simulation model. The scale in Figure A.3 is exaggerated for representing the structure more clearly. Figure A.4 shows the material properties used in this simulation corresponding to Figure A.3. The material properties of PCB are assumed close to polyimide and cited from MatWeb (http://www.matweb.com/). Because the material No. 8 contains PCB and copper, its material property is set as an average of PCB and copper. The element type used in the simulation is Solid70.

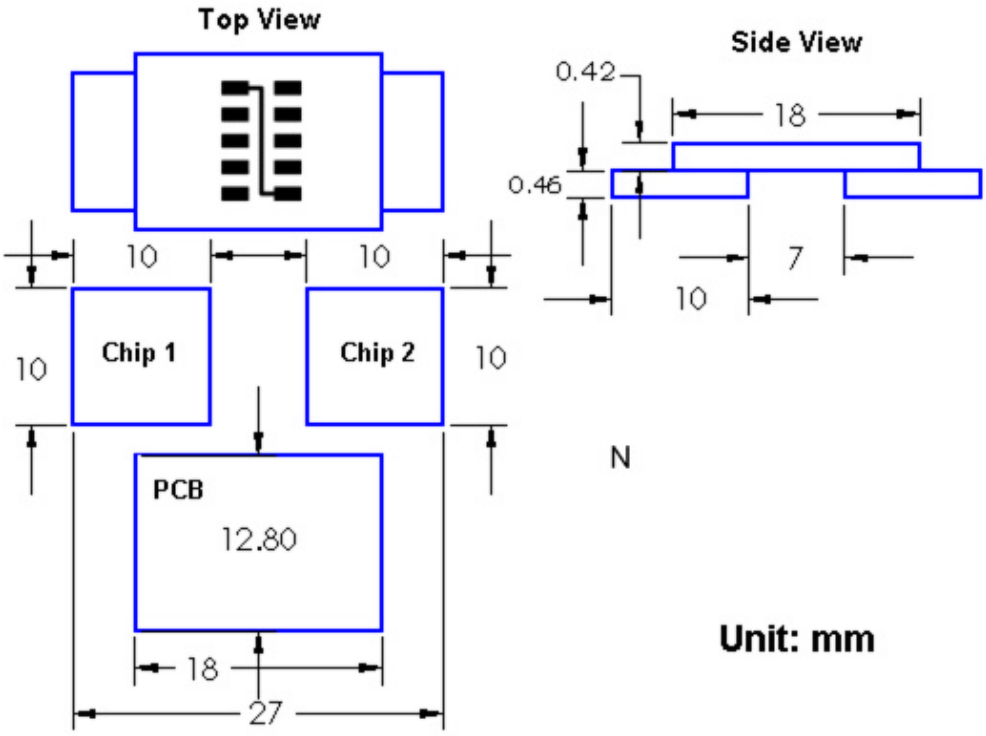

Figure A.1: Dimension of the microrobot.

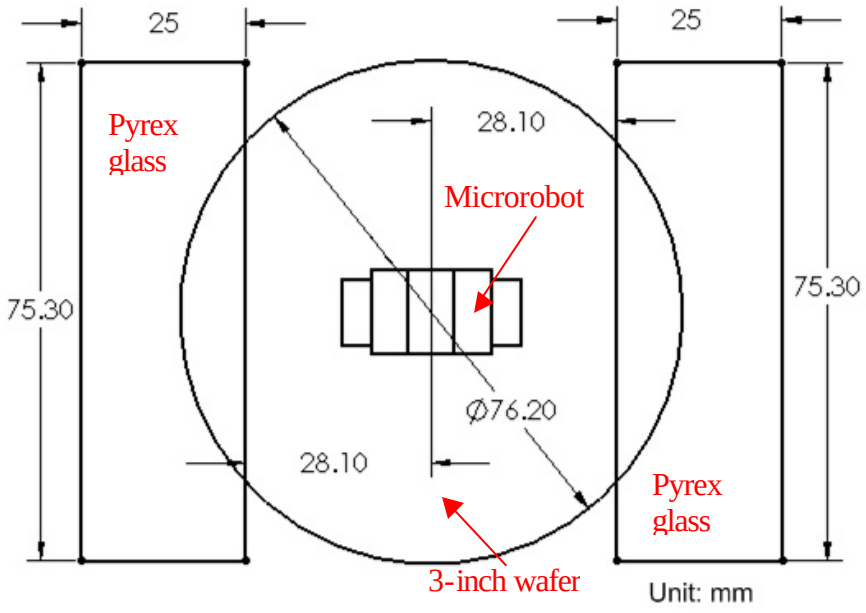

Figure A.2: Position of the microrobot. Dimension of the 3-inch wafer and the pyrex glass.

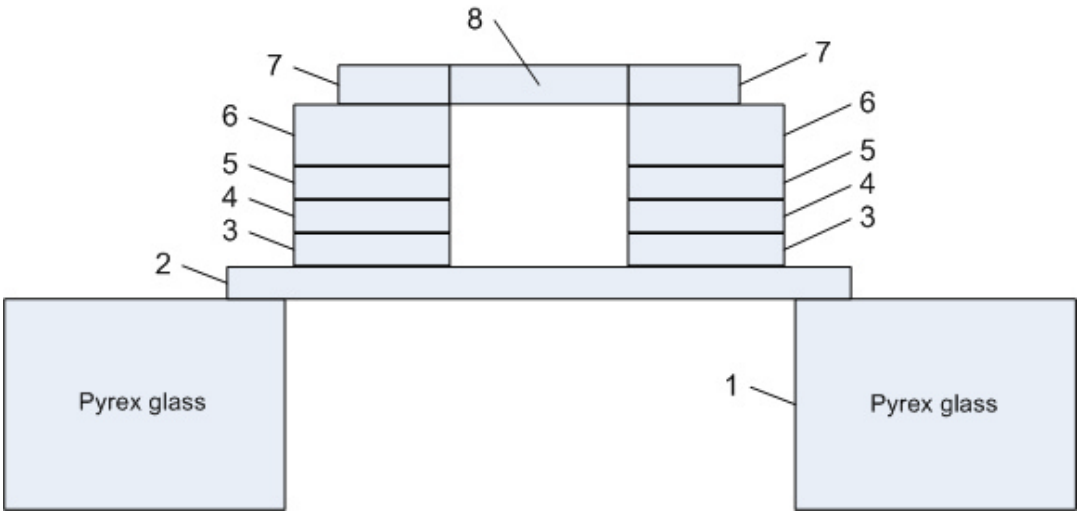

Figure A.3: Side view of the simulation model. The scale is exaggerated for clearer presentation. Figure A.4 contains the list of the material properties corresponding to the indicated material numbers.

No.	Name	Density (kg/m^3)	Thermal Conductivity ($W/m \cdot K$)	Specific Heat C_p ($J/kg \cdot K$)	Thickness
1*	Pyrex glass	2225	1.4	838	5.1mm
2	Silicon	2330	148	712	0.46mm
3	Gap layer 1	1.1614	0.02	1007	40µm
4	Gap layer 2	1.1614	0.0263	1007	40µm
5	Gap layer 3	1.1614	0.04	1007	40µm
6	Silicon	2330	148	712	0.46mm
7	PCB	1400	0.25	1200	0.42mm
8	PCB and copper*	5166.5	200.625	792.5	0.42mm
(*) From Introduction To Heat Transfer [11]					

Figure A.4: Material properties corresponding to Figure A.3.

A.2 Heat Generation

In the simulation, the heat is generated in gap layer 2 using Fourier Series to express the heat generation function. Fourier Series represents a given periodic function in terms of cosine and sine functions. Calculating from the resistance measurement in Figure 2.7, the average resistance of each set of legs is 2.192kO. Each set of legs averagely generates 1.65W power. Figure A.5 shows the heat power in every phase of the four-phase motion.

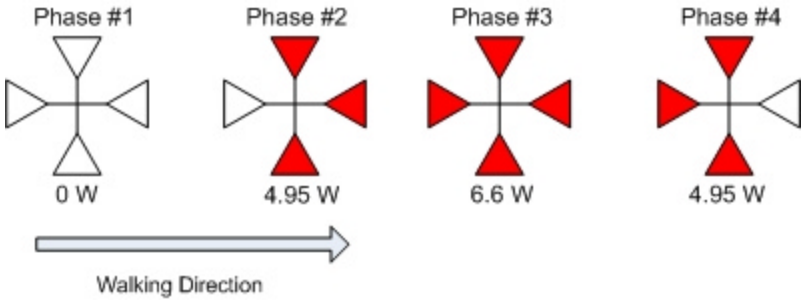

Figure A.5: Heat power in every phase of the four-phase motion.

The heat generation in ANSYS is defined as Watt per unit volume (W/m^3). The volume of the gap layer 2 between each robot chip and the walking surface is 1cmx1cmx40µm. Equation A.1 is the heat generation function, which is a function of time and the step frequency is set at 100Hz. Figure A.6 shows the plot of Equation A.1.

$$
\begin{aligned}
&1.02625\times10^{9} - 5.22665\times10^{8}\,Cos(157.08\cdot t)\\
&+1.74222\times10^{8}\,Cos(471.239\cdot t) - 1.04533\times10^{8}\cdot Cos(785.398\cdot t)\\
&+7.46664\times10^{7}\,Cos(1099.56\cdot t) - 5.22665\times10^{8}\,Sin(157.08\cdot t)\\
&-2.61332\times10^{8}\,Sin(314.159\cdot t) - 1.74222\times10^{8}\,Sin(471.239\cdot t)\\
&-1.04533\times10^{8}\,Sin(785.398\cdot t) - 8.71108\times10^{7}\,Sin(942.478\cdot t)\\
&-7.46664\times10^{7}\,Sin(1099.56\cdot t)
\end{aligned}
\qquad \text{……..(A.1)}
$$

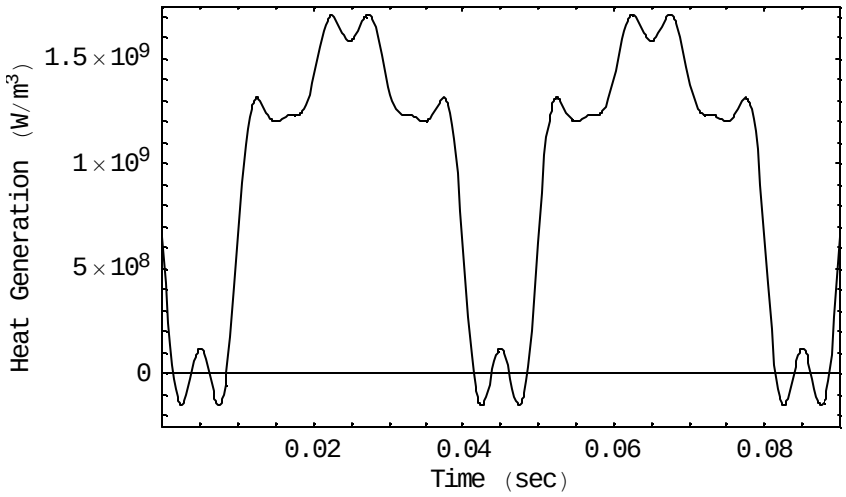

Figure A.6: Plot of Equation A.1

A.3 Boundary Conditions

Figure A.7 indicates where the boundary conditions were applied. Heat convection was applied on surface 1~6 and the bottom of the pryex glass were set at 22°C, which is the average temperature in our lab. The surface 1~4 are classified as hot flat plate facing up and the surface 5~6 are classified as vertical flat plate. All the following equations in this section are from Handbook of Applied Thermal Design [13].

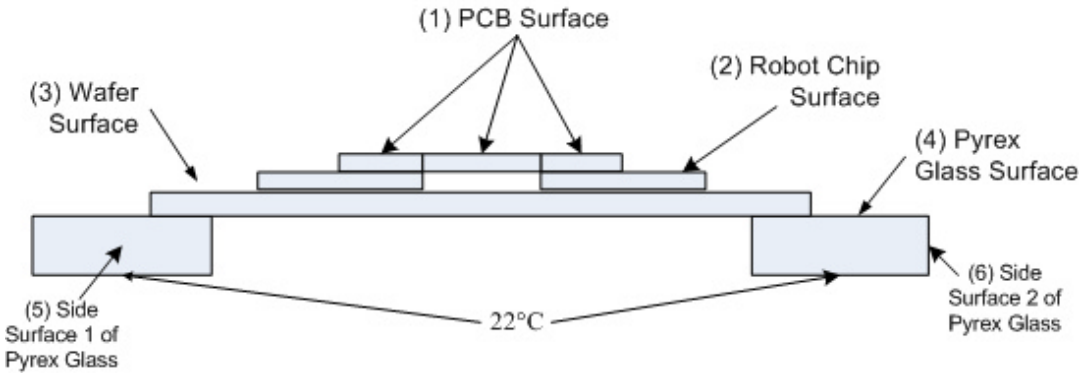

Figure A.7: A schematic indicates where the boundary conditions are applied.

A.3.1 Hot Flat Plate Facing Up

The ambient temperature is 295K and the heat convection coefficient h is a function of surface temperature $T_{surface}$. The heat convection coefficient h has a correlation with Nusselt number showed in Equation A.2.

$$Nu = \frac{h \cdot L_c}{k_{air}} = [(Nu_l)^{10} + (Nu_t)^{10}]^{1/10} \quad \text{.....(A.2)}$$

$$L_c = (plate\_surface\_area)/(plate\_perimeter) \quad \text{.....(A.3)}$$

$$k_{air} : 0.0263 \ (\text{W/K} \cdot \text{m})$$

$$Nu_l = \frac{1.4}{\ln[1 + 1.677/(0.515 \cdot Ra_L^{1/4})]} \quad \text{.....(A.4)}$$

$$Nu_t = 0.14 \cdot Ra^{1/3} \quad \text{.....(A.5)}$$

$$Ra_L = \frac{g \cdot b \cdot \Delta T \cdot L_c^3}{u \cdot a} \quad \text{.....(A.6)}$$

g : 9.8 m/s^2

b : 0.0033

u : 15.89· 10^{-6} (m^2/s)

a : 22.5· 10^{-6} (m^2/s)

(1) PCB Surface:

$$L_c = 0.00374$$

$$Ra_L = 4.731\left(T_{surface} - 295\right)$$

(2) Robot Chip Surface:

$$L_c = 0.00155$$

$$Ra_L = 0.3368\left(T_{surface} - 295\right)$$

(3) Wafer Surface:

$$L_c = 0.01905$$

$$Ra_L = 625.343\left(T_{surface} - 295\right)$$

(4) Pyrex Glass Surface:

$$L_c = 0.00938$$

$$Ra_L = 74.652\left(T_{surface} - 295\right)$$

Figure A.8~A.11 are the plots of the heat convection coefficient h from the calculations above.

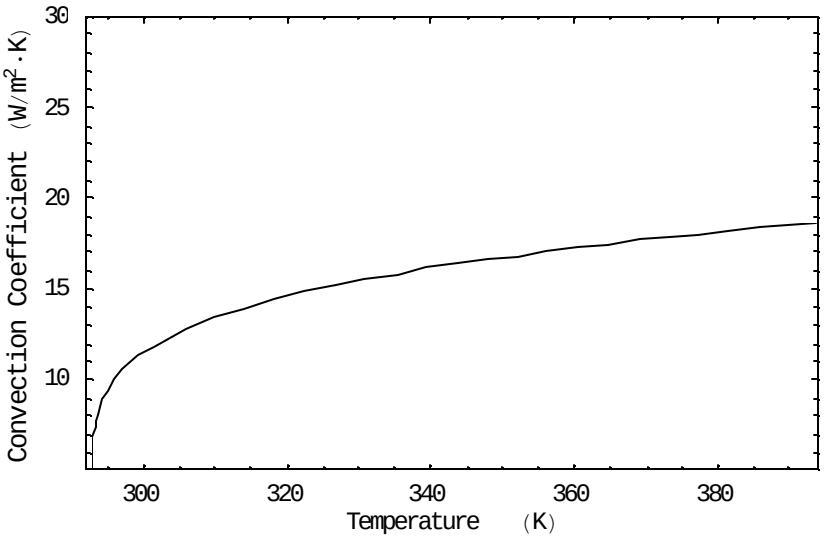

Figure A.8: Plot of the heat convection coefficient for the PCB surface.

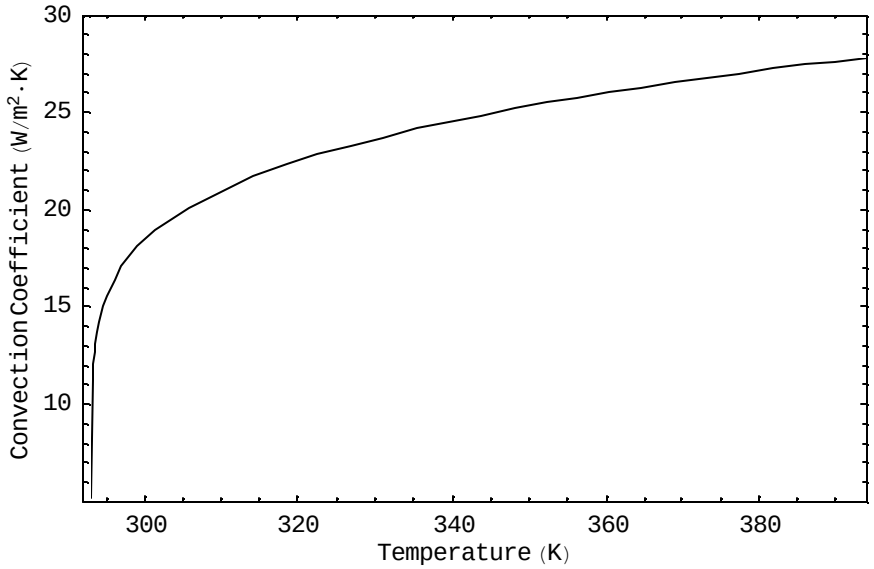

Figure A.9: Plot of the heat convection coefficient for the robot chip surface.

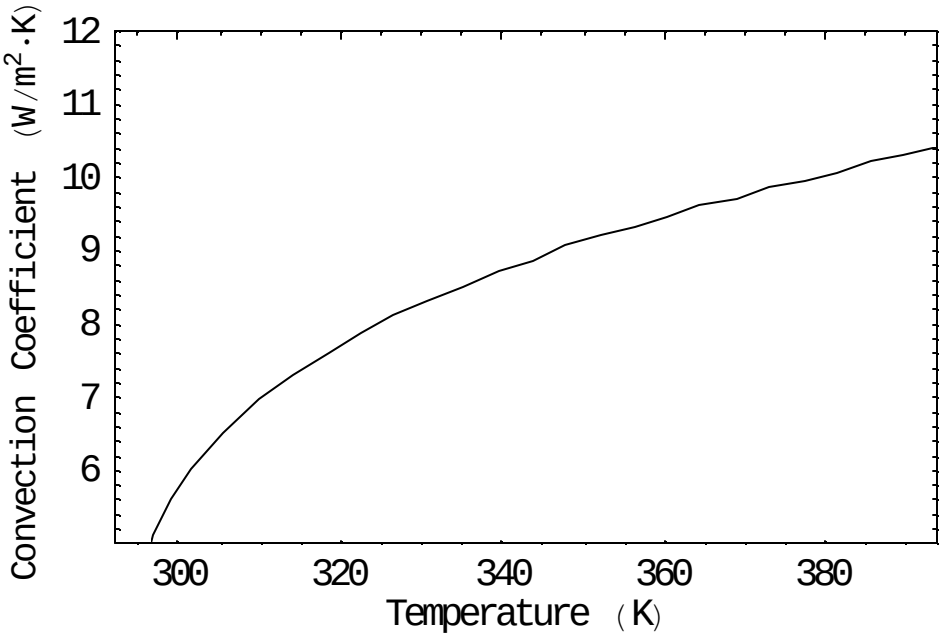

Figure A.10: Plot of the heat convection coefficient for the wafer surface.

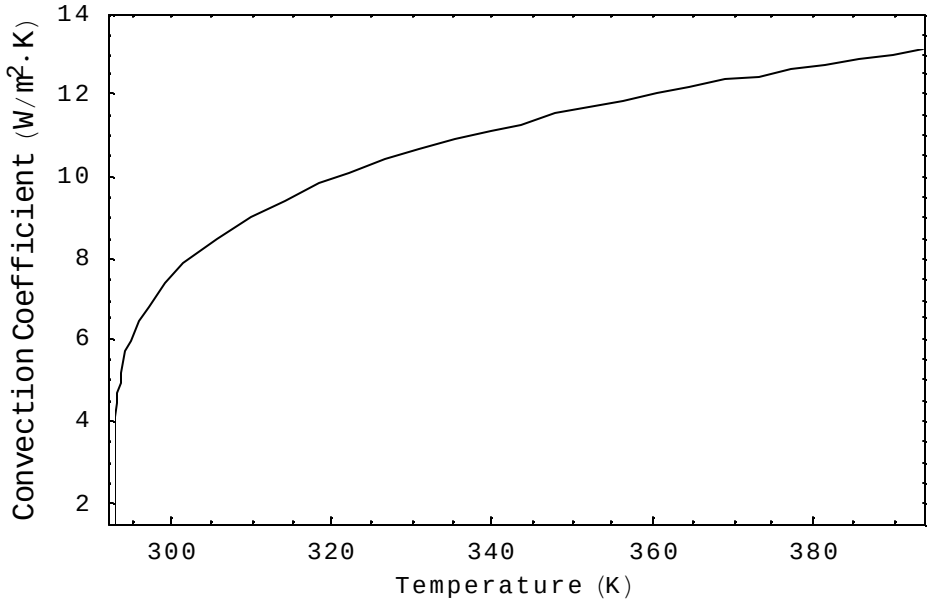

Figure A.11: Plot of the heat convection coefficient for the Pyrex Glass Surface.

A.3.2 Vertical Flat Plate

It is similar to hot flat plate facing up except the empirical equation of Nusselt number is a little bit different. Equation A.7 shows the equation of Nusselt number.

$$Nu = [(Nu_l)^6 + (Nu_t)^6]^{1/6} \quad \text{.....(A.7)}$$

where $$Nu_l = \frac{2.8}{\ln[1 + 2.8/(0.515 \cdot Ra_L^{1/4})]} \quad \text{.....(A.8)}$$

and $$Nu_t = 0.103 \cdot Ra_L^{1/3} \quad \text{.....(A.9)}$$

(5) Side Surface 1 of Pyrex Glass:

$$L_c = 0.00212$$
$$Ra_L = 0.859(T_{surface} - 295)$$

(6) Side Surface 2 of Pyrex Glass:

$$L_c = 0.00239$$
$$Ra_L = 1.230(T_{surface} - 295)$$

Figure A.12 and A.13 are the plots of the heat convection coefficient h from the calculations above.

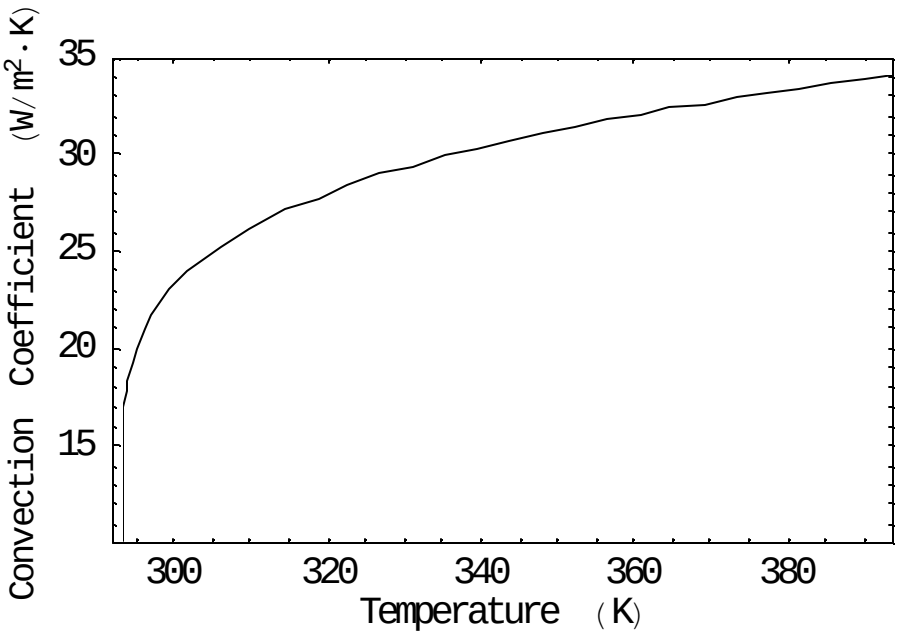

Figure A.12: Plot of the heat convection coefficient for the Side Surface 1 of Pyrex Glass.

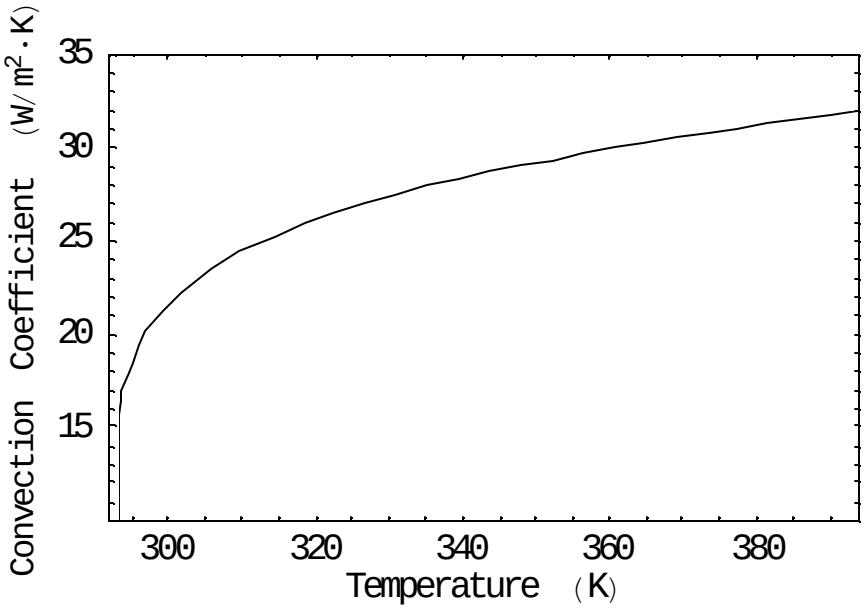

Figure A.13: Plot of the heat convection coefficient for the Side Surface 2 of Pyrex Glass.

Appendix B

MICRO CILIUM SIMULATION

Figure B.1 lists the material properties used in this simulation. They are cited from John Suh' s dissertation [5].

No.	Name	Young' s Modulus (GPa)	Poisson' s Ratio	CTE (10^{-6}°C^{-1})	Process Temperature (°C)
1	PIQ-L200 (polyimide)	8.6	0.33	2	100-350
2	PIQ-3200 (polyimide)	2.7	0.33	50	100-350
3	Silicon Nitride	183	0.25	1.5	300
4	50:50 Ti-W	340	0.2	4	25-40
5	Aluminum	70	0.33	23.6	25-40

Figure B.1: The material properties used in this simulation cited from John Suh' s dissertation.

This is a steady state simulation. The element in the simulation is Solid45.
The temperature of the micro cilium was set at 25° C. Figure B.2 shows the dimension of the micro cilium. The layer structure of this micro cilium is quite complex and not uniform in the micro cilium. Figure B.3 shows the top view of the micro cilium. It will be clearer if expressing the layer structure with four sections: (1) Top to A (2) A to B (3) B to C (4) C to Bottom. Figure B.4~B.7 are the side views of each section. The view direction is from bottom to top. There is one thing, which is difficult to express in Figure B.4 and B.5. In the layer 2 and 3, they are divided into 7.2μm strips and alternate silicon nitride and PIQ-3200. The first strip from top in Figure B.4 is silicon nitride.

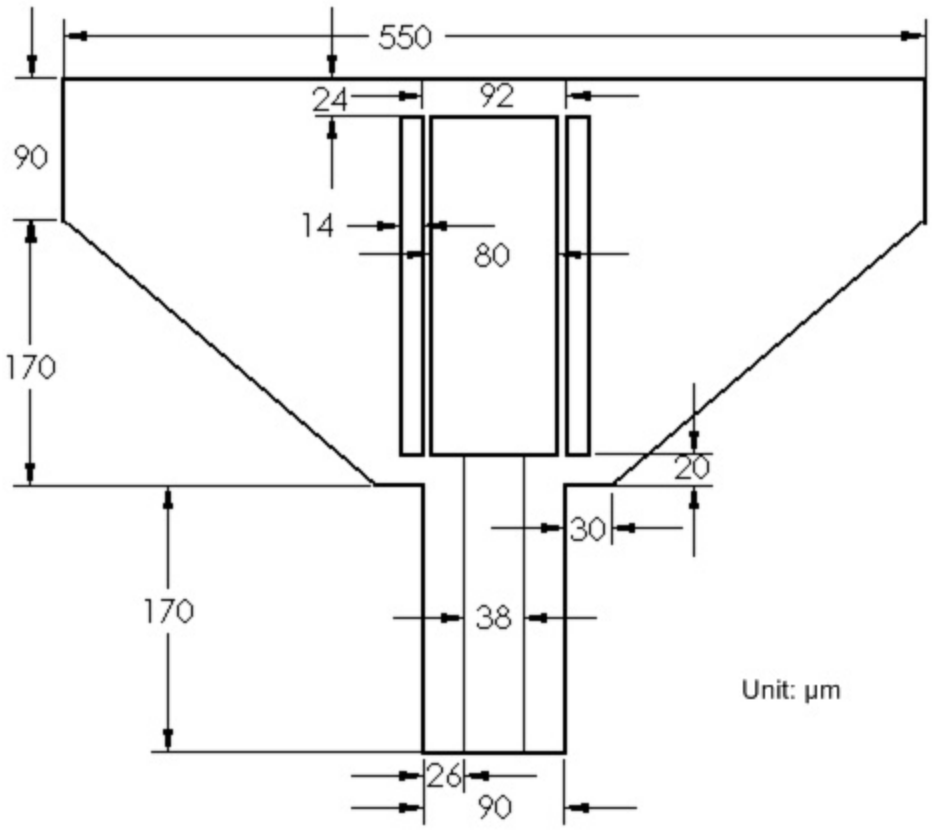

Figure B.2: The dimension of the micro cilium.

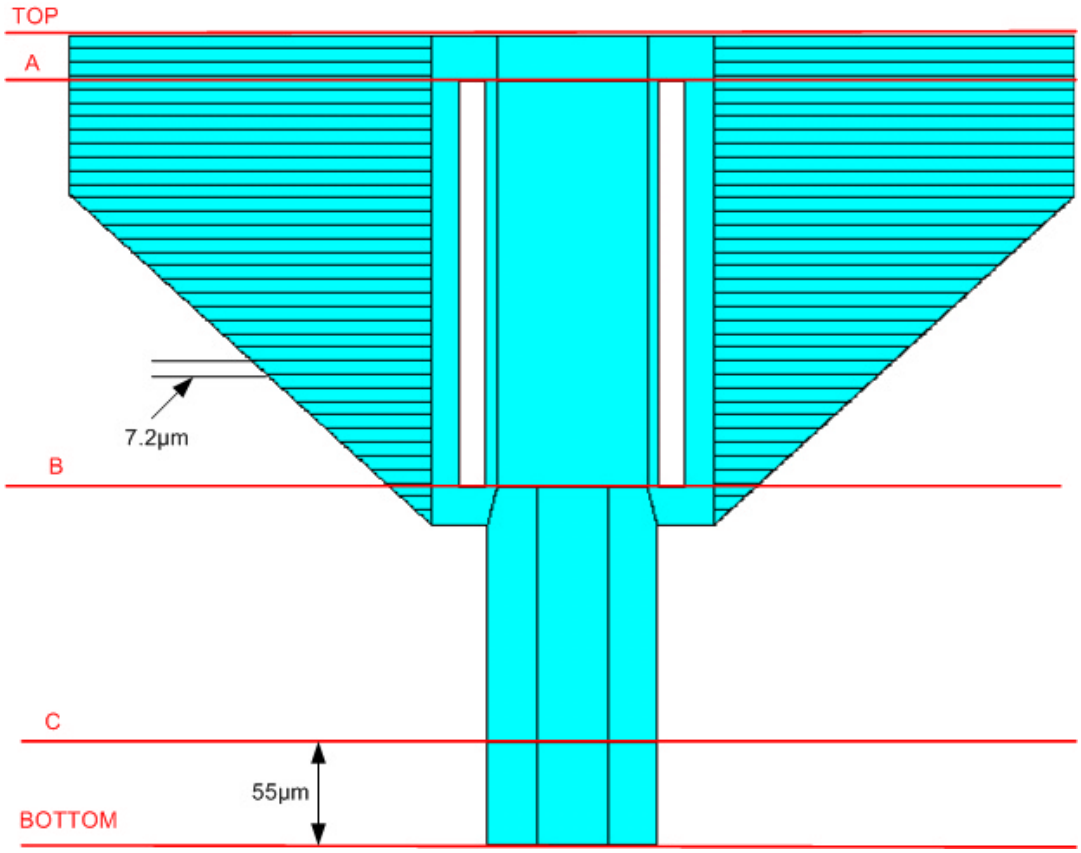

Figure B.3: The top view of the micro cilium. For expressing the layer structure, the micro cilium is separated into four sections: (1) Top to A (2) A to B (3) B to C (4) C to Bottom. The detailed information of each section is in Figure B.4~B.7.

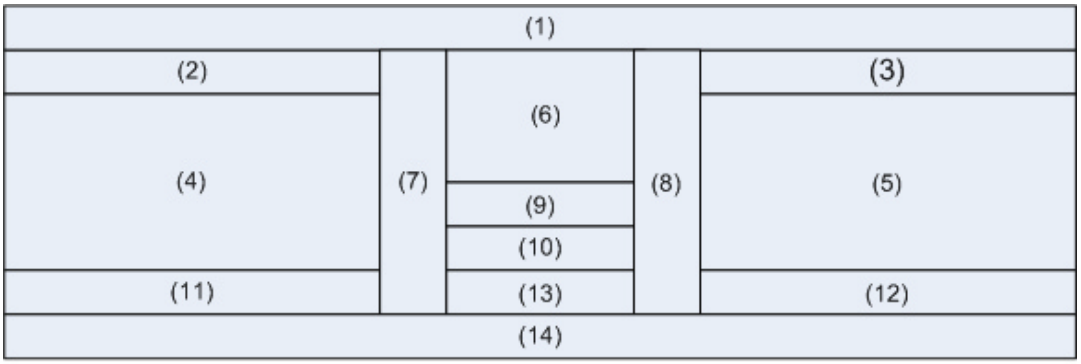

Layer Structure

Section 1: Top to A		
Layer Number	Thickness (nm)	Material
1	4500	PIQ-3200
2	130	Silicon Nitride
3	130	Silicon Nitride
4	780	Aluminum
5	780	Aluminum
6	690	PIQ-3200
7	1040	PIQ-3200
8	1040	PIQ-3200
9	130	PIQ-3200
10	90	PIQ-3200
11	130	Silicon Nitride
12	130	Silicon Nitride
13	130	PIQ-3200
14	4500	PIQ-L200

Figure B.4: The detailed information of the section 1 (Top to A), corresponding to Figure B.3. The view direction is from A to Top.

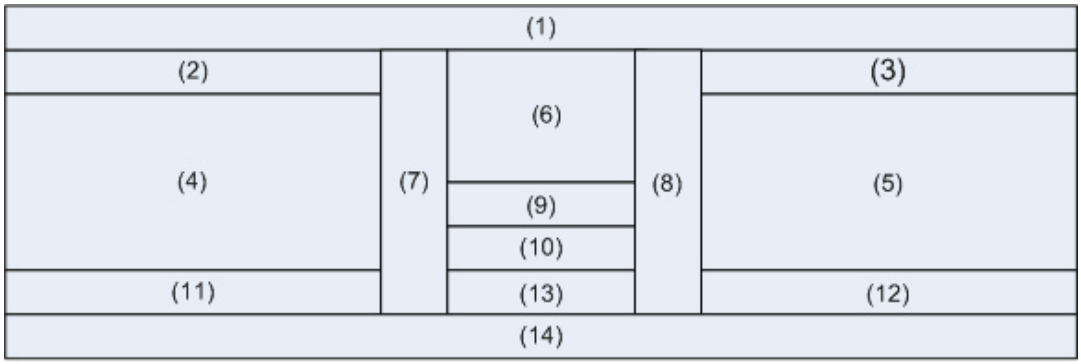

Layer Structure

Section 2: A to B		
Layer Number	Thickness (nm)	Material
1	4500	PIQ-3200
2	130	Silicon Nitride
3	130	Silicon Nitride
4	780	Aluminum
5	780	Aluminum
6	690	PIQ-3200
7	1040	PIQ-3200
8	1040	PIQ-3200
9	130	Silicon Nitride
10	90	50:50 Ti-W
11	130	Silicon Nitride
12	130	Silicon Nitride
13	130	Silicon Nitride
14	4500	PIQ-L200

Figure B.5: The detailed information of the section 2 (A to B), corresponding to Figure B.3. The view direction is from B to A.

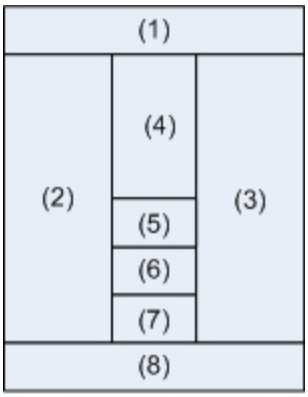

Layer Structure

Section 3: B to C		
Layer Number	Thickness (nm)	Material
1	4500	PIQ-3200
2	1040	PIQ-3200
3	1040	PIQ-3200
4	690	PIQ-3200
5	130	Silicon Nitride
6	90	50:50 Ti-W
7	130	Silicon Nitride
8	4500	PIQ-L200

Figure B.6: The detailed information of the section 3 (B to C), corresponding to Figure B.3. The view direction is from Bottom to C.

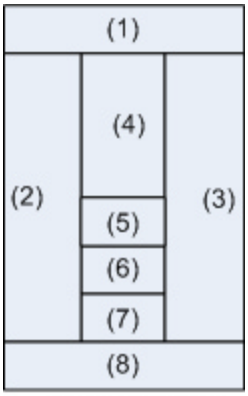

Section 4: C to Bottom		
Layer Number	Thickness (nm)	Material
1	4500	PIQ-3200
2	1040	PIQ-3200
3	1040	PIQ-3200
4	690	PIQ-3200
5	130	Aluminum
6	90	Aluminum
7	130	Silicon Nitride
8	4500	PIQ-L200

Figure B.7: The detailed information of the section 4 (C to Bottom), corresponding to Figure B.3. The view direction is from Bottom to C.